Short-term variations in middle atmospheric ozone induced by solar forcing

Sebastian Dikty

Universität Bremen

Short-term variations in middle atmospheric ozone induced by solar forcing

Vom Fachbereich für Physik und Elektrotechnik
der Universität Bremen

zur Erlangung des akademischen Grades eines

Doktor der Naturwissenschaften (Dr. rer. nat.)

genehmigte Dissertation

von

Dipl.-Met. Sebastian Dikty

aus Hannover

Gutachter:	Prof. Dr. J. P. Burrows
	Prof. Dr. J. Notholt
Eingereicht am:	18.12.2009
Tag des Promotionskolloquiums:	19.02.2010

Menschen können alles verlieren, was sie besitzen,
jedoch ihr Wissen und ihre Träume kann ihnen niemand nehmen.

Für meine Eltern
Gustav-Adolf und Renate Dikty

Abstract

Ozone is one of the most publicly discussed atmospheric trace gases since the discovery of the ozone hole over Antarctica in the mid 1980s. The purpose of this thesis is to investigate the solar influence on ozone of the middle atmosphere, with the focus being on variations on small time scales of less than a month. On the one hand the modulating nature of the 27-day solar rotation signal on stratospheric ozone using a new ozone profile data set from SCanning Imaging Absorption spectroMeter for Atmospheric CHartographY (SCIAMACHY) is studied. In this context, common and new frequency analysis techniques help to unravel dominant signals. On the other hand data from the latest version 1.07 Sounding of the Atmosphere using Broadband Emission Radiometry (SABER) tropical ozone (1.27 μm as well as the 9.6 μm retrieval) and temperature data are studied with respect to daytime variations in the upper mesosphere.

The frequency analysis of the 27-day solar rotation signal in SCIAMACHY ozone data ($< 20°$ latitude, 20-60 km altitude, 2003-2008) was carried out with the help of commonly used tools, like the fast-Fourier transform (FFT) and cross-correlation (CC), but was also supplemented with the continuous wavelet transform (CWT), which was not used before in the analysis of satellite ozone data. The CC showed that the maximum correlation between the Mg II index (used in this thesis as solar proxy) and ozone is weaker during the maximum of solar cycle 23 ($r = 0.38$) than in the previous two solar cycles that have been investigated in earlier studies using different data sets. The magnitude of the ozone signal is highly time dependent and may vanish for several solar rotations even close to solar maximum conditions. The FFT analysis reveals, besides the 27-day signal, several frequencies close to 27-days. The ozone sensitivity (i.e. ozone change in % per 1 % change in 205 nm solar flux) is on average about 0.2 %/% above 30 km altitude and smaller by about a factor of two compared to earlier studies. For selected three month periods the

sensitivity may rise beyond 0.6 %/% in better agreement with earlier studies. The analysis of the 27-day solar rotation signal was also carried out with stratospheric European Centre for Medium range Weather Forecast (ECMWF) temperature data from the operational analysis covering the same period as the SCIAMACHY data (2003-2008). Although direct radiation effects on temperature are weak in the upper stratosphere, temperature signals with statistically significant periods in the 25-35 day range similar to ozone could be found with the applied methods.

In addition to the 27-day solar rotation signal, the investigation of the SABER tropical mesospheric ozone and temperature daytime variations was combined with a comparison to the output of the three-dimensional general circulation and chemistry Hamburg Model of the Neutral and Ionized Atmosphere (HAMMONIA). The results show good agreement for ozone. The amplitude of daytime variations is in both cases approximately 60 % of the daytime mean. During equinox the daytime maximum ozone abundance is for both, the observations and the model, higher than during solstice, especially above 80 km. Furthermore, HAMMONIA output of daytime variation patterns of several other different trace gas species, e.g., water vapor and atomic oxygen, is discussed with respect to the daytime pattern in ozone. In contrast to ozone, temperature data show little daytime variations between 65 and 95 km and their amplitudes are on the order of less than 1.5 %. At last, SABER and HAMMONIA temperatures show significant differences above 80 km in their daytime pattern.

Publications

Journal articles

Dikty, S., Weber, M., von Savigny, C., Sonkaew, T., Rozanov, A., and Burrows, J. P.: Modulations of the 27-day solar rotation signal in stratospheric ozone from SCIAMACHY (2003-2008). J. Geophys. Res., doi:10.1029/2009JD012379, paper in press.

Dikty, S., Schmidt, H., Weber, M., von Savigny, C., and Mlynczak, M. G.: Daytime ozone variations in the mesosphere: A comparison between SABER observations and HAMMONIA modeling, Atmos. Chem. Phys. Discuss., 10, 2005-2029, 2010.

Conference contributions (talks)

Dikty, S., Weber, M., Sonkaew, T., Rozanov, A., von Savigny, C., and Burrows, J. P.: Modulations of the solar influence on the stratosphere - A decomposition of SCIAMACHY ozone and ECMWF temperature data, EUMETSAT Meteorological Satellite Conference, September 21-25, 2009, Bath, England.

Dikty, S., Weber, M., Sonkaew, T., Rozanov, A., von Savigny, C., and Burrows, J. P.: Wavelet Analyse von stratosphärischen SCIAMACHY Ozon Daten - Die Suche nach dem 27-Tage Zyklus, DPG Spring Meeting, March 2-6, 2009, Hamburg, Germany.

Dikty, S., Weber, M., Winkler, H., Sinnhuber, M., Sonkaew, T., Rozanov, A., von Savigny, C., Mlynczak, M. G., and Burrows, J. P.: Short Term Variations in Middle

Atmospheric Ozone from SCIAMACHY and SABER, COSPAR Scientific Assembly, July 13-20, 2008, Montreal, Canada.

Dikty, S., Pagaran, J. A., Weber, M., and Burrows, J. P: SCIAMACHY, SABER und der solare 27-Tage Zyklus in stratosphärischen Ozonprofilen, DPG Spring Meeting, March 10-14, 2008, Darmstadt, Germany.

Other conference contributions (selected posters)

Dikty, S., Weber, M., Winkler, H., Sonkaew, T., von Savigny, C., Rozanov, A., Sinnhuber, M., Mlynczak, M. G., and Burrows, J. P.: Short Term Variations in Middle Atmospheric Ozone from SCIAMACHY and SABER, SPARC General Assembly, August 31 to September 5, 2008, Bologna, Italy.

Dikty, S., Weber, M., Winkler, H., Sonkaew, T., von Savigny, C., Rozanov, A., Sinnhuber, M., Mlynczak, M. G., and Burrows, J. P.: Short Term Variations in Middle Atmospheric Ozone from SCIAMACHY and SABER, Quadrennial Ozone Symposium, June 29 to July 5, 2008, Tromsø, Norway.

Dikty, S., Pagaran, J., Weber, M., Rohen, G., von Savigny, C., and Burrows, J. P.: On the use of Fourier analysis power spectra to identify temporal connections between ozone and solar UV radiation during 27 day solar rotation, EGU General Assembly, April 15-20, 2007, Vienna, Austria.

Contents

Motivation and objectives

Climate change is one of the main issues of our times. The United Nations Environment Program (UNEP) and the World Meteorological Organization (WMO) founded the Intergovernmental Panel on Climate Change (IPCC) in 1988. One of its task is to evaluate the risks of global warming and to develop strategies to avoid, minimize and adapt to these risks. Four reports on the respective scientific expertise have already been published (1990, 1995, 2001, and 2007). It is of utmost importance to determine anthropogenic influences on climate change in order to have the potential to make action suggestions to individuals in general and policy makers in particular. To do so, natural sources of climate change need to be identified and separated from anthropogenic sources.

When speaking of climate, one has to bear in mind that a single climatological state (e.g., temperature) is the average of at least 30 years of data (Le Treut et al., 2007; WMO, 2009). Classically, climate (from the Greek *klima*, meaning *inclination*) happens on time scales of thousands of years with the sun being literally the center of attention. In Milankovitch's theory (Köppen et al., 1924) the modulation of the Earth's movement around the sun causes naturally occurring changes for life on Earth. These are the variations of the orbital shape (eccentricity, 95-400 thousand years), the axial tilt (obliquity, 41 thousand years), and the axial precession (19-24 thousand years).

Data on the above mentioned timescales are hard to acquire. All satellite data from within the last 30 years generally providing global information describe just a single state of the Earth's climate. If one wants to understand more of the physics and chemistry of the Earth's atmosphere on a climatological time scale, it needs to be understood it on *small* time scales first. For studying short-term variations, satellite data are particularly valuable. In order to extend investigations above decadal time scales, space observations need to continue.

The Climate And Weather of the Sun-Earth System (CAWSES) program sponsored by the Scientific Committee on Solar-Terrestrial Physics (SCOSTEP) aims at the enhancement of the understanding of such natural occurring phenomena that impact life on Earth and our society. The research as presented in this thesis was carried out within the framework of the German priority program of CAWSES and provides new knowledge on short-term solar influences on middle atmospheric ozone. Joined with the results of all participating scientists, it might help to extrapolate from small to larger time scales, into the past or even into the future.

Outline of this thesis

The presented thesis is divided into three parts as follows:

Part I refreshes the readers knowledge about solar radiation and the origin of short-term variations in the sun's radiative output. It also provides fundamental knowledge on the physics and the chemistry of the Earth's atmosphere.

Part II deals with the satellite instrumentation and data used in this thesis. The statistical methods are being introduced.

Part III contains the results as presented in peer-reviewed journals. On the one side the influence of the solar rotation signal on stratospheric ozone and on the other the daytime variations of upper mesospheric ozone are being examined.

Part I

Fundamentals

1 The sun

The hydrogen fusion process within the sun's core is ultimately the most important source of energy to mankind and life on Earth in general. Our civilization uses this source either directly or indirectly, except for fission or tidal power, which are based on strong nuclear interaction and gravity, respectively. Direct ways to utilize solar energy sources are, e.g., photo voltaic and solar heat. In addition, the sun's energy drives the winds, which on the other hand are the motor for ocean currents, and the water cycle. Fossil fuels like coal, oil, gas, and wood were only able to have been produced by organic life that once and nowadays relies primarily on energy from the sun. This Chapter will therefore introduce the source of solar radiation and explains the origin of periodic solar signals.

1.1 Solar fusion and radiative output

The sun consists mainly of hydrogen, helium, and a few other light elements as plasma, freed of their electrons. The very source of the sun's energy is the hydrogen fusion or hydrogen burning process within the sun's core, which extends to about 25 % of the sun's diameter. The sun's enormous mass is being pulled together by gravity, which generates very high temperatures of approximately 10^7 K and densities of up to 160 g/cm^3 in the core. At these temperatures hydrogen burning is sparked, letting two protons fuse to deuterium, a positron, and an electron neutrino as shown in Eq. 1.1. Due to the mass defect binding (thermal) energy is already released (Fig. 1.1). Consequently helium nuclei are formed and energy in form of hard gamma radiation is emitted. Equations 1.1 to 1.3 describe the so called pp-reaction chain, which is also shown in Fig. 1.1.

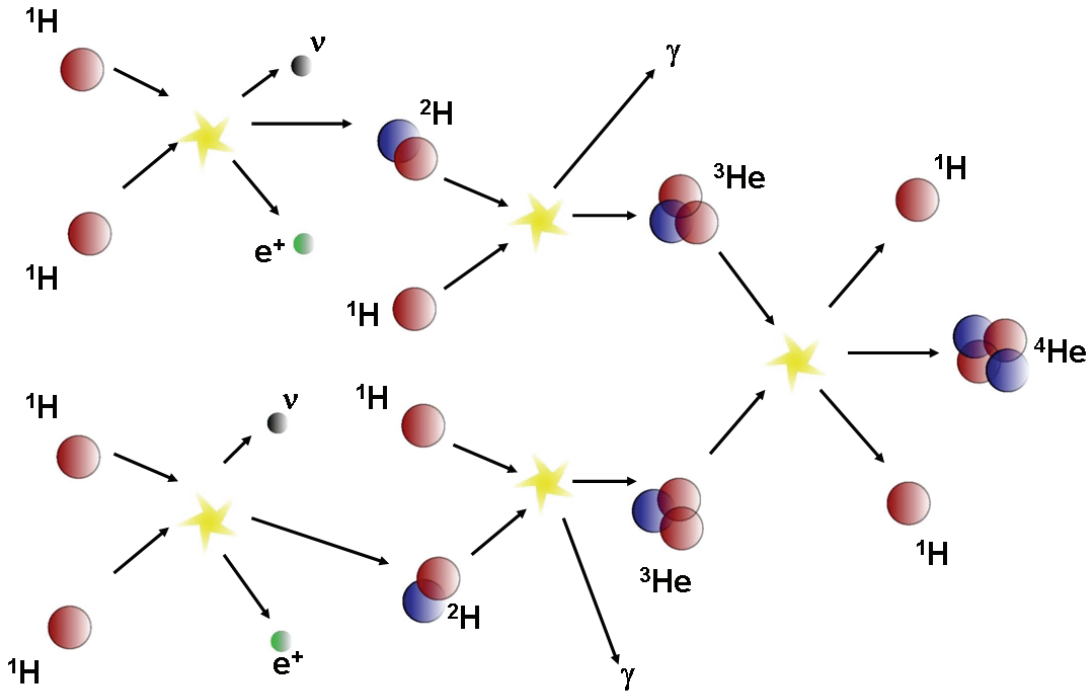

Figure 1.1: Illustration of the reactions involved in the pp-chain. Red balls resemble protons and blue balls resemble neutrons.

$$2 \cdot (p + p \rightarrow {}^{2}H + e^{+} + \nu_{e}) \,, \tag{1.1}$$

$$2 \cdot ({}^{2}H + p \rightarrow {}^{3}He + \gamma) \,, \tag{1.2}$$

$${}^{3}He + {}^{3}He \rightarrow {}^{4}He + 2p \,. \tag{1.3}$$

The gamma quants travel trough the radiation belt of the sun being involved in many secondary reactions with the nuclei present, and counterbalancing the gravitational pull towards the middle of the sun. Textbooks indicate that the radiative energy needs several million years before it finally reaches the visible sun's surface, known as the photosphere, whereas other authors calculated the diffusion time of solar photons in the order of 10^5 years (Mitalas and Sills, 1992).

The solar radiation that can be measured outside the Earth's atmosphere follows mainly Planck's Law:

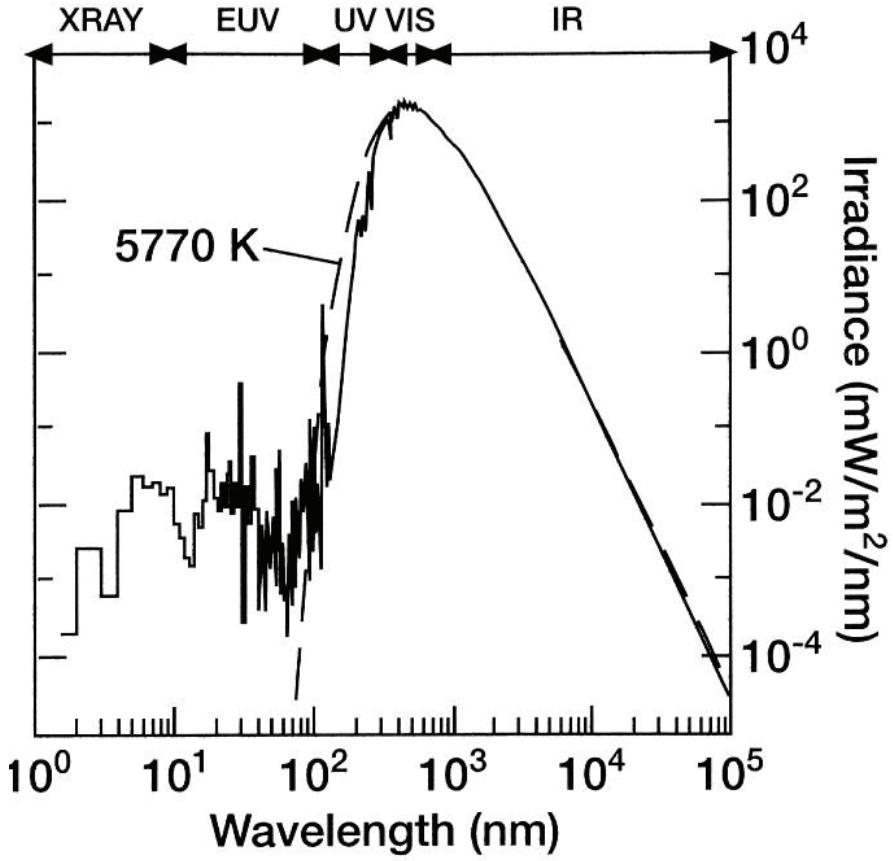

Figure 1.2: Composite extra-terrestrial solar spectrum measured by XPS, SOLSTICE and SIM. The dashed line indicates the blackbody radiation at 5770 K following Planck's law (Eq. 1.4) (Rottman et al., 2006).

$$I(\lambda, T) = \frac{2hc^2}{\lambda^5} \cdot \left[\frac{1}{e^{\frac{hc}{k_B \lambda T}} - 1} \right] , \tag{1.4}$$

with the Boltzmann constant $k_B = 1.38065 \cdot 10^{-23}$ J $\cdot$ K^{-1}, Planck's quantum h = 6.626 10^{-34} Js, and the speed of light c = $2.9979 \cdot 10^8$ m $\cdot$ s^{-1}. The spectral irradiance I as a function of wavelength λ and surface temperature T of a blackbody. Planck's curve for the sun (T = 5770 K) is indicated as dashed line in Fig. 1.2. The actual spectrum is shown as solid line and differs from Planck's curve. Figure 1.2 is a composite extra-terrestrial solar spectrum measured by the XPS (Woods et al., 2005),

the SOLSTICE (Rottman, 2000), and the SIM (Harder et al., 2000), all of which are flying on the SOlar Radiation and Climate Experiment (SORCE) satellite (Woods et al., 2000). Emissions shortward 100 nm account from blackbody radiation with its origin in the sun's chromosphere and corona, and from line emissions from elements in the sun's outer layers. The chromosphere is the layer directly above the photosphere, extending about 5000 km and with rising temperatures the further the distance to the sun is, whereas the corona extends millions of kilometers into interplanetary space with very low gas densities.

In addition to the emissions from the sun's atmosphere (i.e. chromosphere and corona), elements therein absorb radiation emitted from the photosphere. Examples of absorbing elements of the so called *Fraunhofer lines* (named after the German physicist Joseph von Fraunhofer, 1787 - 1826) are O_2, Na, Fe, He, Mg, and Ca. The absorption feature of Mg II (i.e. simple ionized Mg) at 280 nm, originating in the photosphere, in combination with emission lines within the absorption feature, originating in the chromosphere, is used throughout this thesis and referred to as Mg II index, a proxy for solar activity (cf. Sect. 6.3.2).

1.2 11-year solar cycle

Two factors play an important role in the 11-year solar cycle. On the one hand there is the differential rotation of the sun and on the other hand the interaction between plasma and the sun's magnetic field. To start with the latter, it is still an open debate among solar physicists whether or not the plasma follows the magnetic field lines or vice versa (e.g., Litvinenko, 2000; Stepanov, 2008). Assuming that the movement (rotation) of the plasma drags its magnetic field in behind and also assuming that the plasma near the sun's equator rotates faster than the plasma closer to the poles (differential rotation), the magnetic field of the sun becomes twisted with no clear polarity to it (cf. Fig. 1.3). This happens during solar maximum, when sunspots are widely visible on the sun's surface. The inter twisted magnetic field lines also heat the chromosphere leading to an intensified radiative output. During solar minimum the sun's magnetic field is more or less bipolar, sunspots are no longer visible and the total solar irradiance has reached its minimum. It takes approximately 22 years

for the magnetic field to fully reverse itself to its original alignment, going through two maxima and minima. So, what is actually measured is a 11-year solar cycle in the solar irradiance. Already Galileo observed the appearance and disappearance of sunspots dating back to the 17^{th} century. Yet, it was the German astronomer Samuel Heinrich Schwabe, who discovered in the middle of the 19^{th} century the periodicity of recurring minima and maxima in the sunspot numbers on time scales between 9 to 14 years. Therefore the 11-year solar cycle is often referred to as *Schwabe-cycle*.

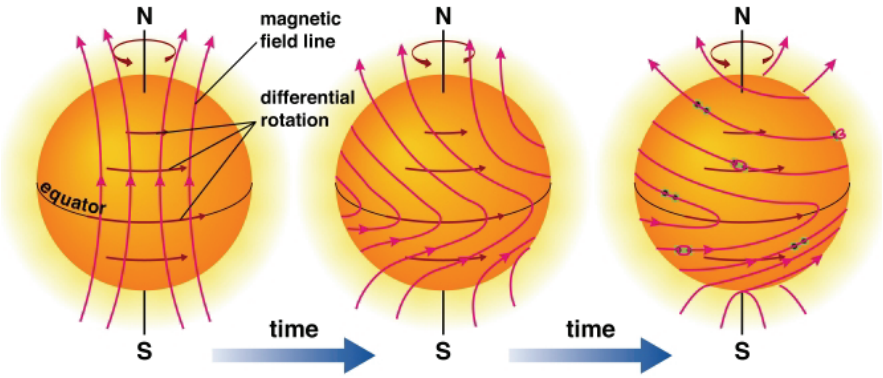

Figure 1.3: Illustration taken from Bennett et al. (2008) on the origin of the 22-year solar magnetic cycle.

1.3 27-day solar signal

On the sun's surface some regions are more active than others, emitting higher levels of radiation, especially at shorter wavelengths less than 320 nm. These active regions usually correspond to areas with an intensified magnetic field activity, i.e. the polarity of the field lines is under constant change and other than on, e.g., the Earth the sun does not have one *North* and one *South* pole, but depending on the period within the solar cycle, the sun has thousands to millions of magnetic poles. These active magnetic field lines heat the chromosphere additionally leading to higher emissions from the gases within the chromosphere. Besides the magnetic heating of the chromosphere, upwelling and downwelling of plasma from below the sun's surface leads to regions with different surface temperatures (Pagaran et al.,

2009, and references therein). Sun spots are usually colder than the surrounding plasma. This is easily explained with their darker appearance resulting from lower blackbody emissions (cf. Eq. 1.4).

The 27-day solar signal itself originates from the (differential) rotation of the sun. Assuming a region with intensified radiative emissions on the sun's surface rotates with the sun, every time this region is facing towards the Earth an observer outside the Earth's atmosphere would measure this radiative maximum. The sun's rotation period is 27 days in the mean. As the sun is built of plasma (a fluid), the rotation periods differ according to the solar latitude, i.e. the distance to the rotation axis. The plasma at the sun's equator rotates faster (25 days) than the plasma close to the sun's poles (30 to 32 days). This effect is called the differential rotation, which is one of the main focuses of this thesis.

Three major, commonly used proxies (among other) exist to track the 27-day solar rotation signal and the 11-year solar cycle. The radio flux at 10.7 cm, the ultraviolet (UV) flux at 205 nm, and the Mg II index at 280 nm, which can be measured from the ground and with satellites. The latter is mainly used in Chapters 5 and 6 of this thesis.

1.4 Particle emissions

In addition to the emission of electromagnetic energy the sun also emits particles into space. It looses approximately 10^9 kg per second of its own mass this way. The so called solar wind consists of ionized, highly energetic particles, mainly protons, electrons, and helium nuclei (alpha-particles), but also of some heavier elements. The emitted particles reach the Earth usually within 2 to 4 days after emission. Photons, which travel at the speed of light, only need approximately 8 minutes. The solar wind is deflected of the Earth's magnetic field towards the polar cusps, where they are able to enter the Earth's atmosphere. Aurorae are the eye-catching phenomena at high latitudes attributed to particle precipitation. The downside of such events related to intensified solar wind, e.g., solar proton events (SPEs) and coronal mass ejections (CMEs), are the perturbative effects high energetic particles have on (communication) satellites and other sensitive electronics on the Earth's

surface. In addition, heavy solar winds can drag satellites into the atmosphere (e.g., Jastrow and Pearse, 1957; Doornbos and Klinkrad, 2006). SPEs are also known to dramatically effect the composition of atmospheric trace gases, e.g. the destruction of high latitude ozone via NO_x, which is produced in great amounts by the impact of energetic particles on O_2 and N_2 (Rohen et al., 2005, and references therein). The effect of solar particle emissions is not the focus of this thesis and it will be rather concentrated on radiative emissions.

2 The atmosphere

The Earth's atmosphere is a very thin layer of gases that engulfs our planet, enabling life as commonly comprehended. The gases are kept in place by the gravitational pull of the Earth's mass. The major meteorological and physical processes in the atmosphere are driven by solar radiation and the spatial and temporal variability of state variables like temperature, pressure, and density. Fundamental principles of the structure of the Earth's atmosphere and the processes involved in radiative transfer need to be understood, in order to be able to retrieve trace gas concentrations from satellite measurements. These fundamental principles are being introduced in this Chapter.

2.1 Structure of the atmosphere

Most of the gases are well mixed up to a height of approximately 100 km (homosphere). Besides water vapor, which is highly variable, the main constituents of the homosphere are nitrogen (N_2) with 78.09 vol-%, oxygen (O_2) with 20.95 vol-%, and Argon (Ar) with 0.93 vol-% (Roedel, 2000). All the other gases are referred to as trace gases with a mixing ratio in the order of a few molecules (parts) per million (ppm) to even less than a few parts per billion (ppb). Reactive species exist only in minor amounts of less than a few ppm. A list of the main constituents is given in Table 2.1. Above 100 km the mean free path of the gas molecules rises because of the reduced air pressure. Heavier molecules tend to sink to the lower part of the heterosphere, lighter molecules like H_2 are mainly located above, i.e. if they do not escape the Earth's gravity at all. The boundary between homosphere and heterosphere is called turbopause.

The air pressure at sea level $p(z_0)$ is of the order of 1000 hPa (i.e., 10^5 N $\cdot$ m^{-2}) and decreases in first approximation exponentially with height z according to the

gas		molar mass	vol-%	mass-%
nitrogen	N_2	28.020	78.09	75.73
oxygen	O_2	32.000	20.95	23.14
argon	Ar	39.940	0.93	1.28
neon	Ne	20.180	$18.200 \cdot 10^{-4}$	$10.500 \cdot 10^{-4}$
helium	He	4.003	$5.240 \cdot 10^{-4}$	$10.724 \cdot 10^{-4}$
krypton	Kr	83.800	$1.140 \cdot 10^{-4}$	$3.300 \cdot 10^{-4}$
xenon	Xe	131.300	$0.087 \cdot 10^{-4}$	$0.390 \cdot 10^{-4}$
air		28.970		

Table 2.1: Constituents of a water vapor free atmosphere according to Roedel (2000), permanent species.

barometric formula (Roedel, 2000):

$$p(z) = p(z_0) \cdot exp\left[-\frac{M \cdot g}{R \cdot T} \cdot (z - z_0)\right] , \; z_0 = 0 , \tag{2.1}$$

with the gravitational acceleration g = 9.81 m $\cdot$ s^{-2}, the universal gas constant R = 8.315 J $\cdot$ K^{-1} $\cdot$ mol^{-1}, and the molar mass of *air* M = 0.02896 kg $\cdot$ mol^{-1}.

Another method to categorize the atmosphere is by taking the vertical temperature gradient into consideration (Fig. 2.1, blue solid line). The lowermost part of the atmosphere where the temperature decreases with altitude ($\approx$ -0.65 $\frac{K}{100\ m}$) is called the troposphere. Their vertical extension goes from the surface to the tropopause. The tropopause height differs according to the latitude. It is at approximately 17 to 18 km in the tropics, 10 to 12 km at mid-latitudes, and between 6 to 8 km close to the poles (Liljequist and Cehak, 1984; Häckel, 1999). The troposphere consists of 90 % of the atmospheric mass and is the most active region of the atmosphere. Weather, as many people understand it, happens in the troposphere. Almost all clouds are restrained to this layer, with the exception of polar stratospheric clouds (PSCs) and noctilucent clouds (NLCs), also called polar mesospheric clouds (PMCs)).

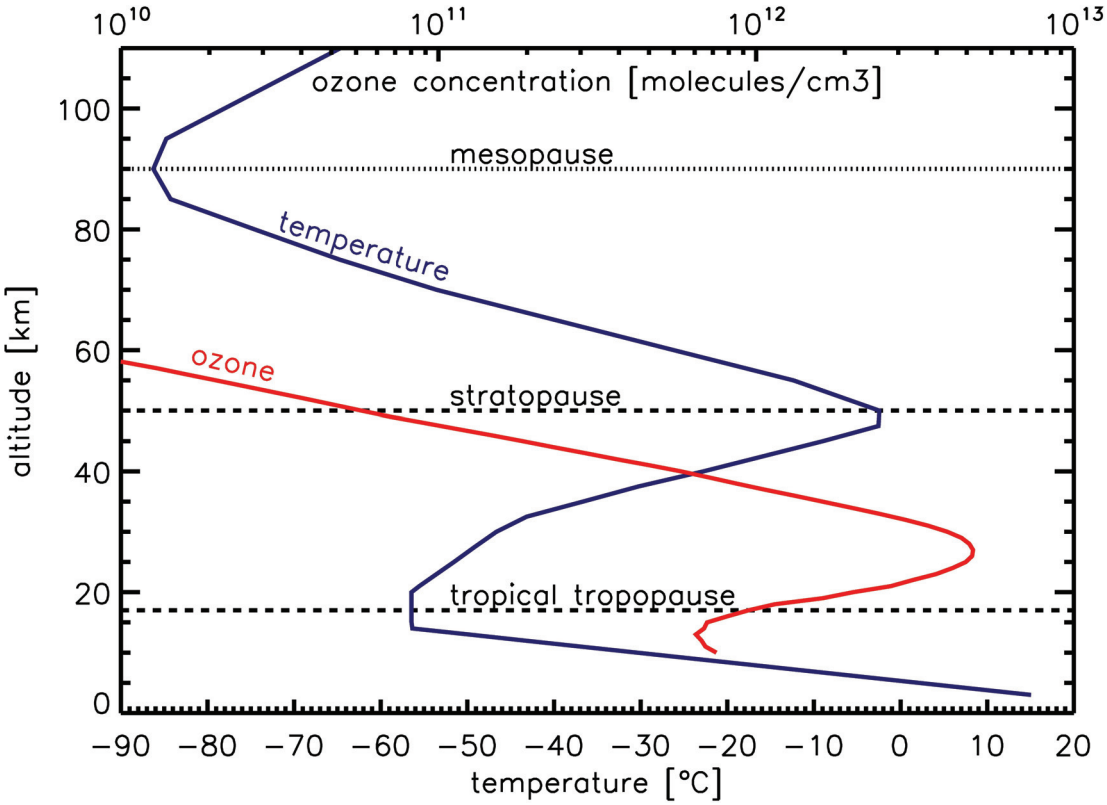

Figure 2.1: U.S. standard atmosphere 1976 (blue) and tropical annual mean SCIAMACHY ozone profile (red).

Tropospheric ozone (O_3) is most abundant in the lowermost layer (surface to approximately 2 km altitude), known as the boundary layer, but still less abundant if compared to the stratosphere, where 90 % of atmospheric ozone is located. Primary sources for tropospheric ozone are combustion processes and lightning, that rather thermally dissociate oxygen and nitrogen molecules. Solar radiation in the UV short-ward of 320 nm is limited near the surface. Another source of tropospheric ozone is via the combination of oxygen molecules with oxygen radicals that have been produced by the photolysis ($\lambda < 424$ nm) of NO_2 into O and NO (Seinfeld and Pandis, 1998).

The stable layer above the troposphere is called stratosphere, where temperature increases with altitude. The stratosphere stretches from the tropopause up to approximately 50 km (stratopause). In this layer the temperature gradient is

reversed, mainly due to the absorption of UV radiation by ozone. The negative temperature lapse rate suppresses vertical motion and creates a very stable dynamical environment, dominated by radiative processes.

The mesosphere (50 to 80 km) is again defined by decreasing temperatures with altitude. Ozone heating is no longer relevant. The mesopause is the upper boundary to the mesosphere. At low latitudes the mesopause is located between 95 and 100 km altitude (von Zahn et al., 1996; She and von Zahn, 1998). The atmospheric layer even further up is called the thermosphere. Here, *air molecules* are ionized by highly energetic solar radiation and particles. The lapse rate is again positive. Above an altitude of approximately 500 km the layer is called exosphere, where the collisions of *air molecules* are very rare and the gravitational pull hardly prevents the molecules from escaping our planet.

Figure 2.1 shows the extended U.S. standard atmosphere (temperature profile) defined in 1976. This vertical temperature profile still serves as a reference in several research activities. The main focus of this thesis lies on the stratosphere and the mesosphere, commonly known as the middle atmosphere. With the discovery of the ozone hole over Antarctica in the mid 1980s (Farman et al., 1985; Hamill et al., 1986), the importance of the middle atmosphere has increased and is monitored by regular intergovernmental investigations, e.g. the WMO Scientific Assessment of Ozone Depletion 2006 (WMO, 2007). The anthropogenic influence on the destruction of the polar ozone layer was recognized by many governments with the signature of the Montreal Protocol, especially the role of chlorofluorocarbons (CFCs) was highlighted (cf. Sect. 3.2).

2.2 Radiative transfer in satellite remote sensing

This section introduces the physical processes involved in radiative transfer. These processes play an important role in the retrieval of trace gas species from space and the ground. In addition, the radiative transfer equation is presented. Altogether, this section serves as an example to show the basics of ozone retrieval. Although the retrieval of ozone itself was not part of this thesis, the principle retrieval process will nevertheless be introduced in order to establish a context to the reader.

2.2.1 Radiative processes in the cloud free atmosphere

For the retrieval of information on atmospheric trace gas species from reflected or backscattered sunlight by satellite observations, the measurements are compared to simulated top-of-atmosphere spectral radiances. A forward radiative transfer model like SCIATRAN (Rozanov et al., 2005b) not only accounts for molecular absorption, it also has to account for other atmospheric processes, e.g. Rayleigh scattering, aerosol extinction, and ground surface reflection.

Molecular absorption

The unique absorption characteristics of molecules of a given species are best described by its absorption cross-section k. The absorption cross-section, depending on pressure and temperature, multiplied with the concentration n of the molecules produces the absorption coefficient α. Integrating along a finite light path results in the corresponding optical density τ. All of which is summarized in the Lambert-Beer's law (taken from Prölss, 2001),

$$L_\lambda(s) = L_{\lambda 0} \cdot exp\left[-\int_{s_1}^{s_2} k_\lambda(s) \cdot n(s)\, ds \right] , \tag{2.2}$$

with the monochromatic radiance L_λ decaying exponentially with respect to τ, while it neglects other absorbers, scattering and surface reflection.

Rayleigh and Raman scattering

Elastic scattering of electromagnetic radiation by molecules or particles, whose sizes are very small compared to wavelength of the incident light ($2\pi r \ll \lambda$), is called Rayleigh scattering. Consequently it applies to scattering of solar radiation by *air molecules*. The angular distribution of Rayleigh scattered light is given by the phase function (normalized to 4π)

$$\varphi_R(\vartheta) = \frac{3}{2} \cdot \frac{(1+d) + (1-d) \cdot cos^2\,\vartheta}{2+d} , \tag{2.3}$$

with the scattering angle ϑ and the depolarizing factor d. Multiplication of the Rayleigh scattering cross-section with the air density leads to the Rayleigh scattering

coefficient, which is proportional to λ^{-4}. So, decreasing wavelengths result in strongly increasing intensities of Rayleigh scattered light, which is the reason for the sky appearing blue during daylight. Multiple scattering is therefore mainly important in the UV/visible spectral range. The difference to the inelastic Raman scattering is that the wavelengths of the incident and scattered light are the same for Rayleigh scattering, not for Raman scattering.

Aerosol extinction

Aerosols are all airborne particles either in liquid or solid state, often a combination of both, with a liquid surrounding a solid nucleus. Typical radii are between 0.01 μm and 10 μm (Miranda and Fenn, 1974; Schuster et al., 2006). Scattering is the main contribution of aerosols to radiative transfer in the visible and near infrared spectral region. The Mie theory describes the scattering of spherical aerosols with sizes in the order of the wavelength of the incident light ($2\pi r \approx \lambda$). Noteworthy sources of aerosols are desert dust, soot, volcanic ash, and ocean spray. Apart from these, aerosols generally play a minor role in radiative transfer with respect to the middle and upper atmosphere, except for events, when they are loaded into the stratosphere via major volcanic eruptions.

Surface reflection

Surface reflection is important for lower atmospheric layers and for wavelengths greater than 310 nm. The albedo A (from the Latin word *albus*, meaning *white*) is expressing the surface reflection as the fraction of the incident to the reflected radiation, with $A \in [0,1]$ being a dimensionless quantity. In the visible, typical values for the Albedo are 0.1 for fallow cropland, 0.3 for deserts, 0.35 for ice, and 0.8 to 0.9 for fresh snow. The albedo of the sea surface strongly depends on the incident angle of the light. It can be as low as 0.04 for perpendicular incident and as high as 0.9 for solar zenith angles between 80 to almost 90 degrees. For the retrieval of ozone in the middle and upper atmosphere, surface reflection plays a minor to no role at all and is therefore not discussed in further detail in this thesis.

2.2.2 Radiative transfer equation

The radiative transfer equation describes the change of the electromagnetic spectrum along a light path due to absorption along the beam, scattering in or out of the beam and the gain by local sources. In its general form the radiative transfer equation is given as followed (Lenoble, 1993):

$$\frac{dL_\lambda(s)}{ds} = \kappa_\lambda \cdot \left[J_\lambda(s,L) - L_\lambda(s)\right] . \tag{2.4}$$

So, it is the change in spectral radiance L_λ, with the units $[W \cdot sr^{-1} \cdot m^{-2}]$. The radiance is given as radiant flux Φ per area A, solid angle Ω and direction Θ

$$L = \frac{d^2\Phi}{cos\Theta \cdot d\Omega \cdot dA} . \tag{2.5}$$

The extinction coefficient κ_λ accounts for all scattering and absorption processes, while J_λ stands for the source function, which again can be split into two terms. One for the scattering sources J_{sc} and one for the emitting sources J_{em}.

In case the source terms are irrelevant ($J_\lambda = 0$), Eq. 2.4 is reduced to

$$\frac{dL_\lambda}{L_\lambda} = -\kappa_\lambda \cdot ds , \tag{2.6}$$

and consequently to the Lambert-Beer's law (cf. Eq. 2.2, simplified here):

$$L(s) = L_0 \cdot e^{-\tau(s)} , \tag{2.7}$$

with τ(s) being the slant optical density of the atmosphere (i.e. the given finite light path):

$$\tau(s) = \int_{s_1}^{s_2} \kappa(s) \cdot n(s)\, ds . \tag{2.8}$$

Equation 2.7 describes the reduction of incoming radiation L_0 due to extinction.

2.2.3 Optimal estimation inversion

In remote sensing of the atmosphere the desired parameters (temperature, ozone concentration, ...) are not measured directly. With the help of *a priori* information, a radiative transfer model (like SCIATRAN) calculates in a forward step the spectral irradiance information, that would have been measured, e.g. by SCIAMACHY, if the *a priori* were *true*. It also calculates the profile in an inverse step. *A priori* information is usually a first guess of what the desired profile will look like. The next step is to compare the actually measured earthshine spectrum with the calculated model spectrum, considering the *a priori* (Rodgers, 2000). Iteratively the profile can be changed till the differences between calculated and measured spectra minimize the cost function. The profile that minimized the cost function is then regarded as the retrieved profile. A flow chart of this process is shown in Fig. 2.2.

For validation of the retrieved profile, comparisons with ground-based measurements, radiosondes, rocket-borne measurements, and other satellite observations permit the estimation of the error and deviation from the *true*.

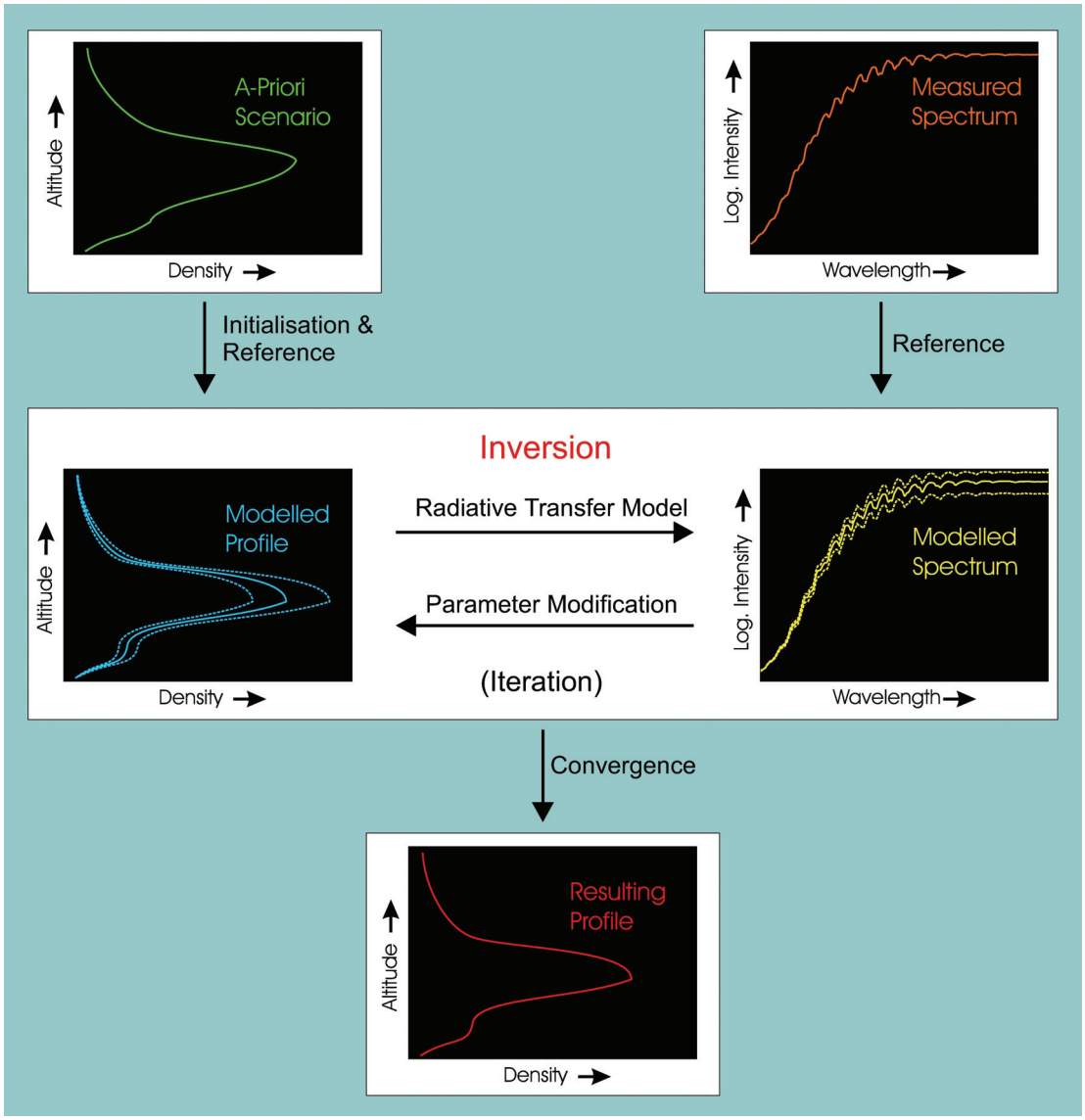

Figure 2.2: Flow chart of the optimal estimation process used in the retrieval of trace gas species from SCIAMACHY spectral measurements (figure courtesy of S. Noël and J. P. Burrows).

3 The chemistry

Ozone is a poisonous gas with a strong odor (from the Greek *ozein*, to smell) that causes respiratory irritation and can, e.g., damage lung tissue. While harmful in the troposphere, it acts as a protective shield in the stratosphere preventing dangerous ultraviolet (UV-B and UV-C) radiation from reaching the Earth's surface. As UV radiation has a potentially hazardous effect to life, not only mankind would be more exposed, e.g. to skin cancer or an impaired immune system, but all life on Earth's surface as well, if the protective ozone would not exist. The gross of atmospheric ozone resides in the stratosphere (less at the equator and more to the poles). The total amount of ozone above any point on the Earth's surface is measured in Dobson units (DUs), typically 260 DU to 330 DU, with large seasonal fluctuations, especially at higher latitudes. 100 DU correspond to a column of 1 mm of ozone if reduced to ground pressure. This Chapter deals with important mechanisms of ozone chemistry in the middle atmosphere.

3.1 Chapman mechanism in the stratosphere

Ozone is created when sunlight dissociates (splits) oxygen molecules (O_2) to atomic oxygen (O). The atomic oxygen (also called oxygen radical) quickly combines with further oxygen molecules to form ozone. This process is called the Chapman mechanism and is explained in detail in the following.

The original mechanism for atmospheric ozone formation and destruction from oxygen species was suggested by Chapman (1930). Solar UV radiation short-ward of 242 nm slowly dissociates molecular oxygen:

$$O_2 + h\nu \rightarrow 2O \,. \tag{3.1}$$

The oxygen atom (O) then rapidly reacts with oxygen in the presence of a third

molecule (e.g., O_2 or N_2), denoted as M to form ozone:

$$O + O_2 + M \rightarrow O_3 + M \; . \tag{3.2}$$

The ozone molecule is then able to strongly absorb radiation with wavelengths below 320 nm to decompose back to O and O_2:

$$O_3 + h\nu \rightarrow O + O_2 \; . \tag{3.3}$$

In addition, ozone may react with atomic oxygen to convert back into O_2:

$$O + O_3 \rightarrow 2O_2 \; . \tag{3.4}$$

The combination of two atomic oxygen atoms (O) in the presence of a third body also alters the concentration of O producing O_2:

$$O + O + M \rightarrow O_2 + M \; . \tag{3.5}$$

The UV absorption of O_2 in the region 175-195 nm (Shuman-Runge band) and formation of O from O_2 (reaction 3.1) play a more important role in the mesosphere, where they produce large concentrations of O. The oxygen atom concentration decreases with decreasing altitude as the intensity of radiation in the Shuman-Runge band weakens as [M] rises, increasing the speed of reaction 3.2. The ratio $\frac{[O_3]}{[O]}$ increases and reaction 3.2 dominates over reaction 3.3 in the stratosphere.

The oxygen family can be divided into two types, even oxygen (O_2) and odd oxygen ($O + O_3$). The odd oxygen is very reactive and inter-converts rapidly through 3.3 and 3.4. The formation of odd oxygen in equation 3.2 is driven by UV radiation, which is primarily absorbed in the upper stratosphere. As the intensity of solar radiation is highest over the tropical region, ozone formation mainly takes place in the tropical upper stratosphere (cf. Fig. 3.1).

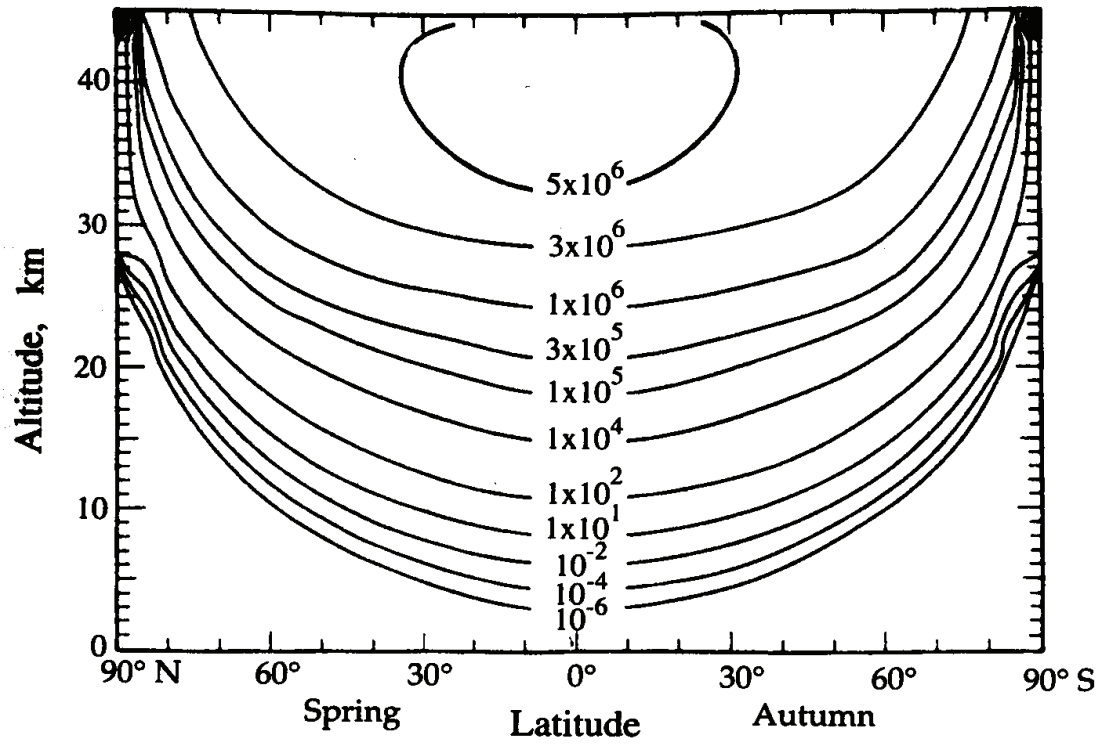

Figure 3.1: Ozone production rates in March [molecules/cm^3·s] (Johnston, 1975).

3.2 Catalytic ozone depletion

Taking only the Chapman mechanism into account would result in overestimated amounts of total ozone (800 DU on global average). So, the role of two other mechanisms controlling the amount of ozone in the atmosphere (mainly in the stratosphere) was recognized. First, an ozone transport mechanism from the tropics to higher latitudes was proposed (Brewer-Dobson (BD) circulation) (Brewer, 1949). The BD circulation explains the lower amounts of total ozone in the tropics although ozone production is highest there. Second, it was observed that both O and O_3 react with various other chemical species which alter the ozone budget significantly. It was found that ozone can be destroyed by a number of free radical catalysts. The most important families among these are HO_x (H, OH, HO_2, Bates and Nicolet, 1950), NO_x (NO, NO_2, Crutzen, 1970; Crutzen et al., 1975), ClO_x (e.g. ClO, Molina and Rowland, 1974; Stolarski and Cicerone, 1974), and BrO_x (e.g. BrO, Wofsy et al.,

1975). All of these species can be either of natural or anthropogenic origin. The catalytic ozone loss reactions are summarized below:

$$X + O_3 \rightarrow XO + O_2, \tag{3.6}$$

$$O + XO \rightarrow O_2 + X, \tag{3.7}$$

$$Net : O + O_3 \rightarrow 2 \cdot O_2, \tag{3.8}$$

with X and XO as chain carriers involving HO_x, NO_x, ClO_x, BrO_x, and IO_x families and X = OH, NO, Cl, Br, I. The importance of this catalytic reaction chain is that the ozone depleting substances are being recycled many times before they are removed and stored in more stable compounds. Presently, most of OH and NO in the stratosphere have natural sources, but the amounts of chlorine and bromine have risen with human activity dramatically (WMO, 2003). These species can be especially found in CFCs. CFCs are slowly transported towards the polar regions (via BD circulation). During polar night CFCs are stored in PSCs. The strong polar vortex constraints air masses within and with the dawn of the polar day, the photochemistry ignites a massive destruction of ozone leading to the known *ozone hole* (Farman et al., 1985; Hamill et al., 1986).

3.3 Active oxygen recycling in the mesosphere

In the following the most important reactions involved in the oxygen chemistry of the mesosphere are being introduced. These reactions are summarized in Table 3.1 and can be divided into two groups. The first group includes reactions happening during day and night, the second group includes only the reactions involving the photodissociation of molecular oxygen and ozone during daylight hours. A schematic of the active oxygen recycling can be seen in Fig. 3.2.

During the day the abundance of atomic oxygen rises through reactions 1-4. Due to the swiftness of reactions 5-8 atomic oxygen is quickly converted back into ozone and molecular oxygen. Ozone either reacts with atomic oxygen or atomic hydrogen (reactions 9+12) to also form molecular oxygen. The remaining hydroxyl radicals also react with atomic oxygen to form molecular oxygen (reaction 10).

	reaction			rate constant
1	$O_2 + h\nu$	$\rightarrow$	$2O$	$8.4 \cdot 10^{-10}$ $(177\ nm \leq \lambda \leq 256\ nm)$
2	$O_2 + h\nu$	$\rightarrow$	$O + O(^1D)$	$1.5 \cdot 10^{-13}$ $(\lambda \leq 177\ nm)$
3	$O_3 + h\nu$	$\rightarrow$	$O_2 + O$	$8.0 \cdot 10^{-4}$ $(200\ nm \leq \lambda \leq 730\ nm)$
4	$O_3 + h\nu$	$\rightarrow$	$O_2 + O(^1D)$	$5.1 \cdot 10^{-3}$ $(167\ nm \leq \lambda \leq 320\ nm)$
5	$2O + M$	$\rightarrow$	$O_2 + M$	$9.59 \cdot 10^{-34} e^{480/T}$
6	$2O + O_2$	$\rightarrow$	$O_3 + O$	$2.15 \cdot 10^{-34} e^{345/T}$
7	$O + 2O_2$	$\rightarrow$	$O_3 + O_2$	$2.15 \cdot 10^{-34} e^{345/T}$
8	$O + O_2 + N_2$	$\rightarrow$	$O_3 + N_2$	$8.82 \cdot 10^{-35} e^{575/T}$
9	$O + O_3$	$\rightarrow$	$2O_2$	$1.5 \cdot 10^{-11} e^{-2218/T}$
10	$O + OH$	$\rightarrow$	$O_2 + H$	$2.3 \cdot 10^{-11} e^{-90/T}$
11	$O + HO_2$	$\rightarrow$	$OH + O_2$	$2.8 \cdot 10^{-11} e^{172/T}$
12	$H + O_3$	$\rightarrow$	$OH + O_2$	$1.4 \cdot 10^{-10} e^{-270/T}$

Table 3.1: Important reactions involved in the balancing between active and inactive oxygen in the mesosphere (Allen et al., 1984a).

Hydroxyl radicals are also the product of the combination from atomic oxygen with the hydroperoxy radical HO_2.

Once daylight is no longer available for the photo-chemistry, reactions 6 to 8 dominate reactions 9 to 11 and use up the oxygen radicals. Atomic oxygen abundance drops and mainly ozone is produced. Ozone itself can then no longer be easily converted to molecular oxygen due to the lack of atomic oxygen. It can still be converted into hydroxyl radicals, but again due to the lack of atomic oxygen, hydroxyl is not easily being destroyed though reaction 10 to form molecular oxygen. Although speaking of active oxygen, during the night the lifetime of ozone is longer than during the day and high nighttime concentrations are build up in the mesosphere, especially near the mesopause ozone values may rise up to 40 ppm, in

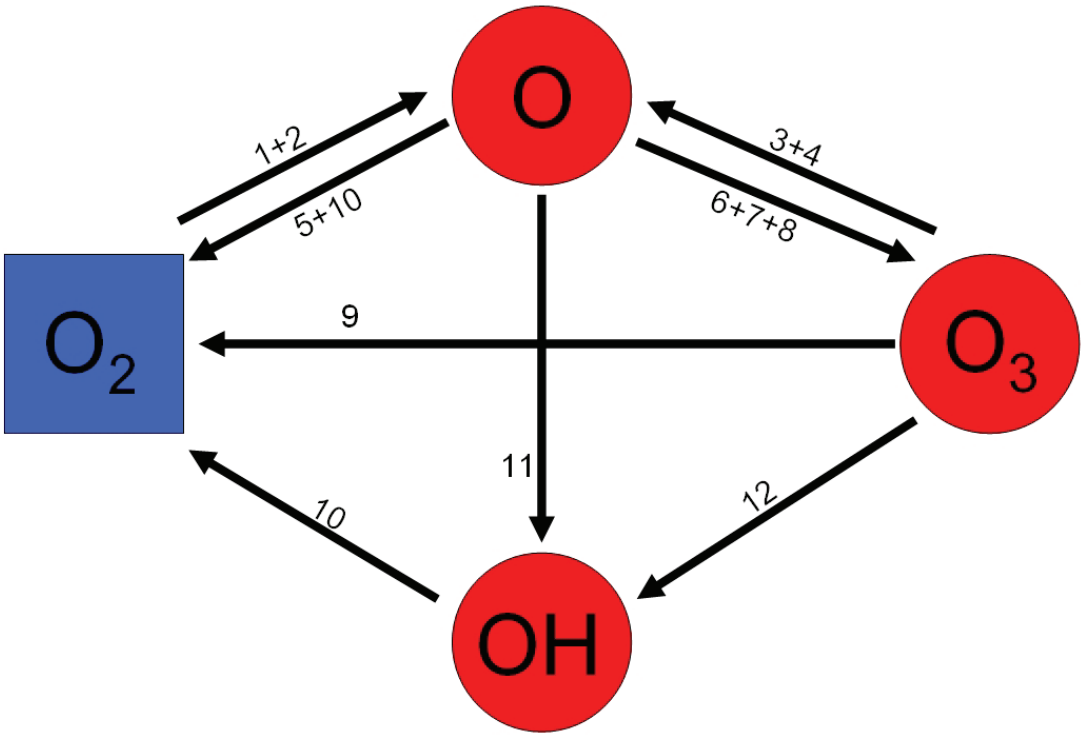

Figure 3.2: Schematic of the active oxygen recycling in the mesosphere according to Allen et al. (1984a). Red circles denote the active oxygen species. The numbers stand for the involved reactions listed in Table 3.1.

terms of volume mixing ratio (Smith et al., 2008).

3.4 Solar-ozone relations in the literature

With the extension of satellite remote sensing in the late 1970s and early 1980s the observation of solar influences on atmospheric ozone became easier. Orbital platforms offered the chance to globally investigate the composition and temporal variability of trace gases in general. Measurements were no longer restricted to ground-based observations. At the same time, computational power rose to a level that allowed the modeling of atmospheric chemistry and dynamics. As for the atmospheric dynamics, the physics behind air in motion (or fluids in general) is described by the Navier-Stokes equations. Often the simplified Euler equations

are used for atmospheric motion without considering friction, e.g. above the atmospheric boundary layer (Etling, 2002):

$$\frac{\partial \vec{v}}{\partial t} + (\vec{v} \cdot \nabla)\vec{v} + \frac{1}{\rho}\nabla p = 0\,, \tag{3.9}$$

with p being the atmospheric pressure, ρ the air density, and $\vec{v}$ the wind vector.

In addition to the knowledge of the location of an air parcel with time it is also necessary to understand the chemistry within such an air parcel. Especially the reaction rates need to be known in order to simulate the temporal variability of atmospheric species. These reaction rates can be obtained in laboratory measurements.

In the following an overview on selected studies is given that investigated solar influences on middle atmospheric ozone with respect to variations on timescales of the solar rotation period (27-days) and diurnal variability.

3.4.1 27-day solar signal

Chandra (1985) already asked the question whether solar-induced oscillations in stratospheric ozone are a *myth* or *reality*?. Nowadays it is clear that the solar rotation signal can be identified in middle atmospheric ozone. Table 3.2 summarizes selected studies that dealt with this issue, mainly at low latitudes. Gruzdev et al. (2009) gives a good summary on these studies. The ozone sensitivity (i.e. the change in ozone for 1 % change in solar flux at 205 nm) at an altitude of approximately 40 km was shown to be between 0.2 and 0.6 %/%. Another common point of interest is the phase lag between solar signal and ozone response. It was shown to be a few days around 30 km altitude and may even be reversed at altitudes around 50 km, i.e. the ozone *response* leads the solar signal. This response gets stronger the further you go into the lower mesosphere and may even be reversed further up in the mesosphere. A more in depth discussion of the above mentioned studies can be found in Sect. 6.2.

Table 3.2 also gives a quick overview on studies that investigated solar-ozone connections on time scales of 27 days with 1-, 2- or 3-dimensional models within the past three decades. With time the models advanced and additional dimensions were added in the calculation.

paper	parameter	atmospheric layer	model dimension
Hood (1984)	O_3	S	
Chandra (1985)	O_3, T	S	
Keating et al. (1985)	O_3	S, LM	
Eckman (1986b)	O_3	S, LM	
Hood (1986)	O_3, T	S	
Hood (1987)	O_3, T	S	
Keating et al. (1987)	O_3, T	S, LM	
Hood and Chantrell (1988)	O_3, T	S	
Hood et al. (1991)	O_3	S, M	
Chandra et al. (1994)	O_3	M	
Fleming et al. (1995)	O_3	S, LM	2D
Zhou et al. (1997)	O_3	S	
Hood and Zhou (1998)	O_3, T	US, LM	
Zhou et al. (2000)	O_3	US	
Ruzmaikin et al. (2007)	O_3, T	S	
Fioletov (2009)	O_3	US	
Eckman (1986a)	O_3, T	S, LM	1D
Brasseur et al. (1987)	O_3, T	S, LM	1D
Summers et al. (1990)	O_3, T	S, M	1D
Brasseur (1993)	O_3, T	S, LM	2D
Chen et al. (1997)	O_3, T	S, M	1D, 2D
Williams et al. (2001)	O_3, T	S, LM	3D
Zhu et al. (2003)	O_3, T	S, LM	2D
Rozanov et al. (2006)	O_3, T	S, LM	3D
Austin et al. (2007)	O_3, T	S	3D
Gruzdev et al. (2009)	O_3, T	S, M, LT	3D

S = stratosphere
US = upper stratosphere
LM = lower mesosphere
M = mesosphere
LT = lower thermosohere

Table 3.2: Selected 27-day solar signal observational and model studies for middle atmospheric ozone.

paper	main data source	compared to...
Allen et al. (1984a,b)	sondes[1]	model
Vaughan (1984)	sondes[1]	model
Connor et al. (1994)	microwave[2]	LIMS[3], NIR[3]
Ricaud et al. (1996)	MLS[3]	model, microwave[2]
Marsh et al. (2002)	HRDI[3]	previous studies
Huang et al. (2008a)	SABER[3]	previous studies
Haefele et al. (2008)	microwave[2]	model

[1]rocket-borne
[2]ground-based
[3]satellite instrument

Table 3.3: Selected studies dealing with diurnal variations in mesospheric ozone.

3.4.2 Diurnal variations

Ground-based observations have a distinct advantage over satellite based measurements when it comes to temporal resolution on an hourly to daily time scale. The satellite only flies over one location on Earth once a day, at its best. Usually it takes a few days before the satellite returns to the same location again. Even if the instrument on board the satellite is able to make one measurement a day, most satellites are in a sun-synchronous orbit, limiting this measurement to the same local time each day. Nonetheless, there are some satellites flying in a non-sun synchronous orbit (also called drifting orbit). The Upper Atmosphere Research Satellite (UARS) (Banks et al., 1978) and the Thermosphere, Ionosphere, Mesosphere, Energetics and Dynamics (TIMED) (Russel III et al., 1999) satellite are two examples. Their local time of measurement for any particular location shifts by a few minutes a day.

Table 3.3 gives a few examples of studies that either used ground-based or orbital instrumentation or models to investigate diurnal variations in ozone. These diurnal variations are mainly driven by the intensity of the incident solar radiation and its variation during the course of a day due to different solar zenith angles. At night

the solar influence is understandably reduced to zero.

The main sources for daytime diurnal variations are the photochemistry that directly relies on the incident radiation, diurnal tides that vertically transport air with a different chemical composition, and changes in temperature that alter the chemical kinetics (rate constants). For detailed information on previous studies, please refer to Sect. 7.2.

Part II

Sources and methods

4 Satellite instrumentation

Civilian achievements like satellite communication and the Global Positioning System (GPS) can be seen as a result of the cold war. The race to the stars between the former Sowjet Union and the United States in the 50s and 60s of the last century encouraged engineers and scientists from both nations to push forward the technology that lay the basis for modern spaceflight and satellite remote sensing today. This Chapter introduces the main sources of satellite data used within this thesis.

4.1 SCIAMACHY on ENVISAT

4.1.1 The environmental satellite ENVISAT

The ENVIronmental SATellite (ENVISAT) was built by an industrial consortium of sixteen member states of the European Space Agency (ESA). It was lifted by the first successful launch of an Ariane-5 rocket from Kourou in French Guiana into a sun-synchronous near polar orbit in descending node on March 1, 2002. Its mean altitude of 800 km was reached soon after launch. The inclination angle is 98.55° and the equator crossing time is 10:00 am local time. Each orbit lasts approximately 100 minutes resulting in slightly more than 14 orbits per day and a ground track repeat cycle of 35 days, every 501 orbits. An image of ENVISAT can be seen in Fig. 4.1. With a total mass of more than 8100 kg and dimensions of 26 m x 10 m x 5 m, ENVISAT is the largest satellite to observe and monitor the Earth's atmosphere, land, ice and ocean. The expected lifetime of the satellite was five years, but mission operation has already been exceeded by more than two and a half years.

ENVISAT is host to ten instruments, the Radar Altimeter 2 (RA-2), the MicroWave Radiometer (MWR), the Doppler Orbitography and Radiopositioning Integrated by Satellite (DORIS) instrument, the Laser RetroReflector (LRR), the Advanced Synthetic Aperture Radar (ASAR), the Medium Resolution Imaging Spectrometer

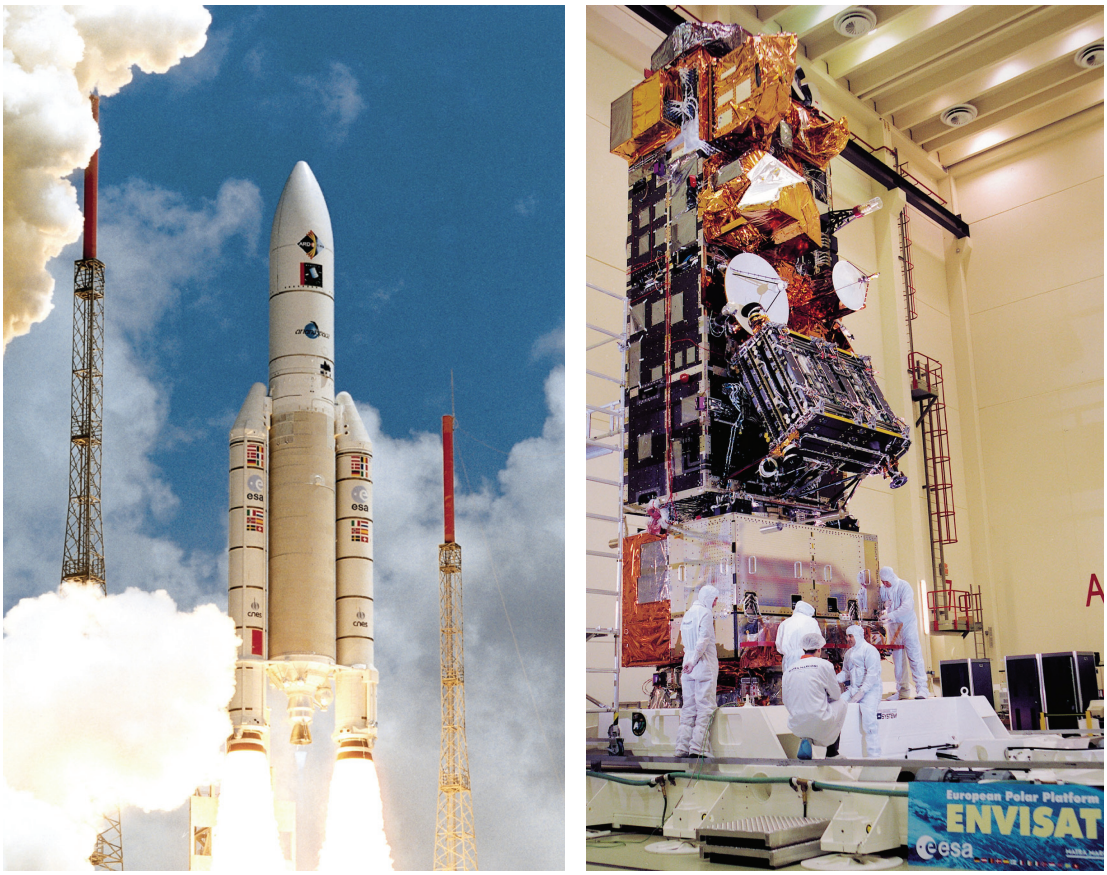

Figure 4.1: Left: Ariane V rocket being launched from Europe's spaceport in Kourou, French Guiana. Right: ENVISAT at the ESTEC (photos courtesy of ESA).

(MERIS), the Michelson Interferometer for Passive Atmospheric Sounding (MIPAS), the Global Ozone Monitoring by Occultation of Stars (GOMOS), and SCIAMACHY, being used in this thesis. The latter three instruments are dedicated atmospheric chemistry instruments, which are complementary to each other with respect to application ranges, spectral coverage, and measurement principles. The spectrometer GOMOS (Bertaux et al., 1991) covers the UV/visible spectral range between 250 and 950 nm and was designed for stellar occultation measurements. Thus it is equipped with a large telescope to improve the signal to noise ratio. The Fourier transform spectrometer MIPAS (Fischer and Oelhaf, 1996) on the other hand covers the infrared spectral region between 4.15 μm and 14.6 μm, and was intended to monitor the stratosphere and mesosphere for minor chemical constituents in the

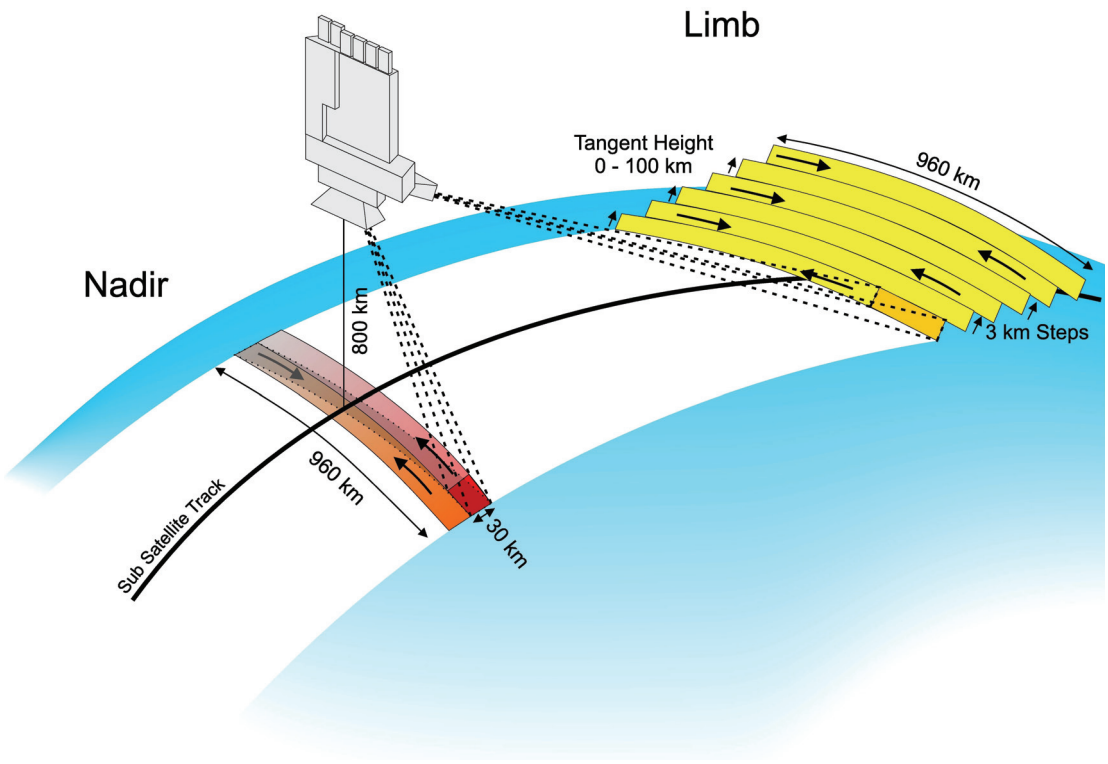

Figure 4.2: Illustration of SCIAMACHY's limb and nadir viewing geometries (figure courtesy of S. Noël).

limb mode.

4.1.2 The SCIAMACHY instrument

The acronym SCIAMACHY originates from the Greek , meaning *fighting* or *chasing shadows*. It is a passive imaging and combined prism/grating spectrometer, which measures the reflected, backscattered and transmitted solar radiation upwelling from the top of the atmosphere (Burrows et al., 1990; Burrows and Chance, 1991; Burrows et al., 1995; Bovensmann et al., 1999; Gottwald et al., 2006). Channels 1 to 6 of SCIAMACHY cover continuously the spectral region from 214 nm to 1773 nm. In addition, channel 7 and 8 cover the spectral range from 1934 nm to 2044 nm and from 2259 nm to 2386 nm, respectively, providing information about infrared absorbing species. Altogether, this allows the retrieval of information on atmospheric gases and trace gases, e.g. O_3, NO_2, O_2, H_2O, CH_4, CO_2, CO, BrO, OClO,

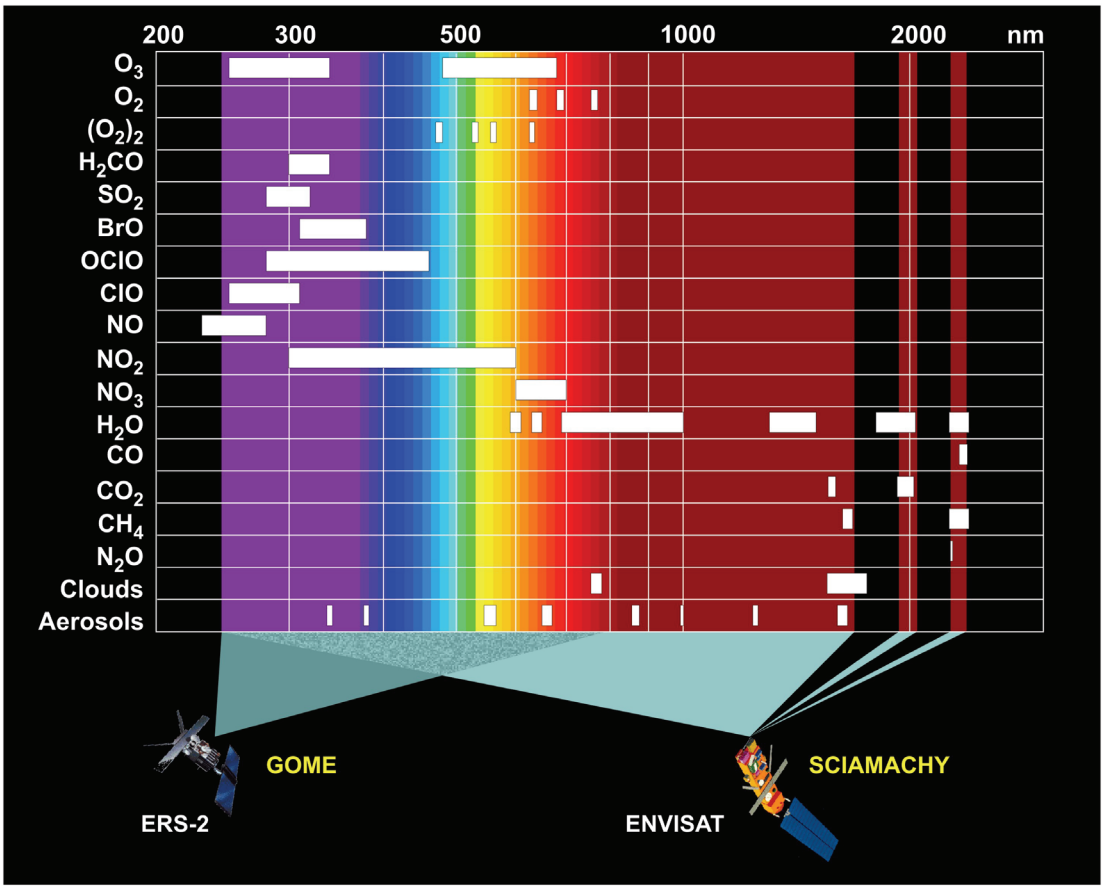

Figure 4.3: Data products of SCIAMACHY and their corresponding spectral ranges (figure courtesy of S. Noël and H. Bovensmann).

SO_2, and IO (figure 4.3). O_3 is being retrieved using information from within the Hartley-Huggins (260 to 305 nm) and Chappuis (525 to 675 nm) ozone absorption band. Besides gases, information about aerosols and clouds can also be retrieved from SCIAMACHY spectral data.

SCIAMACHY is able to perform measurements in three different measuring geometries, from which two are illustrated in Fig. 4.2 (nadir- and limb-view). The first measuring mode is the nadir-view capturing the concentrations of several trace gases in the total atmospheric column on a 960 km wide swath orthogonal to the flight direction (looking directly down). The resolution is about 30 km in flight direction and about 60 km orthogonal to the flight direction. The second mode is the limb-view allowing the retrieval of profiles, i.e. the vertical distribution of trace

gases. The vertical field of view is about 2.6 km in the distance of about 3000 km. Orthogonal to the flight direction the horizontal resolution of the measurements accounts to 240 km across-track. The third and last viewing geometry is the occultation mode, in which SCIAMACHY directly observes the sun or the moon through the atmosphere. The resolution is 30 km horizontally and 2.5 km vertically. The advantage of the occultation mode is its high precision, yet the spatial coverage is limited to middle and high latitudes in the northern hemisphere (solar occultation) and southern hemisphere (lunar occultation).

4.2 SABER on TIMED

4.2.1 The TIMED satellite

The TIMED satellite was successfully launched on July 12, 2001, on board a Delta II rocket from Vanderberg Air Force base, California. An image of the launch can be seen in Fig. 4.4 (left panel). The satellite is flying in a low Earth orbit at approximately 630 km altitude with an inclination of 74.1°. The geometry of the orbit is non sun-synchronous, i.e. a drifting orbit. Thus, the equator crossing time of the TIMED satellite is shifting by approximately 12 minutes each day. It takes the satellite 97 minutes to complete a full orbit.

TIMED serves as platform for four instruments, all of which are designed to monitor the mesosphere and lower thermosphere/ionosphere region of the Earth's atmosphere focusing on altitudes from 50 to 180 km. The instruments are the Global UltraViolet Imager (GUVI), the Solar Extreme ultraviolet Experiment (SEE), the TIMED Doppler Interferometer (TIDI), and SABER. An image of the TIMED satellite and the instruments can be seen in Fig. 4.4 (right panel).

4.2.2 The SABER instrument

The scientific goal of SABER (Mlynczak, 1997; Russel III et al., 1999) is to explore the mesosphere and the lower thermosphere in order to improve the understanding of the fundamental processes governing chemistry, transport, dynamics, and energetics. This includes seasonal, latitudinal, and temporal variations of odd oxygen.

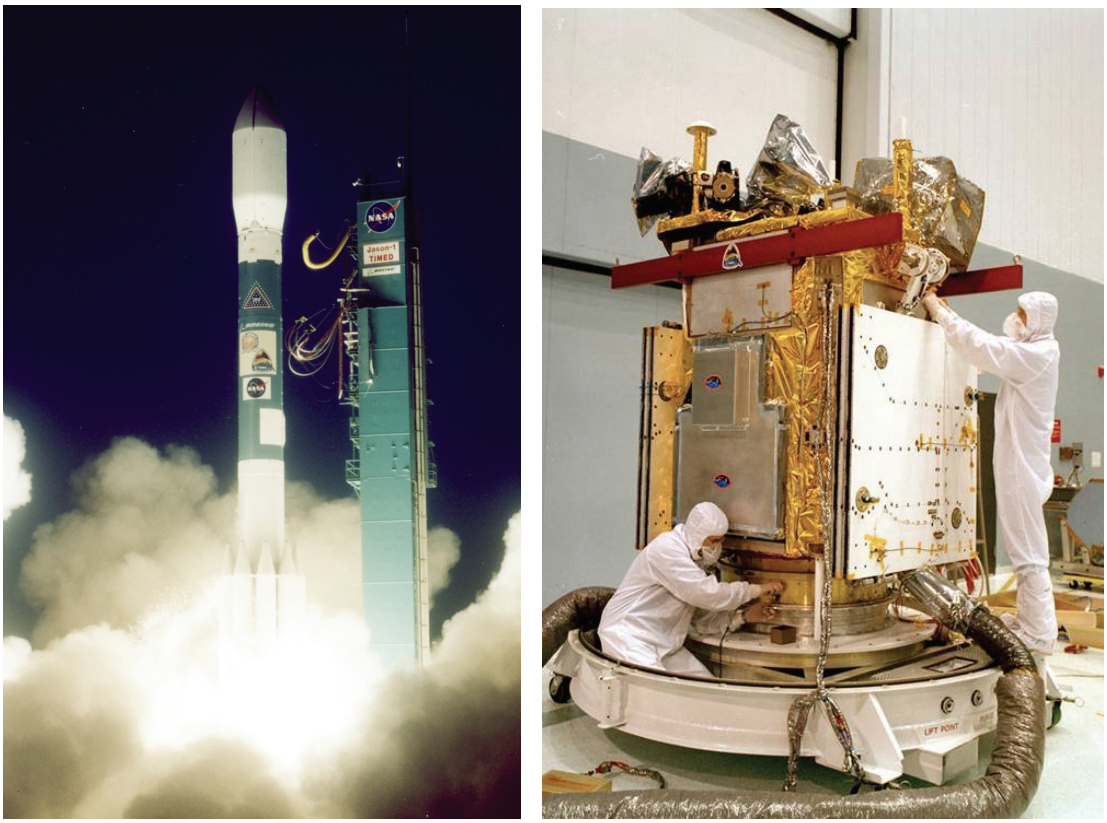

Figure 4.4: Left: Delta II rocket launched at Vanderberg Air Force base in California, U.S.A.. Right: Image of the TIMED satellite. (photos courtesy of NASA)

The SABER instrument itself is a 10-channel radiometer measuring infrared earthshine emissions in the limb mode (cf. Fig. 4.2, SCIAMACHY viewing geometries). Limb scans are performed from the Earth's surface to an altitude of approximately 400 km with an instantaneous field of view (IFOV) of 2 km. The scanning range of the infrared spectrometer ranges from 1.27 μm to 16.9 μm. It has the capability to continuously sound the atmosphere during day and night. The monthly yield is approximately 40,000 profiles between either from 52°S to 83°N or from 83°S to 52°N, depending on the yaw cycle.

The field of view of the instrument is perpendicular to the flight direction of the satellite, being reversed by 180° approximately every 60 days. Therefore continuous observations are limited to a band between 52°S and 52°N.

Variables of interest for this thesis are ozone and temperature retrieved with

SABER. Temperatures are retrieved using atmospheric CO_2 emission at 15 μm. As for the ozone, two products exist: One from the 9.6 μm O_3 emissions and the other one via the 1.27 μm dayglow emissions of the exited $O_2(^1\Delta)$, thus limited to daytime and also to altitudes above 50 km. Some species and variables retrieved from SABER infrared spectra are summarized in Table 4.1.

species	wavelength [μm]	application	altitude [km]
CO_2	14.9, 15.2	T, density, IR cooling rates, P(z), non-LTE	10-130
O_3	9.6	O_3 conc. cooling rates, solar heating, chemistry and dynamics	15-100
$O_2(^1\Delta)$	1.27	O_3 conc. (day), inferred [O] at night, energy loss for solar heating efficiency	50-105
CO_2	4.3	CO_2 conc., mesosphere sol. heating, tracer	85-150
OH	2.0, 1.6	HO_y chem., chem. heat source, dynamics, energy loss for solar heating efficiency	80-100
NO	5.3	thermosphere cooling, NO_x, chemistry	90-180
H_2O	6.9	HO_y source gas, dynamical tracer	15-80

Table 4.1: SABER measurements and applications.

5 Statistical approaches

The major benefit scientists have from satellite remote sensing is the vast amount of data available. Ground-based observations only produce one profile per week, maybe per day, for a single location (e.g., a profile from an ozone sonde), at its best. Satellite data often covers the whole globe within 1 to 6 days, offering hundreds to thousands of profiles per day. This data needs to be converted into information, that can easily and quickly be comprehended by the people interested, before scientific conclusions can be drawn. Statistics help to reduce data and to present it in a concise manner. The main approaches used in this thesis are summarized in this Chapter.

5.1 Correlations

5.1.1 Correlation coefficient

Correlations are a form of comparing two variables with each other. Given, e.g., two random variables X and Y with x_i and y_i being the pairs of N measurement points (x_1,y_1), ..., (x_N,y_N), and $\overline{x}$ and $\overline{y}$ the sample mean values, respectively, the corresponding correlation coefficient r ∈ [-1,1] is the ratio of the covariance of the sample populations to the product of their standard deviations σ:

$$r = \frac{cov(X,Y)}{\sigma_X \cdot \sigma_Y} = \frac{\sum(x_i - \overline{x})(y_i - \overline{y})}{[\sum(x_i - \overline{x})^2(y_i - \overline{y})^2]^{1/2}} . \tag{5.1}$$

The greater | r | is, the better both variables are correlated. When r is negative, we speak of anti-correlation.

5.1.2 Cross-correlation function

In case two time series are known to be linear dependent on each other, but the correlation coefficient is small, the CC function might help to identify a time-lag τ between both variables that increases the correlation. The correlation between both time series as a function of time lag τ is called the cross-correlation function. The CC function r(τ), ideally peaks at the time-lag with the highest correlations between both time series. The CC is used in Sect. 6.4 of this thesis.

5.1.3 Auto-correlation function

The auto-correlation function is a cross-correlation function with itself. It is used to identify repeating or periodic signals in a series of values. An example of a auto-correlation function is given in Fig. 5.1. For zero time lag the autocorrelation function is always 1. Recurring peaks off to the wings indicate dominant frequencies in time series. In case of the combined GOME and SCIAMACHY (GOMESCIA) Mg II index, a proxy for solar UV irradiance variation (cf. Sect. 6.3.2), supplemented with Solar Backscatter UltraViolet (SBUV) and SOLSTICE data, the 11-year solar cycle and the solar rotational period (27-days) can be identified.

5.1.4 Significance tests and spurious correlation

Spurious correlations may occur if two variables correlate, but lack a causal connection. An often used example for a spurious correlation is the connection between the human birth rate within a certain region and the amount of nesting storks in the same region. To make sure both variables are not randomly connected and to gain some level of confidence, two simple significance tests can be performed.

Assuming that for the limit of infinite measurements the correlation coefficient of two uncorrelated variables x and y will be r = 0 (Null Hypothesis H_0), the likelihood for a finite number of measurements that the correlation coefficient r exceeds the value r_0 is given by the so called *p-value* ($P_N \in [0,1]$) (Taylor, 1996):

$$P_N(|r| \geq r_0, H_0) = \frac{2\Gamma[(N-1)/2]}{\sqrt{\pi}\Gamma[(N-2)/2]} \int_{|r_0|}^{1} (1-r^2)^{(N-4)/2} dr \ , \qquad (5.2)$$

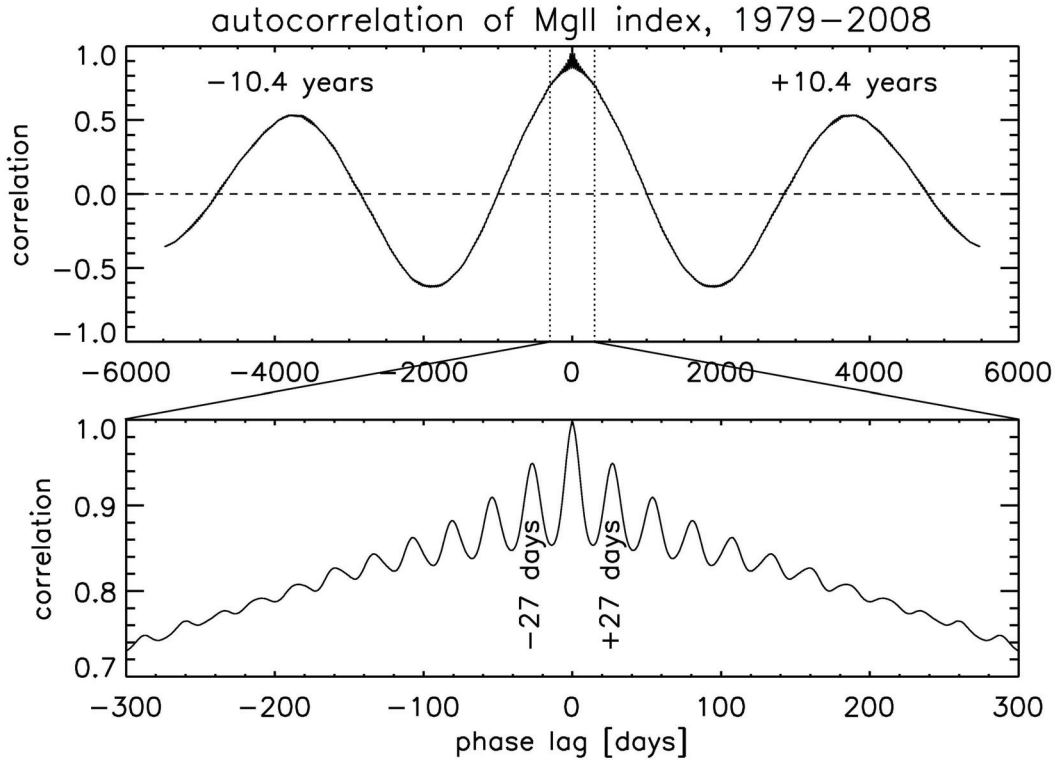

Figure 5.1: Autocorrelation function of the composite Mg II index (1979-2008). Recurring peaks can be found at 10.4 years (11-year solar cycle, upper plot) and at 27 days (solar rotation period, lower plot).

with Γ being the Gamma-function.

Another easily applicable method to gain some confidence whether two series of variables x_i and y_i are indeed not randomly connected is to take the standard deviation σ of the slope s from a linear regressional. The following criteria may be used: $s > 2\sigma$.

5.2 Discrete Fourier transform and FFT

The forward discrete-Fourier transform (DFT) is given as (taken from Bracewell, 2000)

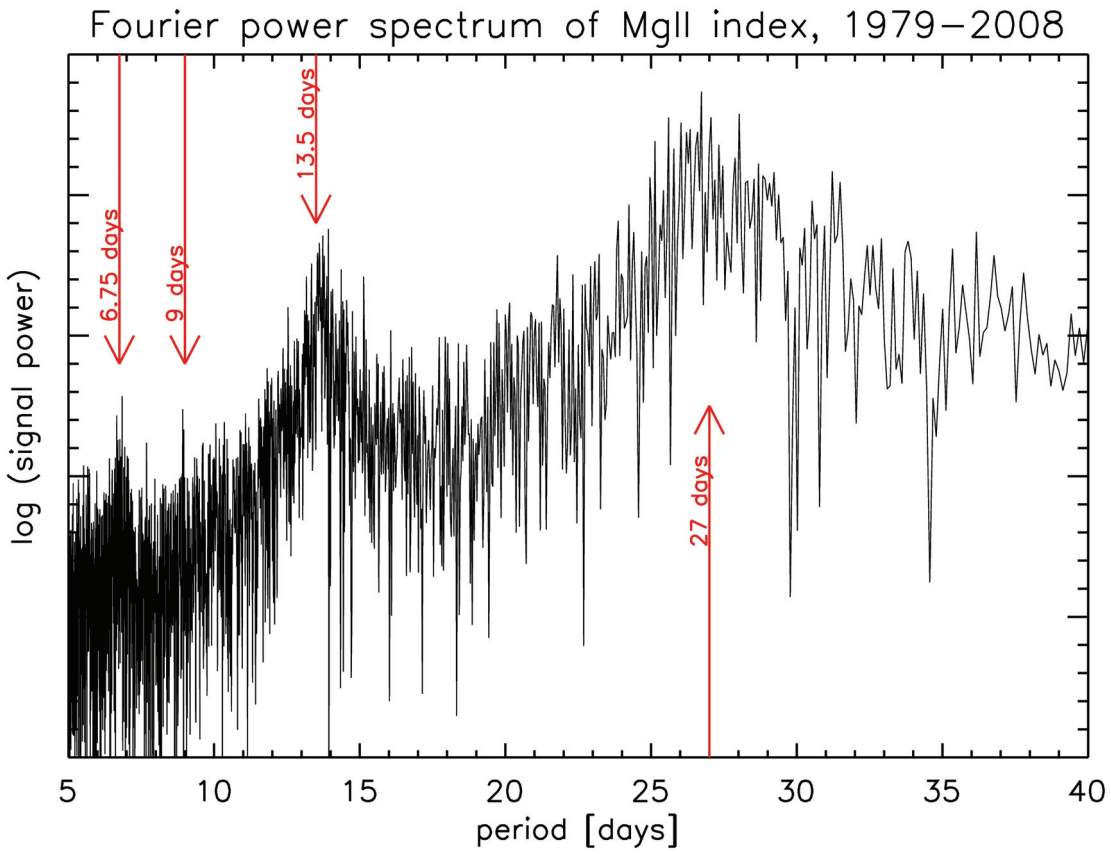

Figure 5.2: Fourier power spectrum of the composite Mg II index (1979-2008). Spikes at 27 days (solar rotations period) as well as the first (13.5 days), the second (9 days) and the third (6.75 days) harmonics are visible.

$$F(\nu) = \frac{1}{N}\sum_{\tau=0}^{N-1} f(\tau) \cdot e^{-i2\pi(\nu/N)\tau} , \tag{5.3}$$

with the time variable τ and the frequency ν/N measured in cycles per sampling interval.

The reverse DFT is given as followed:

$$f(\tau) = \sum_{\nu=0}^{N-1} F(\nu) \cdot e^{i2\pi(\nu/N)\tau} . \tag{5.4}$$

For computational purposes, the fast-Fourier transform (FFT) is commonly used. The FFT is a DFT that uses factorized transform matrices to save computational

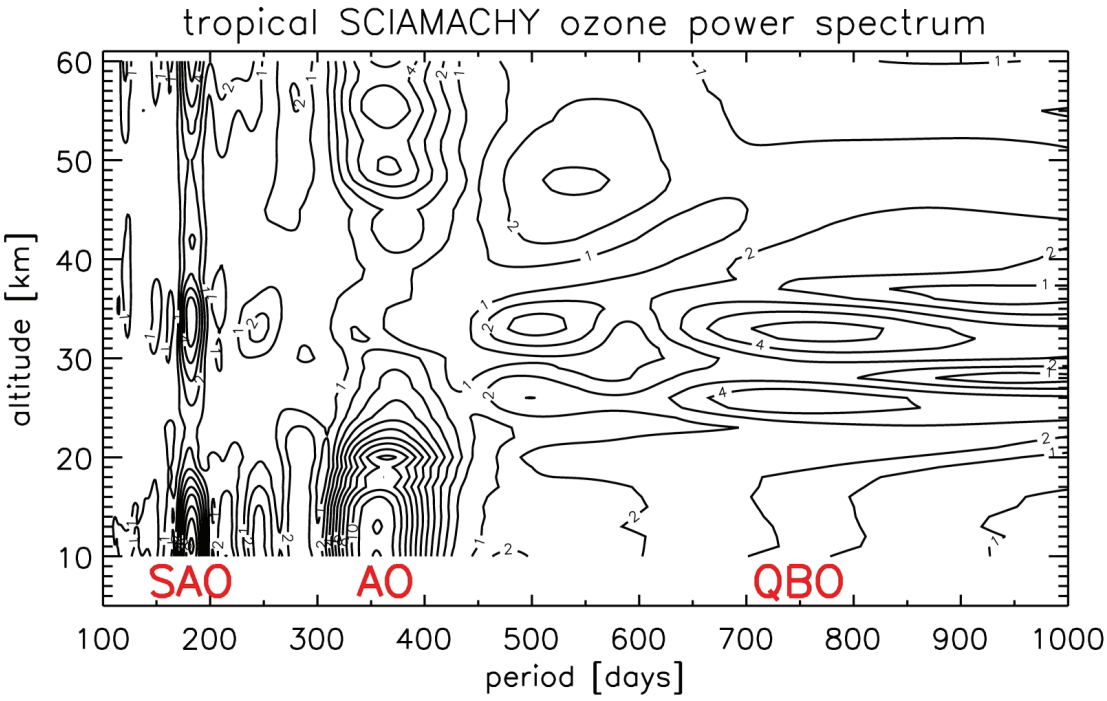

Figure 5.3: Power spectrum of tropical SCIAMACHY ozone obtained via individual regression fit of periods shown.

resources. Another way to understand the concept of a FFT, without filling books with explanations, is to think of the FFT as a DFT that is split into two transforms to potentially save 50 % of the time needed for computation.

Figure 5.2 shows the power spectrum of the Fourier transformed composite Mg II index (1979-2008). F(ν) is peaking at the expected 27 days (solar rotation period), but also at 13.5, 9, and 6.75 days, presumably the first, second and third harmonics of the 27-day signal.

5.3 Regression analysis

Sinusoidal functions can be fitted in a multivariate least squares approach to time series, e.g. tropical SCIAMACHY ozone, in order to retrieve annual oscillation (AO), semi-annual oscillation (SAO), and quasi-biennial oscillation (QBO) variations as follows (Fahrmeir et al., 2004):

$$\vec{\beta} = (\mathbf{X}^T\mathbf{X})^{-1}\mathbf{X}^T\vec{Y} \; . \tag{5.5}$$

The vector $\vec{Y}$ contains the time series to be investigated, the matrix $\mathbf{X}$ is subscripted with the functions to be fitted to the time series, and the vector $\vec{\beta}$ contains the regression parameters (A, B, C, D) as follows,

$$R(t) = A + Bt + \sum_i [C_i \, sin(\frac{2\pi t}{T_i}) + D_i \, cos(\frac{2\pi t}{T_i})] \; , \tag{5.6}$$

with the offset A and the trend term Bt. Done for all periods T between 100 and 1000 days results in a power spectrum as shown in Fig. 5.3. The AO, the SAO, and the QBO can be identified. The amplitude in Figs. 5.3 and 5.4 is obtained as being

$$Amp_i = \sqrt{C_i^2 + D_i^2} \; . \tag{5.7}$$

In addition to the AO and SAO periods (365 and 183 days, respectively), selected QBO periods from a study by Fischer and Tung (2008) that are characteristic for the SCIAMACHY observation period (2002 to today) are fitted: T = 854, 823, 793, 762 days. The resulting AO, SAO, and QBO fits are shown for SCIAMACHY ozone in Fig. 5.4, a and b, respectively. The AO in Fig. 5.4a is most pronounced below 27 km and above 45 km altitude, being a SAO signal in between. The QBO signal in its typical, with altitude shifting pattern is the strongest below 35 km altitude (Fig. 5.4b).

Many publications deal with the relationship between the 11-year solar cycle and QBO (e.g., Labitzke, 2004; Gabis and Troshichev, 2004; Camp and Tung, 2007). It has been shown that the influence of the 11-year solar cycle on ozone is being modulated by the phase of the QBO. The solar signal in the tropical stratosphere appears to be stronger during the easterly phase of the QBO. Covering more than two QBO cycles, the SCIAMACHY ozone time series might be used to infer a QBO phase dependent modulation of the stratospheric 27-day ozone signal.

5.4 Continuous wavelet transform

The CWT can be used if the temporal resolution offered by the standard Fourier transform is insufficient and a temporal resolution of the investigated time series is

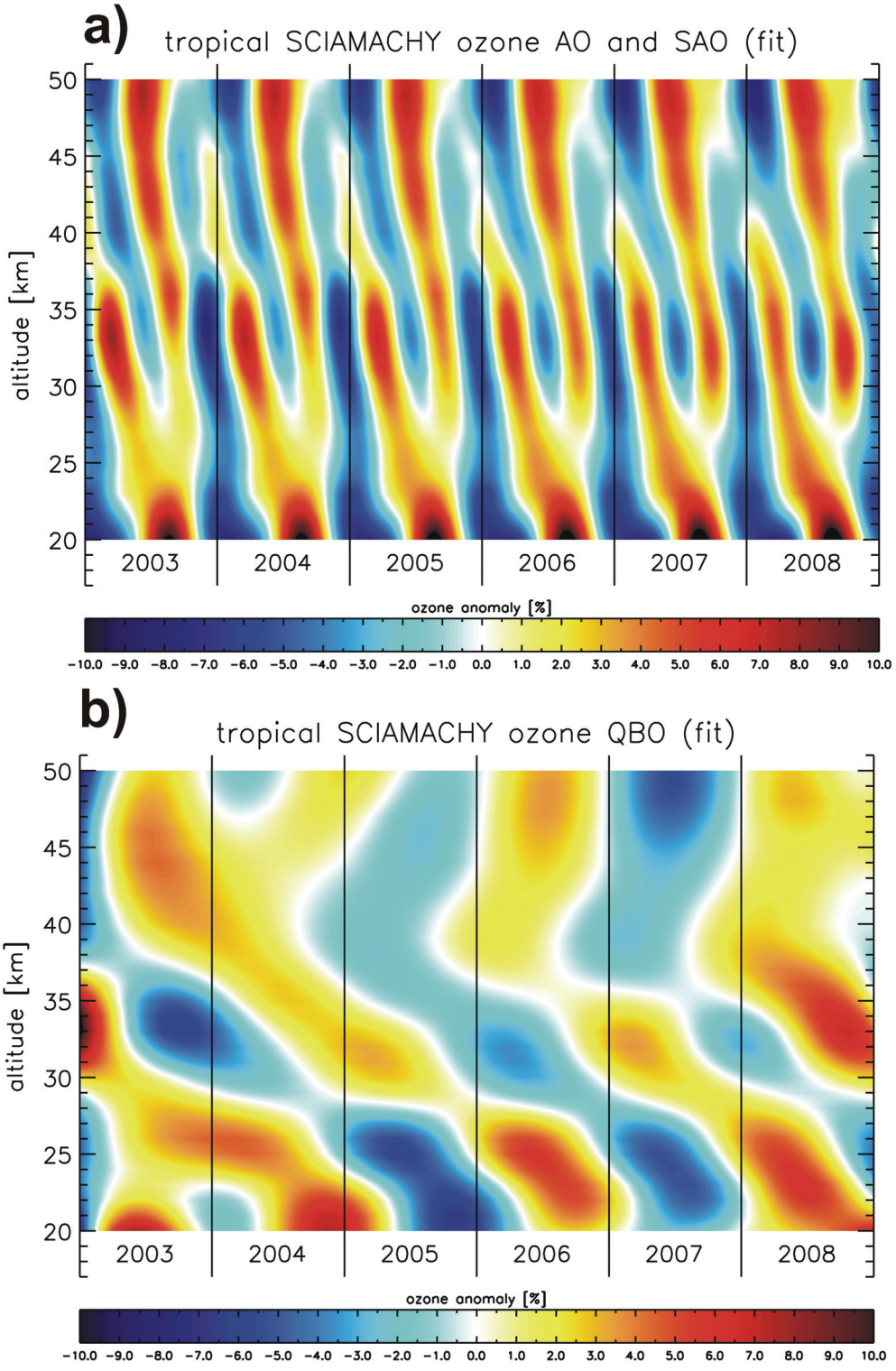

Figure 5.4: Amplitudes of SCIAMACHY ozone variability: a) AO and SAO signal, b) QBO signal.

name	$\Psi_0(\eta)$
Morlet	$\pi^{-\frac{1}{4}} \cdot e^{i\omega_0\eta} \cdot e^{-\frac{\eta^2}{2}}$
Mexican Hat (Gaussian)	$e^{\frac{-\eta^2}{2\omega_0^2}}$
Paul	$(1-i\eta)^{-(\omega_0+1)}$

Table 5.1: Examples of wavelet mother functions.

additionally wanted.

For a discrete sequence x_n of a time series x(t) the wavelet transform is given as (Torrence and Compo, 1998)

$$W_n(s) = \sum_{n'=0}^{N-1} x_{n'} \cdot \Psi^* \cdot \left[\frac{n' - n}{s}\right] \delta t \,, \tag{5.8}$$

where the complex conjugate wavelet Ψ^* is scaled with s and translated by n′-n to convolute the discrete sequence x_n. The resulting power spectrum of the wavelet transform is represented by $| W_n(s) |^2$.

The wavelet $\Psi_0(\eta)$ is called mother wavelet. For the choice of the mother wavelet certain rules apply. One is that the mean of the wavelet function has to be zero and the other is that the wavelet has to be localized in both time and frequency space. The Morlet wavelet serves here as an example, because it was used in Chapter 6 of this thesis in the time series analysis of SCIAMACHY ozone. It is given as a plane wave constrained by a Gaussian function:

$$\Psi_0(\eta) = \pi^{-\frac{1}{4}} \cdot e^{i\omega_0\eta} \cdot e^{-\frac{\eta^2}{2}} \,, \tag{5.9}$$

with the non dimensional frequency ω_0, which allows the *adjustment* of time vs. frequency resolution of the transformed time series. Within this thesis ω_0 was

chosen to be 24. An overview over some common wavelets is given in Table 5.1. The corresponding wavelets are plotted in Fig. 5.5 for different parameters ω_0. The application of the CWT was also done for the Mg II index. The results can be seen in Fig. 6.9 in Chapter 6.

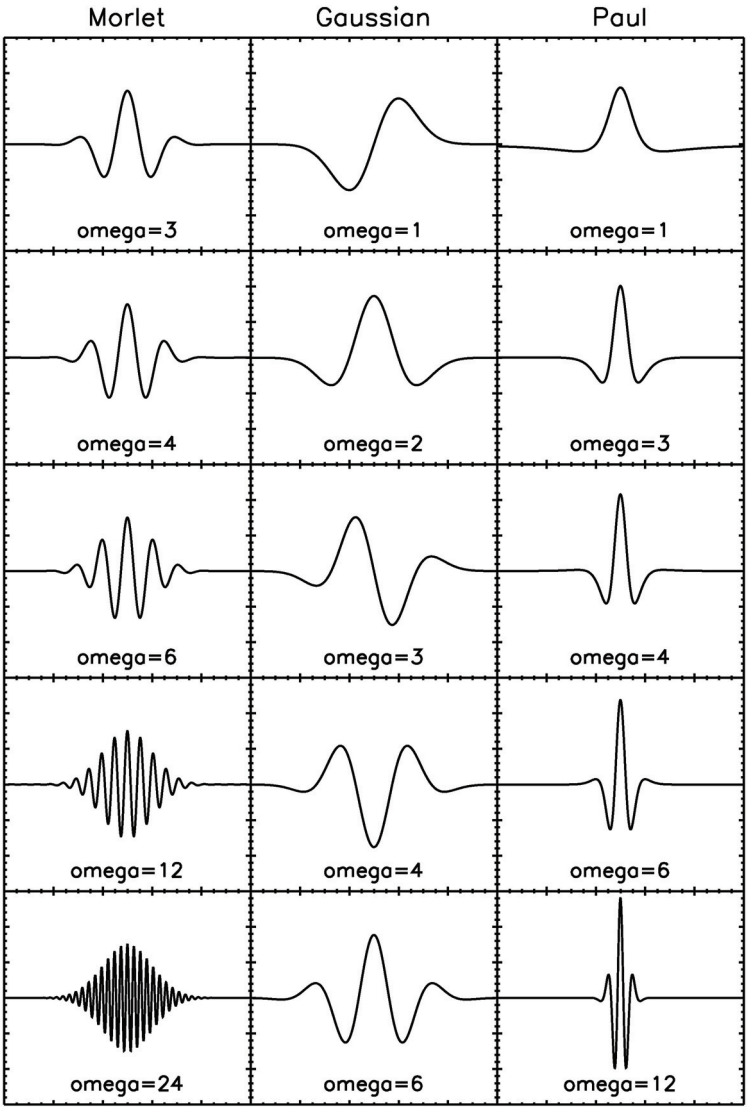

Figure 5.5: Illustration of Morlet, Mexican Hat (Gaussian) and Paul wavelets with different orders ω_0.

Part III

Results

6 27-day solar rotation signal in stratospheric ozone [1]

6.1 Abstract

Here the modulating nature of the 27-day solar rotation forcing on stratospheric ozone is investigated using a new ozone profile data set from SCIAMACHY. CWT, FFT, and CC have been applied to SCIAMACHY ozone in the tropics ($< 20°$ latitude) between 20 and 60 km altitude. The maximum correlation between Mg II index and ozone is weaker during the maximum of solar cycle 23 ($r = 0.38$) than in the previous two solar cycles that have been investigated in earlier studies using different data sets. The magnitude of the ozone signal is highly time dependent and may vanish for several solar rotations even close to solar maximum conditions. The FFT analysis reveals, besides the 27-day signal, several frequencies close to 27-days. The ozone sensitivity (ozone change in % per % change in 205 nm solar flux) is on average about 0.2 %/% above 30 km altitude and smaller by about a factor of two compared to earlier studies. For selected three month periods the sensitivity may rise beyond 0.6 %/% in better agreement with earlier studies. The analysis of the 27-day solar forcing was also carried out with stratospheric temperature data from the ECMWF operational analysis. Although direct radiation effects on temperature are weak in the upper stratosphere, temperature signals with statistically significant periods in the 25-35 day range similar to ozone could be found with the applied methods.

[1] Sections 6.1 to 6.6 have been accepted for publication as Dikty, S., Weber, M., von Savigny, C., Sonkaew, T., Rozanov, A., and Burrows, J. P.: Modulations of the 27-day solar rotation signal in stratospheric ozone by SCIAMACHY (2003-2008), J. Geophys. Res., doi:10.1029/2009JD012379; with minor modifications.

6.2 Introduction

The differential rotation of the sun causes regions with intensified radiative output to appear and disappear within the field of view of the Earth. Depending on the solar latitude the sun's rotational period varies from 25 days near the equator to 35 days close to the poles (Lean, 1991). The frequency and latitudinal distribution of the sun spots and active regions also vary with the 11-year solar cycle and modulate the radiative output of the sun. The solar variation on the 11-year time scale has been shown to cause 2-3 % variability in tropical ozone at altitudes of approximately 40 km. This has been concluded from satellite observations (e.g., Hood, 2004; Fioletov, 2009; Remsberg, 2008; Randel and Wu, 2007; Soukharev and Hood, 2006) and confirmed by model studies (e.g., Marsh et al., 2007; Sekiyama et al., 2006; Langematz et al., 2005). In general, the models show a lower altitude for the maximum ozone sensitivity to solar forcing than observations. Differences between observations and model still remain for the lower stratosphere. Fioletov (2009) estimated from the 27-day ozone response the 11-year ozone response with the help of a statistical model. He also emphasized the fact that only three complete periods of the 11-year solar cycle were covered by satellite observations so far. In addition, the life span of a single satellite instrument is generally far less than one solar cycle and instrumental biases between different ozone profile data sets complicate statistical analysis of decadal variations.

The influence of the 27 day solar rotation on ozone has already been investigated by Hood (1986) in the 1980s using SBUV ozone measurements during solar maximum of solar cycle 21 (1979-1981). He found the ozone sensitivity at 45 km to be slightly more than 0.4 % per 1 % change in the 205 nm flux. Further investigations with different satellite data sets and model outputs covering other time periods followed (e.g., Hood and Zhou, 1998; Zhou et al., 2000; Williams et al., 2001; Rozanov et al., 2006; Ruzmaikin et al., 2007; Fioletov, 2009). Especially Fioletov (2009) examined a time series of ozone measurements from various satellite instruments from the SBUV series from 1979 to 2006. Compared to Hood (1986) the ozone response is in good agreement (0.4 %/%). Austin et al. (2007) and Gruzdev et al. (2009) compared the 27-day ozone variability determined by Chemistry-Climate-Models (CCMs) with satellite measurements and were able to

verify the observations in magnitude (0.4 to 0.5 %/%) but found the maximum ozone sensitivity slightly lower in altitude (approx. 40 km) in the model simulations. A detailed summary of 27-day ozone variations from past observations can be found in Gruzdev et al. (2009). Ruzmaikin et al. (2007) used the empirical mode decomposition on Microwave Limb Sounder (MLS) ozone (2004 to 2006) to show the altitude/latitude distribution of the 27-day mode. He found the highest 27-day amplitude to be in the winter high latitudes of the upper stratosphere. The term *27-days* will be used throughout this chapter to describe variations on time scales of 25 to 32 days period that are likely related to solar rotational variations.

The scope of this chapter is to investigate short-term variations (approximately 27-days) in stratospheric ozone. Dominant frequencies may vary according to the section of the time series investigated. This makes it necessary to introduce new frequency analysis approaches, such as the CWT, in addition to the more traditional approaches. A second motivation is that a new ozone profile data set is available from SCIAMACHY that spans a large part of the recent solar cycle 23 and beginning of the current cycle and is well suited for studies on short-term solar variations.

The FFT (Bracewell, 2000), the CC and the already mentioned CWT (Torrence and Compo, 1998) is used for the presented time series analyses of SCIAMACHY limb scatter ozone and ECMWF temperature profiles. The SCIAMACHY data have a high spatial sampling with global coverage of the sunlit earth achieved within six days, which makes this data set valuable for studying short-term variability in the middle to upper stratosphere. The CWT in particular has become more popular over the last two decades. While the FFT and CC are common tools in time series analysis, their main disadvantage is that the time series is treated as a whole and temporal fluctuations in the signal period cannot be detected. The CWT offers a higher temporal resolution with a combined adjustment between time and frequency resolution depending on the choice of wavelet and its order. Within a given time series the connection between ozone and solar radiation is sometimes not well-defined and this can be studied in a suitable way with the CWT in combination with other frequency analysis tools.

The FFT, CC, and CWT have been applied to both the tropical ozone profiles and the Mg II index, the latter being a common proxy for solar activity and irradiance

changes. Both quantities were derived from SCIAMACHY observations (Skupin et al., 2005; von Savigny et al., 2005b; Sonkaew et al., 2009). In order to identify possible mechanisms for a solar rotation signal on stratospheric ozone, it is worthwhile to look at corresponding stratospheric temperature variations; e.g., a recent study by Ruzmaikin et al. (2007) showed 27 day variations in stratospheric temperatures. Gruzdev et al. (2009, Fig. 14, and references therein) nicely summarize earlier findings regarding the temperature sensitivity in the stratosphere observed by Stratospheric and Mesospheric Sounder (SAMS) and MLS, and compare these findings with their 3D model output. Both, observations and model show sensitivities in the range of 0.02 to 0.04 %/% in stratospheric temperatures. These results are in agreement with findings from Brasseur et al. (1987), who used a 1D model with a sinusoidal 27-day solar forcing and compared their results to SAMS observations reported in Keating et al. (1987). The same frequency analyses FFT, CC and CWT were, therefore, also applied to stratospheric temperatures from the ECMWF operational analyses during the SCIAMACHY observation period (2003-2008) to allow a better evaluation of the indirect effects of solar-ozone interactions and to identify possible links to temperature dependent ozone chemistry. Variations in stratospheric temperatures, if correlated with corresponding ozone changes on such a short-term time scales, may also be indicators for dynamical responses to solar forcing in addition to chemical and radiative effects.

6.3 SCIAMACHY and ECMWF data

6.3.1 SCIAMACHY ozone data

A comprehensive summary of the SCIAMACHY instrument can be found in Bovensmann et al. (1999). SCIAMACHY is one of ten instruments on board the European satellite ENVISAT, which was launched in March 2002. ENVISAT is in a sun-synchronous orbit with an inclination of 98.5°, a mean altitude of 796 km and has a period of 100 minutes thus performing about 14 to 15 orbits per day. The vertical resolution of the retrieved ozone profiles - as given by the full width at half maximum of the averaging kernels - is about 4.5 km, the vertical sampling approximately 3.3 km, and its IFOV of 2.8 km. The limb spectra are measured in

the flight direction of the satellite. The overall yield is roughly 10,000 profiles per month. Except for polar night regions, global coverage is achieved within 6 days. The local time for tropical SCIAMACHY observations is close to 10 am.

SCIAMACHY is an 8-channel spectrometer covering the spectral range from 240 nm to 2380 nm. It uses different viewing geometries for retrieving total trace gas columns (nadir) and profiles (limb and solar/lunar occultation) (Bovensmann et al., 1999). The limb retrieval uses wavelengths in the Hartley-Huggins (264, 267.5, 273.5, 283, 286, 288, 290, and 305 nm) and Chappuis (525, 600 and 675 nm) ozone absorption band and covers altitudes from 10 to 60 km. The multiple scattering radiative transfer model SCIATRAN 2.0 (Rozanov et al., 2005b) is used in the forward modeling as part of the optimal estimation inversion. The ozone profile data was retrieved on a vertical one km altitude grid, which provided more stable profile retrievals compared to a coarser resolution. A complete description of the ozone limb retrieval is given by von Savigny et al. (2005b) and Sonkaew et al. (2009). The version 2.1 ozone profile data set derived from SCIAMACHY limb observations are used here. Earlier versions including only the Chappuis wavelengths in the retrieval (von Savigny et al., 2005b), thus limiting retrieved altitudes up to 40 km, were in good agreement with Halogen Occultation Experiment (HALOE) and Stratospheric Aerosol and Gas Experiment (SAGE) II (within 10 %). However, earlier data suffered from a varying shift in the tangent height (von Savigny et al., 2005a). In the new data version, the tangent height offset has successfully been corrected and agreement of the limb ozone profiles with other satellite data (HALOE and SAGE II) has now improved to better than 10 % on average up to 50 km altitude (Mieruch et al., manuscript in preparation).

6.3.2 Solar proxy - Mg II index

For the CC analysis a suitable proxy for solar UV irradiance variation is needed. Hood (1986) used the 205 nm irradiance as a solar proxy since molecular oxygen is primarily photodissociated at wavelengths between 183-205 nm in the upper stratosphere. The Mg II index is given by the core-to-wing ratio of the Mg II h and k doublet at 280 nm and was shown to correlate well with solar UV irradiance changes throughout the UV region down to 30 nm (DeLand and Cebula, 1993;

Weber, 1999; Viereck et al., 2004). The Mg II absorption originates in the sun's photosphere, while the narrow emission core stems from the chromosphere above. The chromospheric solar activity varies with temperature and surface magnetic activity and is, therefore, a good measure of solar UV irradiance variation. Since it is a ratio, it is insensitive to the optical degradation of the measuring instrument. A 1 % change in the GOMESCIA Mg II index corresponds to a 0.61 % change in the solar flux at 205 nm. In addition to atmospheric measurements, SCIAMACHY provides daily solar irradiance measurements from which a daily Mg II index can be derived (Skupin et al., 2005). This Mg II index has been combined with data from SBUV (1979-1992), Solar Ultraviolet Spectral Irradiance Monitor (SUSIM) (1992-1995), and Global Ozone Monitoring Experiment (GOME) (1995-2001) to obtain a composite Mg II index spanning nearly three decades (Weber, 1999; Viereck et al., 2004). The composite Mg II index, also called GOMESCIA Mg II index, from GOME and SCIAMACHY solar irradiance measurements from 1995 to 2008 (solar cycle 23) is shown in Fig. 6.1. The 27-day solar rotational variations during solar maximum are almost half the magnitude of an entire 11-year solar cycle (Weber, 1999; Skupin et al., 2005).

6.3.3 ECMWF temperatures

Stratospheric temperature data are taken from the ECMWF operational analysis available at 1.5° by 1.5° spatial resolution. The main source of data for ECMWF stratospheric temperatures are from the Advanced Microwave Sounding Unit-A (AMSU-A), the Atmospheric Infrared Sounder (AIS) and the High-resolution Infrared Radiation Sounder (HIRS). Observational data up to approximately 50 km are being assimilated. Zonal mean data for the latitude band 20°S to 20°N were calculated from 20 to 60 km in steps of one km. Fig. 6.2a shows the CC between unfiltered stratospheric ozone and temperatures from 20 to 60 km. Ozone and temperature are highly anti-correlated above 35 km peaking at 40 km ($r < -0.85$) with approximately zero time lag, and highly correlated below 28 km peaking at 20 km ($r > 0.9$) with a time lag of approximately 20 days. The origin of the high absolute correlation comes mainly from the seasonal variation in stratospheric temperatures and ozone (concluded from the CC of seasonal fits to ECMWF temperatures and SCIAMACHY

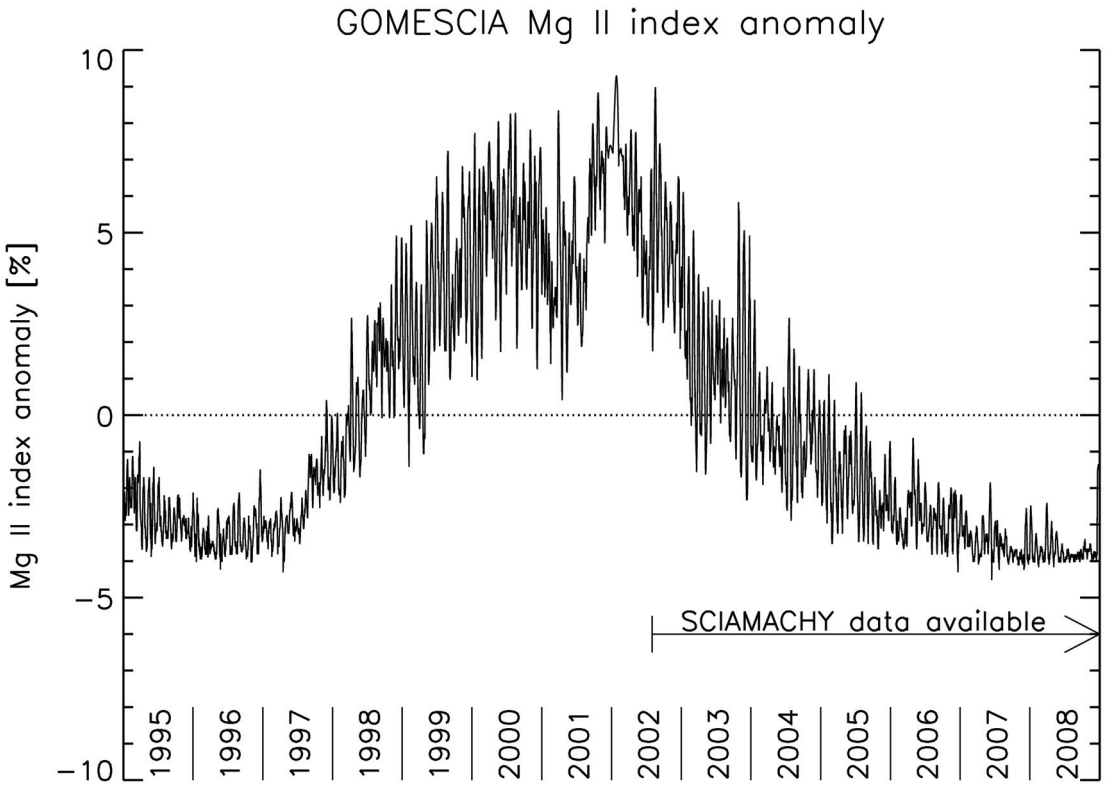

Figure 6.1: Composite Mg II index anomaly from GOME and SCIAMACHY solar observations from 1995 to 2008. The SCIAMACHY observation period covers the declining phase of solar cycle 23 from 2003 to 2008.

ozone showing a similar picture, but not shown here). Fig. 6.2b now shows the CC between the ozone and temperature with the seasonal cycle removed. Above 30 km anti-correlation is as low as -0.6 and below 30 km the correlations are up to 0.5, in both cases for zero time lag. The anti-correlation in the upper stratosphere is mainly caused by the negative temperature dependency of the ozone production ($O_2 + O + M \rightarrow O_3 + M$) in the Chapman reaction cycle, decreasing the O/O_3 ratio with decreasing temperature (Rosenfield et al., 2002). In the lower stratosphere the lifetime of ozone is longer, atmospheric transport and the catalytic ozone loss cycles play a larger role. In addition to the impact on ozone production, the ozone loss ($O + O_3 \rightarrow 2O_2$) is significantly slowed down with decreasing temperature (Sander et al., 2005; WMO, 2007).

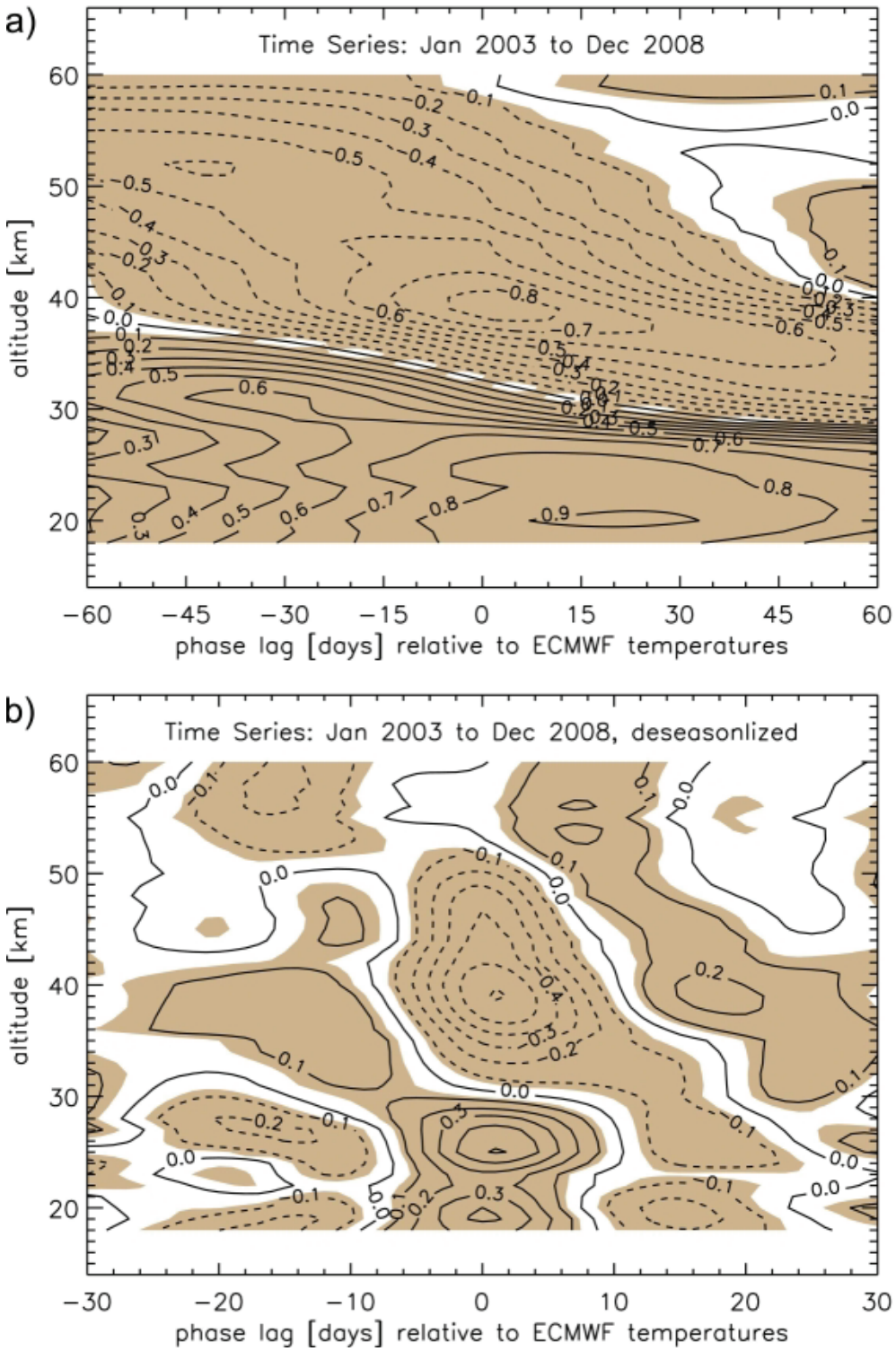

Figure 6.2: CC of tropical zonal mean SCIAMACHY ozone and ECMWF temperature anomalies (20°S to 20°N) between 20 and 60 km with a) the unfiltered time series and b) after the seasonal cycle has been removed. The grey shading indicates statistical significance being greater than 95 %.

6.4 Analysis approaches and results

6.4.1 Ozone data preprocessing

All profiles between 20°S to 20°N latitude for a given day were selected and an area-weighted zonal mean profile was calculated. Days with less than ten profiles within this latitude band were treated as days with no data. Daily zonal mean SCIAMACHY ozone profiles were derived from 20 km to 60 km altitude in steps of one km. Ozone anomalies were calculated by subtracting the long-term mean from 2003 to 2008. Major outliers in the time series are identified as being outside the 3σ value from the zonal mean at each altitude and are rejected. Anomalies in ozone as well as temperature from January 2003 to December 2008 are illustrated for the 20-60 km altitude range in Fig. 6.3. Annual variations in ozone are dominant above 40 km and a QBO signal can be identified below (Huang et al., 2008b; McCormack et al., 2007).

Filtering of the time series becomes necessary to separate known frequencies from a potential 27-day signal. Otherwise these frequencies may dominate the time series. The first filter is the subtraction of a 6-day running mean (smoothing) to eliminate fluctuations on very short time scales (Fig. 6.3). Six days were chosen because SCIAMACHY fully covers the earth in 6 days and contributions from all longitudes were desired. Choosing an even number of days for the running mean shifted the time series by half a day. This shift has also been applied to the solar proxy and ECMWF temperatures. Before the 6-day running mean was applied, data gaps were closed using a spline interpolation. Data gaps normally occur due to maintenance operations on the instrument or satellite platform and rarely last more than a few days. In case of the larger data gap between January 29 and February 23, 2005, the spline interpolation introduced an artifact in such a way that the amplitude is overestimated in the frequency analysis. The 6-day running mean was applied to all time series used in this chapter before any other filter or analysis method was applied.

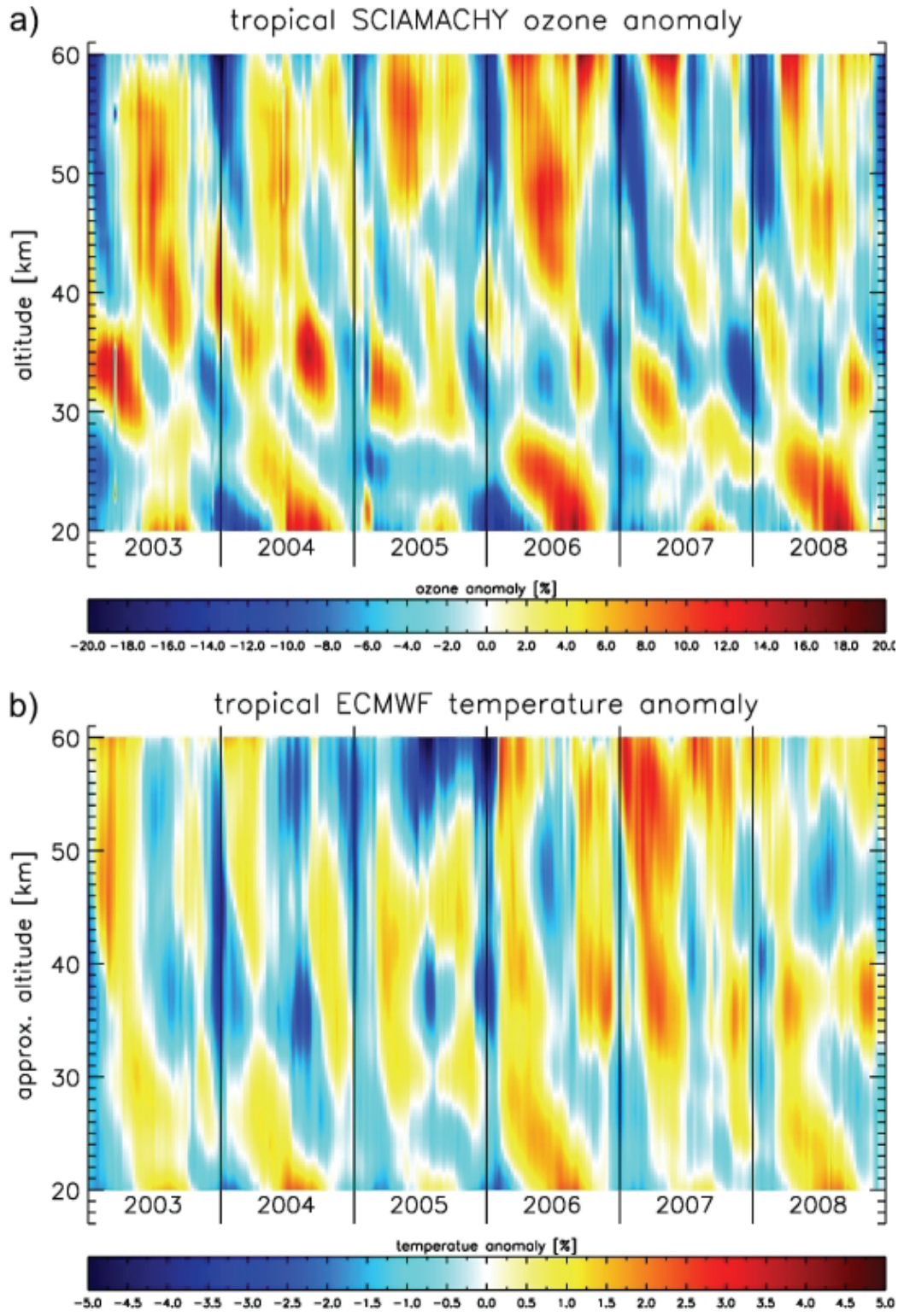

Figure 6.3: Zonal mean anomaly of a) SCIAMACHY ozone and b) ECMWF temperature (20°S-20°N) between 20 and 60 km altitude from 2003 to 2008.

6.4.2 Fast-Fourier transform

A FFT was applied to the unfiltered SCIAMACHY ozone and ECMWF temperature anomalies. The resulting power spectrum can be seen in Fig. 6.4. Similar results are obtained if the semi-annual, annual, and QBO terms from a multivariate least squares approach are subtracted from the time series before FFT application. For ozone, a peak at 26 and 28 days at altitudes of approximately 35 km and above 45 km are visible. In addition, the first harmonics, the 13.5 days signal, is visible at approximately 35 km. Whether or not any high-pass filter or the 6-day smoothing (low-pass filter) was applied to the time series before does not change the result of the FFT. It can also be seen in Fig. 6.4 that the 27-day ozone signal is in fact a collection of periods ranging from 25 to 32 days for the 2003 to 2008 ozone data. As for temperature, peaks are visible at 29 days at altitudes of approximately 35 and 50 km, and also a peak at 23 days at an altitude of approximately 45 km. The overall magnitude of the temperature signal is by more than one order of magnitude less than compared to the ozone signal, which is due to the smaller amplitude of temperature variations.

6.4.3 Cross-correlation

For comparisons to studies by Hood (1986), Fleming et al. (1995) and Hood and Zhou (1998) a CC analysis was performed on SCIAMACHY ozone and ECMWF temperatures. A 35-day running mean was subtracted from the unfiltered time series to remove variations on large time scales, e.g., the (semi-)annual and the QBO signal. An example of the 35-day filtered final time series is shown in Fig. 6.5, where a periodic signal with a period of approximately a month is detectable for ozone and temperature at 45 km altitude.

Mg II index and ozone anomaly time series from SCIAMACHY at selected altitudes are shown in Fig. 6.6. It is evident that both time series track each other nicely for some brief periods, at other times however the correlation vanishes as highlighted in Fig. 6.7. The correlation strongly depends on the examined period.

CCs with time lags between ozone (upper panel) and temperature (lower panel), respectively, and the Mg II index as a function of altitude are shown in Fig. 6.8

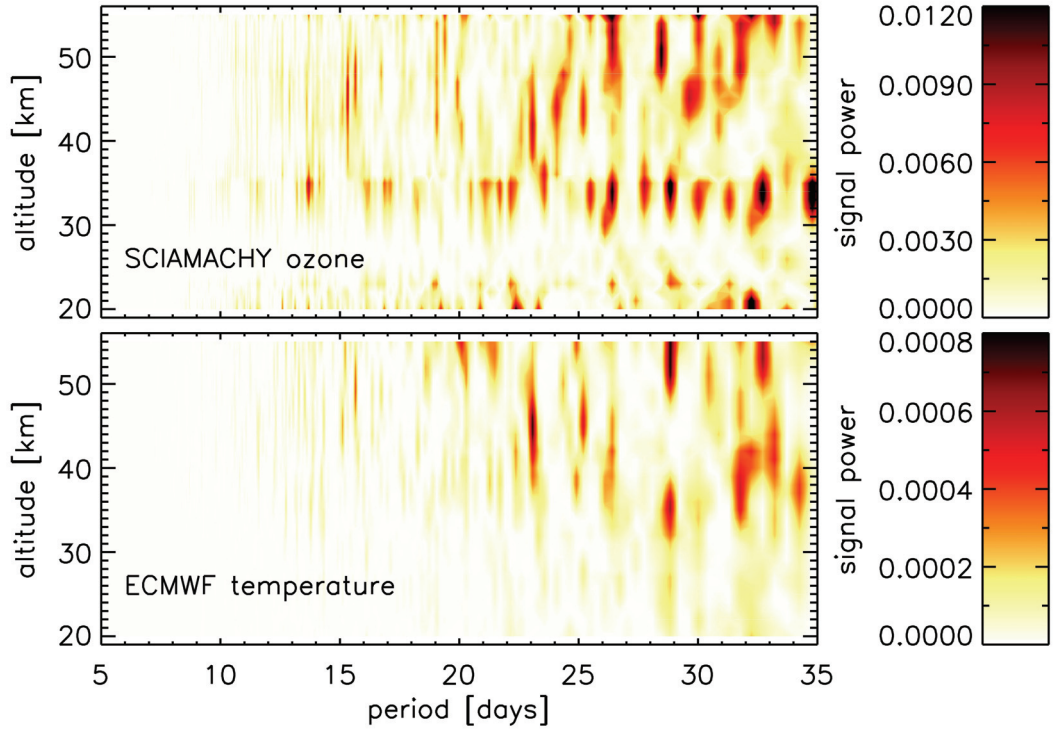

Figure 6.4: FFT power spectrum of zonal mean SCIAMACHY ozone (top) and ECMWF temperature (bottom) anomalies (20°S-20°N) from 2003 to 2008 between 20 and 55 km.

for different time segments: a) the entire observation period (2003 to 2008), b) close to solar maximum (2003 to 2004), c) at solar minimum (2006 to 2007). The 27-day signal is statistically significant near solar maximum and considerably weakens near solar minimum. However, from Fig. 6.7 it is also clear that during some periods close to solar maximum the solar signal in ozone may vanish. Close to solar maximum, the maximum correlation in ozone is 0.38 with a phase lag of approximately 3 days (no phase lag below 35 km). The overall structure of the ozone CC is in agreement with Hood (1986) and Hood and Zhou (1998), however the correlation is lower than during maxima of solar cycle 21 (1979 to 1980) and solar cycle 22 (1990 to 1991) as reported by Hood (1986) and Hood and Zhou (1998), and there is a phase shift of the maximum correlation with altitude by about 5 days between 30 and 45 km, which is not visible in the SCIAMACHY analysis. As

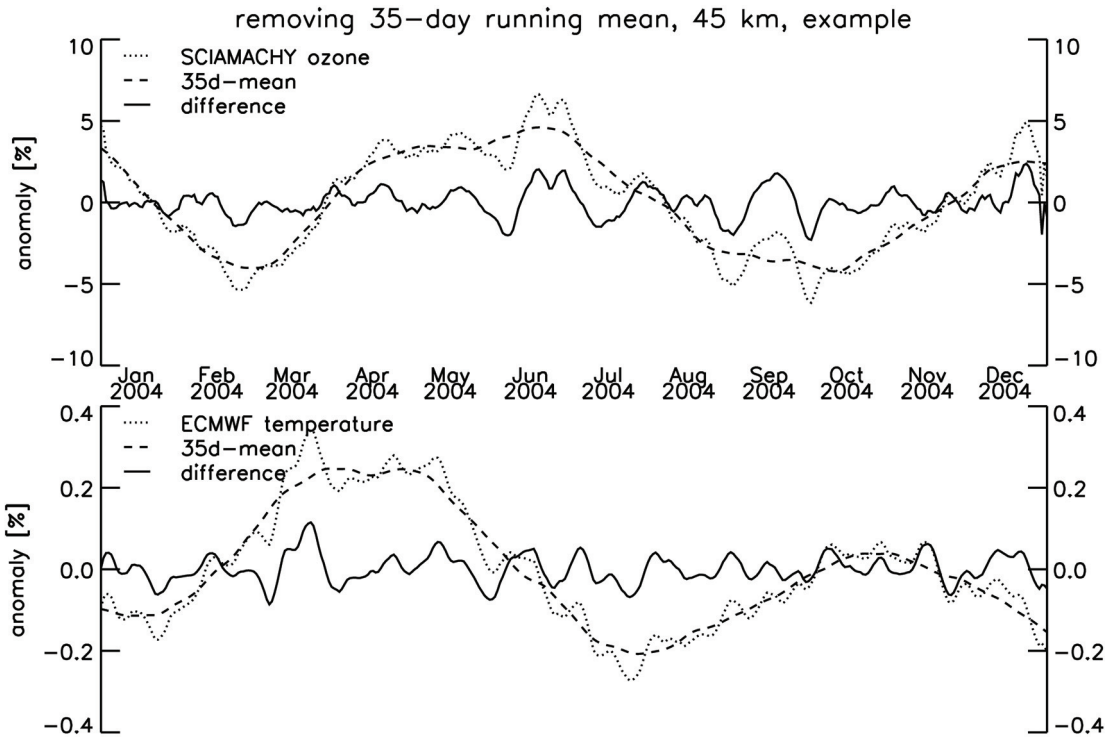

Figure 6.5: Example of SCIAMACHY ozone (top) and ECMWF temperature (bottom) anomaly time series at 45 km altitude in year 2004 before and after subtracting a 35-day running mean.

for temperature, near solar maximum correlations are weak, yet significant, and increasing above 50 km. During solar minimum the correlation weakens and below 30 km an anti-correlation is visible with approximately 2-3 days time lag.

6.4.4 Wavelet analysis

As shown in Fig. 6.7, the correlation between the 27-day solar signal and ozone varies strongly with time. A CWT has the advantage of showing frequencies contained in a time series as a function of time. The Morlet wavelet with an order of 24 was chosen for the transform (Percival and Walden, 2006). This choice provides a good compromise between frequency resolution and time resolution in the power spectrum.

Discontinuities at both ends of the power spectra occur due to the finite nature

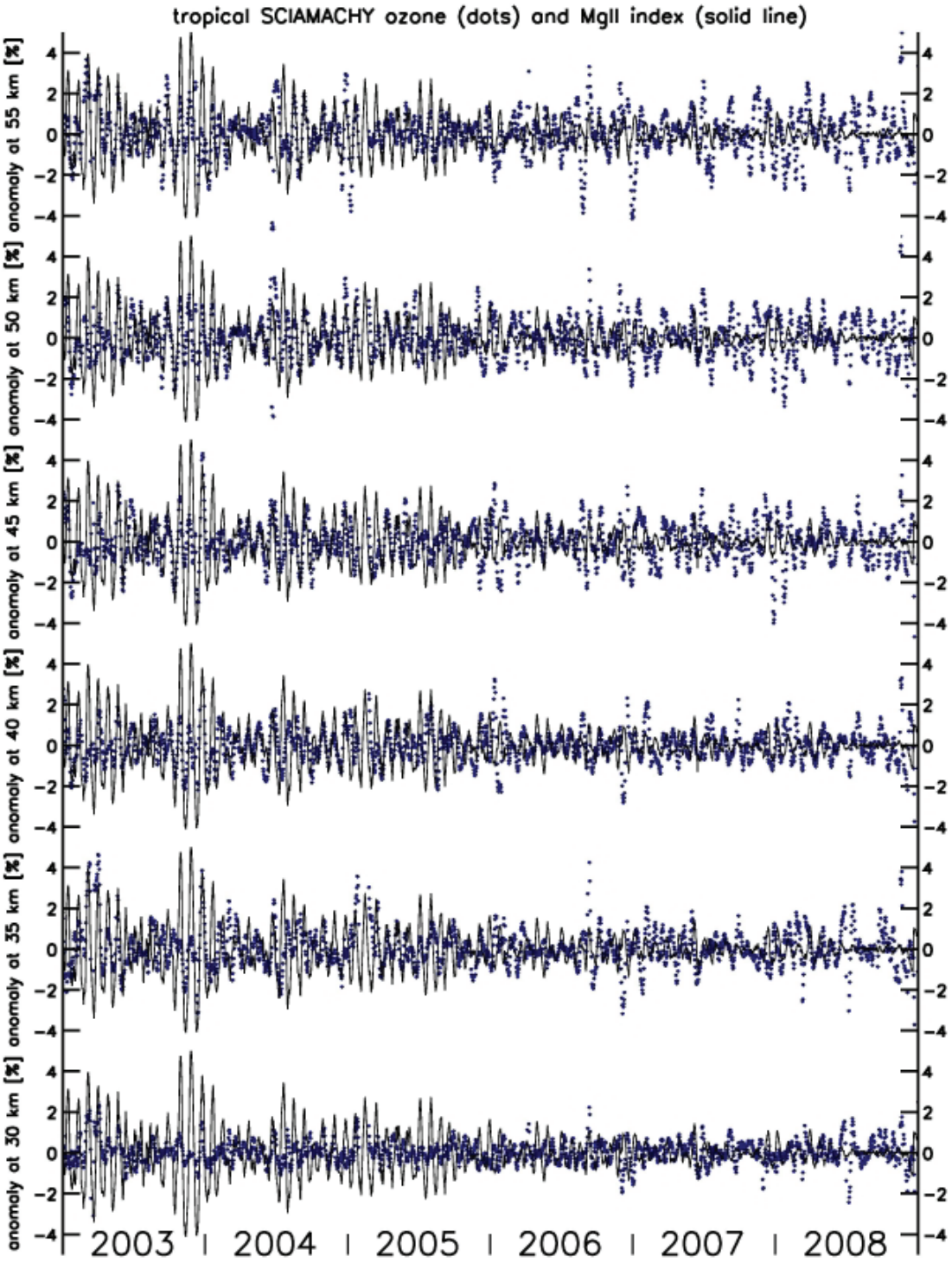

Figure 6.6: SCIAMACHY zonal mean ozone anomaly (20°S-20°N) (solid line) and Mg II index anomaly (filled circles) in percent at selected altitudes (55, 50, 45, 40, 35 and 30 km, from top to bottom). A 35-day running mean was removed in all time series.

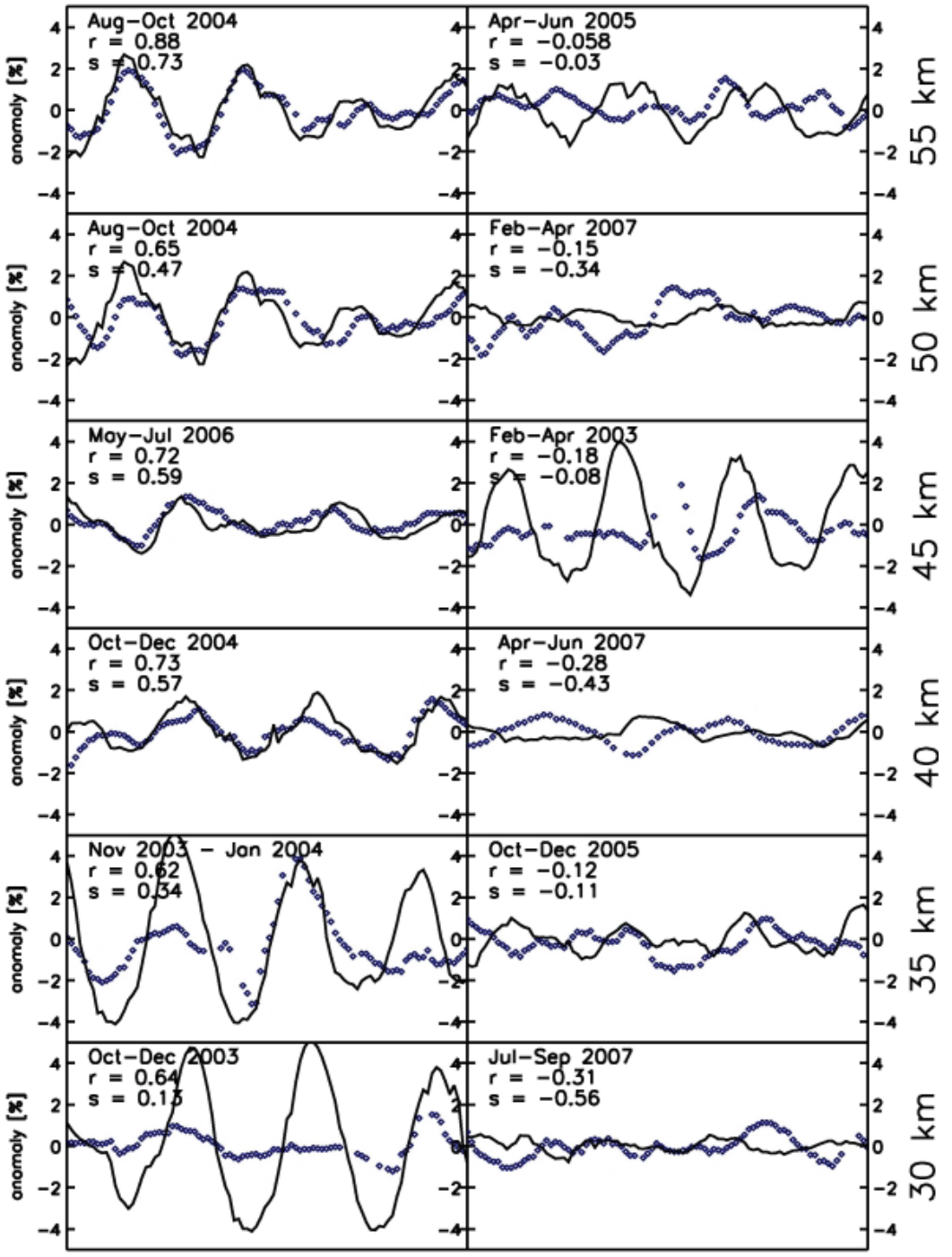

Figure 6.7: Selected three month periods from Fig. 6.6 with high (left panels) and low correlation (right panels) between ozone (solid) and Mg II index (circles). In each panel the period, correlation (r) and ozone sensitivity (s), the latter being defined as ozone change per Mg II index change in units of %/% are indicated. The ozone sensitivity per unit 205 nm solar irradiance change is obtained by multiplying s with 0.61.

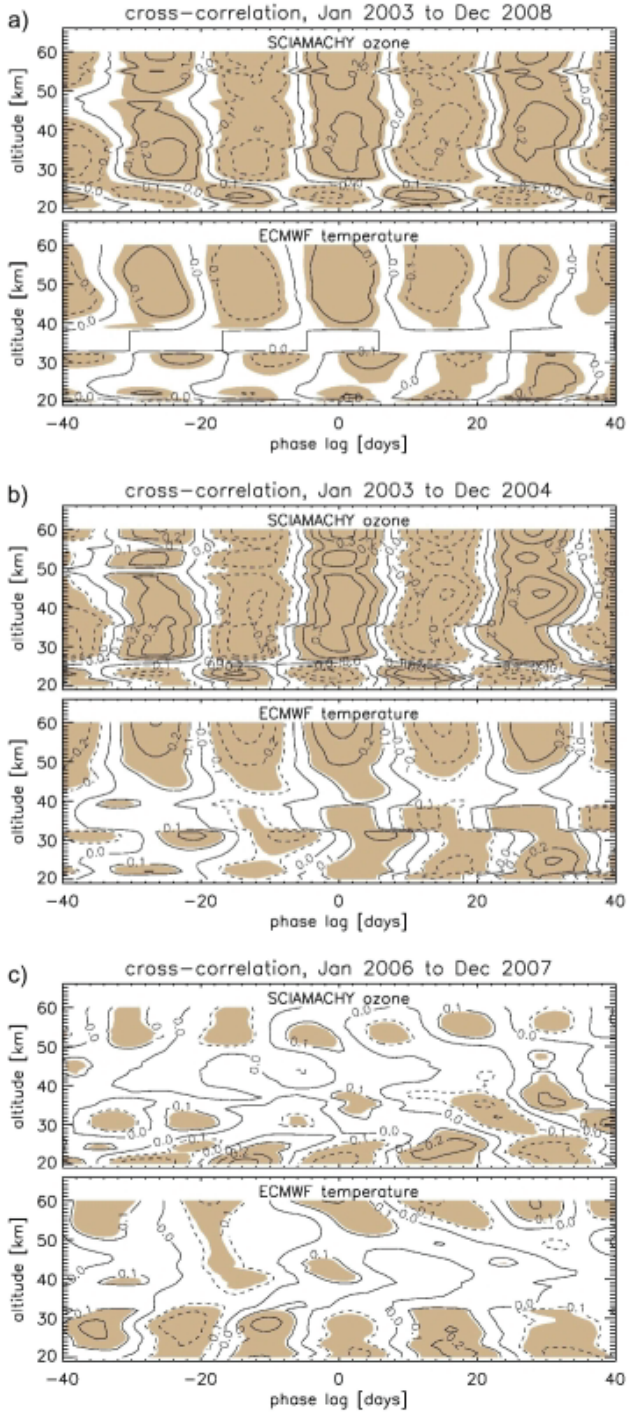

Figure 6.8: a) CC of SCIAMACHY ozone (upper panel) and ECMWF temperature (lower panel), respectively, with Mg II index for the complete observation period (2003-2008). Shaded areas represent regions of statistical significance (2σ). b) Same as a) but under solar maximum condition (2003-2004). c) Same as a) but during solar minimum conditions (2006-2007).

of the time series. The so called *cone of influence* is therefore limited to the inner part of the spectrum bordered by the dashed lines in Figs. 6.9 and 6.10. Solid contour lines denote the 99 % confidence level, which was calculated by testing the wavelet spectra against a theoretical background wavelet spectrum (red or white noise) (Torrence and Compo, 1998). The lower the frequencies the more of the wings of the spectrum can be regarded as statistically insignificant. The Morlet wavelet was also applied to the extended GOMESCIA Mg II index going back to 1979 (Weber, 1999) as shown in Fig. 6.9a. The power spectrum as well as the Mg II index itself clearly shows the increased 27-day amplitude of the Mg II index during solar maximum. The 27-day as well as its first harmonics, the 13.5-day peak, can be identified. Apart from the stronger 27-day signal during solar maximum, it is also evident that solar cycles 21 and 22 were more intense than solar cycle 23 regarding the 27-day signal during solar maximum, especially solar cycle 22 with relative anomaly amplitudes of up to 5 %, which is more than half of the amplitude between solar maximum and solar minimum (11-year cycle). This figure also indicates that the disk averaged solar rotation has varying periods ranging from 25 to 32 days. Ebel et al. (1981) noted 25 day periodic response in temperature and geopotential height at 50, 30 and 10 hPa from solar forcing. The second harmonics, a 9-day signature as identified in the SBUV ozone time series (Fioletov, 2009), is not visible in the CWT of the Mg II index. Only the 27-day signal is above the 99 % level of confidence, which is marked by solid lines.

For a better comparison with SCIAMACHY ozone data, this CWT analysis of the Mg II index has been repeated for the shorter SCIAMACHY observation period from 2003 to 2008 as shown in Fig. 6.9b. This time the 35-day running mean has already been subtracted to remove low frequencies and to treat the Mg II index in the same way as the ozone and temperature data. Again, the 27-day and 13.5-day peaks are clearly visible. The corresponding CWT for ozone and temperature is shown in Fig. 6.10 for altitudes of 30, 45 and 55 km, respectively.

The power spectrum of SCIAMACHY ozone shows a peak at approximately 25 days, but limited to altitudes between 42 and 47 km (cf. Fig. 6.10c for 45 km). This is a slightly higher frequency than the mean solar signal input (27 days). Below this altitude the signal power becomes rather faint lacking a clear peak (Fig.

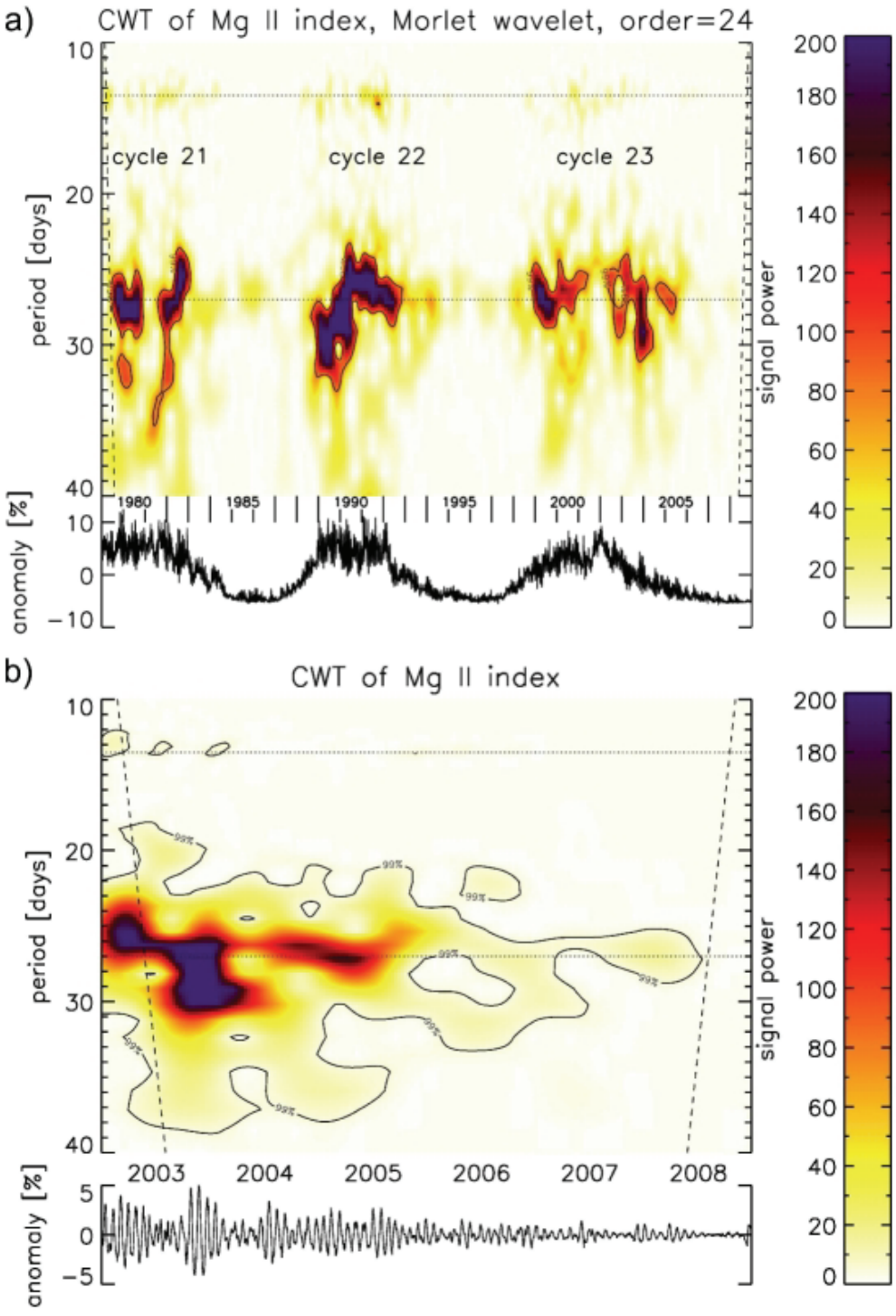

Figure 6.9: a) Wavelet power spectrum as a result of the CWT applied to the composite Mg II index from 1979 to 2008. Peaks around 27 days as well as first harmonics, 13.5 day, are visible. The cone of influence is marked with dashed lines on either side. b) Same as a) but CWT only applied to Mg II data from the SCIAMACHY observation period. Solid contour lines indicate 99 % confidence level.

6.10a). Above 47 km the power spectra show stronger signals, but with broader peaks covering frequencies between 23 and 32 days in selected years (Fig. 6.10e, 2004 and 2006-2007). In the first half of 2005 strong peaks are visible, not only in the ozone time series but also in the power spectrum. Due to a change in SCIAMACHY mission operations tropical ozone data were not available from 29^{th} of January 2005 to 23^{rd} of February 2005 (marked with dashed vertical lines in Fig. 6.10) causing fake signals in the CWT and therefore has to be treated with caution. Especially in Fig. 6.10a, a fake signal is visible in early 2005. Apart from this signal, the CWT of SCIAMACHY ozone at 30 km reveals weak and mostly statistically insignificant signals inside the cone of influence.

The CWT for ECMWF temperatures shows smaller signal strengths compared to ozone, which again is due to its smaller amplitude. Nevertheless, these signals are statistically significant. At 30 km a 30-day peak for early 2008 and a 35-day peak for 2004 are visible. The CWT for 45 km reveals a peak structure going from 23 days up to 35 days from late 2004 to late 2006 similar to ozone. Above that height at 55 km the signals become stronger, with peaks in late 2004 (23-35 days), and in early 2006 (20 days and 28-30 days). Both ozone and temperature CWT show similar time-varying frequency signals in the period range of 25 to 35 days throughout the SCIAMACHY observation period, while CWT of the Mg II index shows marked signals only close to 27 days and during solar maximum. This may suggest that periodic variations in the temperature and ozone in the time scale of 25 to 35 day periods may not only be due to solar variability. An exception is the broad frequency signal in the Mg II CWT at the end of 2003 (25-32 days), which shows a corresponding pattern in ozone only at 45 km altitude, but not in temperature.

6.4.5 Ozone sensitivity to 27-day solar radiation variations

The altitude dependent sensitivity of tropical SCIAMACHY ozone to variations in the 205 nm solar irradiance flux (converted from Mg II index as explained in Sect. 6.3.2) is shown in Fig. 6.11. The solid line indicates the mean sensitivity from the correlation method and dashed lines denote the 2σ uncertainty. The ozone sensitivity is plotted for the complete time series (left panel, 2003-2008), conditions close to solar maximum (middle panel, 2003-2004), and solar minimum

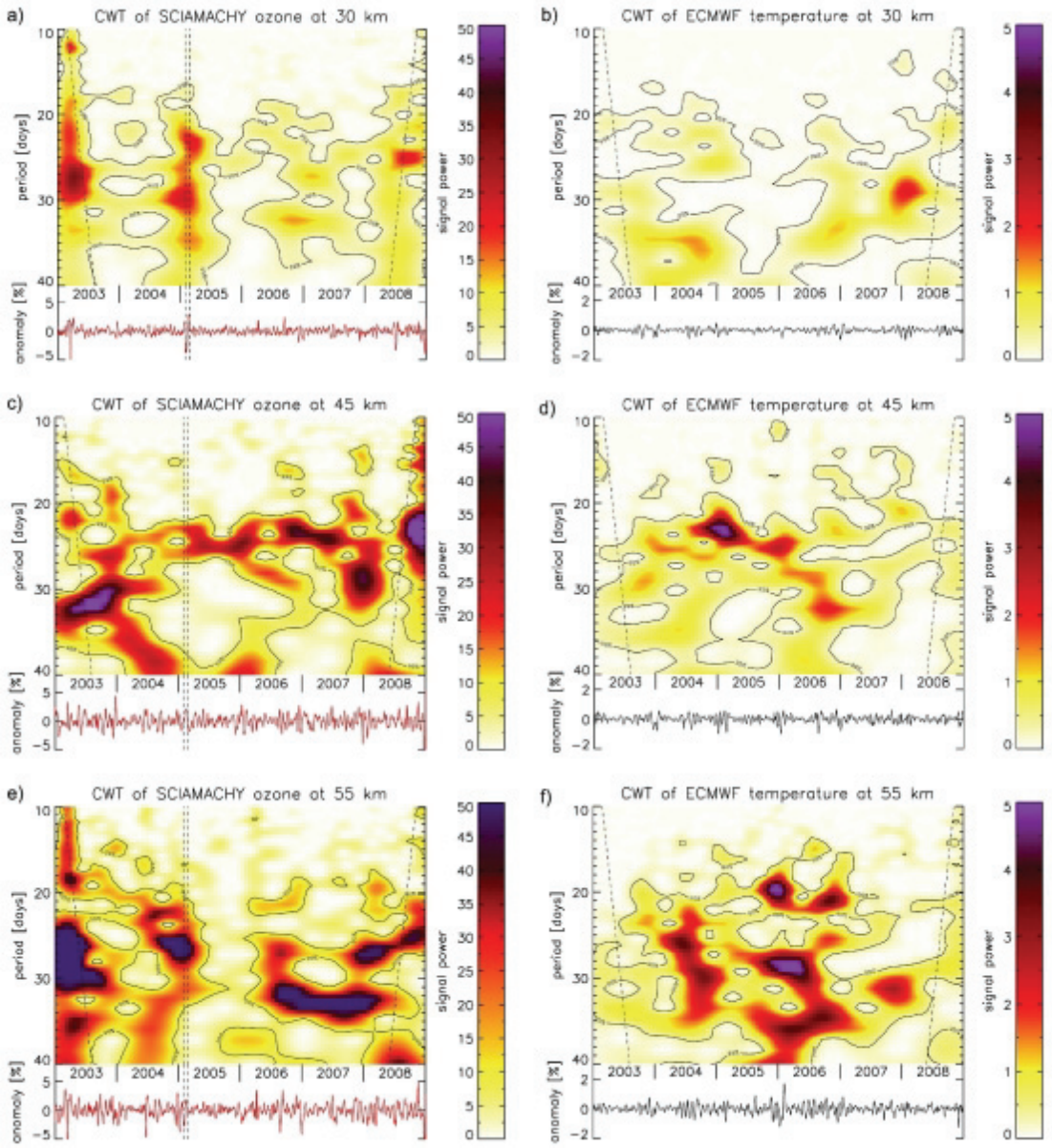

Figure 6.10: Wavelet power spectra as a result of the CWT applied to SCIAMACHY zonal mean ozone anomaly (20°S-20°N) at a) 30 km, c) 45 and e) 55 km altitude and to ECMWF temperature at b) 30 km, d) 45 km, f) 55 km altitudes. The temperature signal is about one order of magnitude weaker. Solid contour lines indicate 99 % confidence level. The vertical dashed lines in a), b) and e) indicate the data gap in early 2005.

(right panel, 2006-2007). Comparisons with model results from Gruzdev et al. (2009, Fig. 10) and observational data results from Fioletov (2009, Fig. 4) show differences in the altitude of maximum sensitivity. Their ozone sensitivity peaks near 40 km for the observations and slightly below for model output, while the peak for SCIAMACHY is at approximately 35 km, and a second but smaller one at 43 km close to solar maximum conditions. The amplitude of the observed ozone sensitivity is a factor of 2-3 smaller than summarized in Gruzdev et al. (2009). From Fig. 6.7 it can be shown that for some three month periods, e.g. August-October 2004, SCIAMACHY ozone sensitivity is in better agreement with Gruzdev et al. (2009) and Fioletov (2009).

6.5 Discussion

The CC between the Mg II index and SCIAMACHY ozone and between Mg II index and ECMWF temperature for heights between 20 km and 60 km are summarized in Fig. 6.8. The results for ozone are similar to the findings from Hood (1986) and Hood and Zhou (1998), however, the absolute value for the maximum correlation is weaker. The maximum correlation in this investigation is 0.25 for the whole SCIAMACHY observation period (2003 to 2008). Close to solar maximum 23 in 2003 to 2004, the maximum correlation increases to 0.38, which is still considerably smaller than the model results from Austin et al. (2007) ($r > 0.8$) for this solar maximum and about 0.5-0.6 from earlier studies (Hood, 1986; Hood and Zhou, 1998). The statistical significance is above the 2σ level as indicated by the gray shading. Limiting data to solar minimum conditions (2006 to 2007) considerably weakens correlations below statistical significance for most altitudes as can be seen in Fig. 6.8c. Hood (1986) chose SBUV data from well within the solar maximum 21 (1979-1980) and also Hood and Zhou (1998) used MLS data from within solar maximum 22 (1990-1991). The first SCIAMACHY data were available from August 2002 onwards, already on the declining branch of solar cycle 23 with smaller amplitudes in the 27-day variations, which is assumed to be the reason for the difference of the presented ozone CC results to previous studies. Comparing the results from the CC to the results from model calculations done by Gruzdev et al.

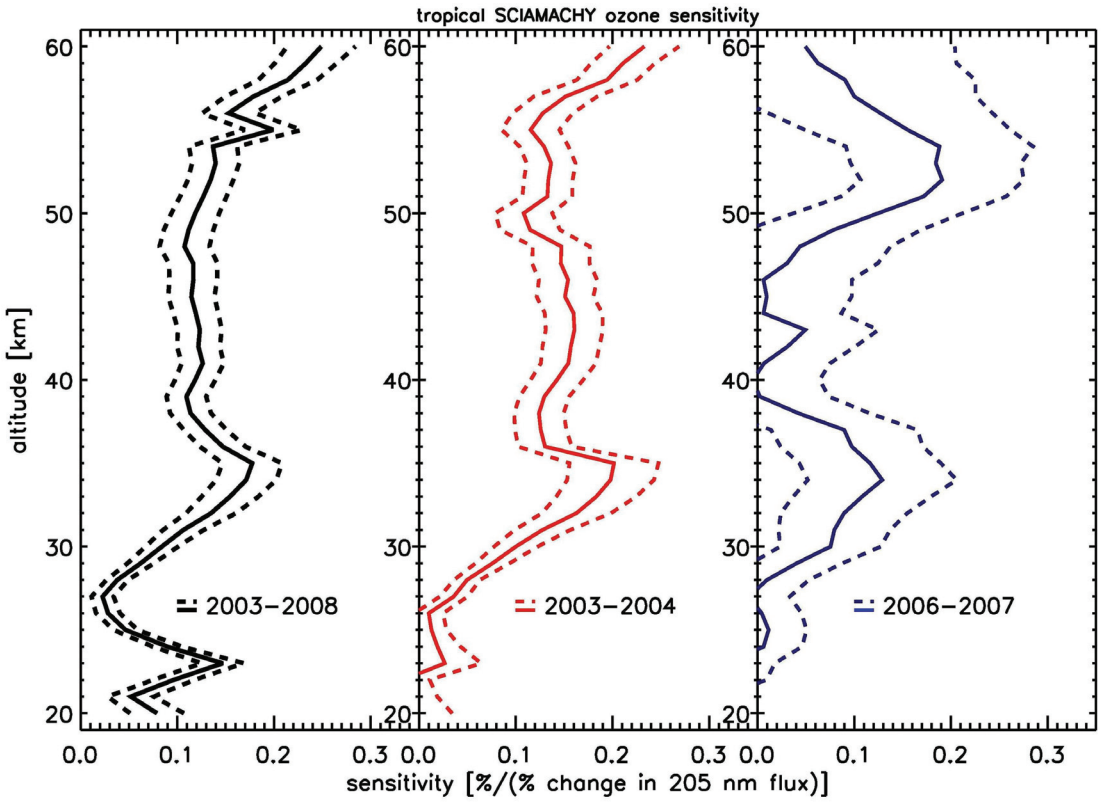

Figure 6.11: Altitude dependent sensitivity of high pass filtered tropical SCIAMACHY ozone (20°S-20°N) to variations in the 205 nm solar irradiance flux in units of %/%. Solid lines indicate the mean and dashed lines denote the 2σ uncertainty. The sensitivity is plotted for the complete time series (left panel, 2003-2008), solar maximum (middle panel, 2003-2004), and solar minimum (right panel, 2006-2007).

(2009, Fig. 2) reveals an agreement between the SCIAMACHY CC under solar maximum conditions and the model CC with solar forcing. However, the varying phase shift with altitude is not visible in the SCIAMACHY CC. The solar forcing in the model being shut off, the CC now rather compares well to the SCIAMACHY CC during solar minimum.

Ruzmaikin et al. (2007) used the Empirical Mode Decomposition (EMD) to investigate the 27-day solar variations in stratospheric ozone and temperature. They came to the same conclusions about the general connection between ozone and temperature (Fig. 6.2). They emphasized that interpreting any obvious correlations

should be done with care since not only ozone but also temperature is dependent on UV changes. In the upper stratosphere the Chapman chemistry governs mainly ozone changes and this is also the region where the highest influence of UV radiation on ozone is found in the presented results. On the other hand, the influence of short-term variation in solar UV radiation on temperature in the upper stratosphere is weaker than it is on ozone (Fig. 6.8). The influence becomes stronger above 50 km and below 30 km. According to Ruzmaikin et al. (2007) the tropical lower stratospheric vertical winds also show a 27-day signal, probably caused by wave disturbances or upwelling. In addition, they identified a 27-day solar UV signature in lower stratospheric tropical MLS (v1.51) temperature data.

The CWT of the Mg II index (Fig. 6.9a) shows that the amplitudes of the 27-day solar forcing are higher during solar maxima of solar cycle 21 and 22 than in solar cycle 23. These results are consistent with findings from Fioletov (2009), who showed in addition that the 27-day solar forcing amplitude is weaker during solar minimum. He separated SBUV ozone data for all solar cycles (21 to 23) into solar maximum and solar minimum conditions (5-year intervals) and found that the ozone response to the 27-day solar forcing is not much different, whether it is solar maximum or minimum, although the 27-day signal in ozone goes below the 2σ level of significance during solar minimum. This result is confirmed with the CWT except that during solar minimum the significance does not even drop below the 3σ level (Fig. 6.10c) and the periods are closer to 25 days. The most interesting result from the CWT analysis of SCIAMACHY ozone is the time varying solar signal, bearing a collection of frequencies close to 27-days, which has been predicted by model simulations by Rozanov et al. (2006) and Gruzdev et al. (2009). The same collection of frequencies is also found in the CWT of ECMWF temperature, partially with the same signals in the CWT as for ozone, implying the connection between ozone and temperature on short-term time scales. However, comparing the CWT power spectra of temperature to the power spectrum of the Mg II index does not reveal many similarities. The CC of temperatures with the Mg II index in the upper stratosphere show weaker correlations than for ozone. The broad frequency response (25-35 days) seen in both ozone and temperature CWTs throughout the SCIAMACHY observation period (Fig. 6.10), but not evident in the Mg II

index strongly suggest that apart from direct radiative effects, indirect effects from chemistry and/or atmospheric dynamics are important. This is in agreement with findings from Brasseur et al. (1987) and Gruzdev et al. (2009). Other dynamical and chemical processes not related to solar activity cannot be ruled out to play a role as well here. A similarity in ozone at 45 km and Mg II frequency response appears to be only evident at the end of 2003 with strong periodic signals in the range of 25 to 32 days. During the Halloween 2003 solar storm unusually large variations in the solar radiation flux were measured by SCIAMACHY (Pagaran et al., 2009).

One has to carefully look at the selected part of the time series that is being investigated. Periodic signals in ozone vary with time and even vanish for several solar rotations independent of the phase of the larger 11-year solar cycle where the period was selected from. This large variability in solar response may be explained by other competing processes like atmospheric transport (dynamics) or chemistry (other than direct photochemistry), which become more important in the lower stratosphere (e.g., Williams et al., 2001). It cannot be ruled out that the latter mechanism may as well be triggered by short-term variations in solar forcing in the upper stratosphere, but are considered indirect effects.

6.6 Summary

In this chapter different approaches were used to analyze the relationship between the 27-day solar variations and stratospheric ozone. In addition, the influence of the 27-day solar variations on ECMWF temperatures were investigated. Some of the techniques were used to prove that SCIAMACHY ozone data are capable of confirming qualitatively results from earlier studies. Correlations are generally higher during solar maximum conditions, but even under solar maximum conditions correlations diminish for several solar rotations as discussed in Sect. 3.3 and 3.4.

A wavelet analysis was used for the first time on satellite observations to investigate sun-ozone interaction and allowed the study of the time varying frequency content of the ozone, temperature, and Mg II index time series. Applied to the ozone time series, only altitudes close to 45 km show a clear 27-day signal. This is

slightly above the height of maximum ozone sensitivity from earlier observations (40 to 45 km, depending on the study) and model runs (approx. 39 km) as summarized by Gruzdev et al. (2009). However, ozone sensitivity to solar flux changes at 205 nm (most important for ozone production) is only half of that from other studies (Gruzdev et al., 2009; Fioletov, 2009). The same techniques as applied to SCIAMACHY ozone were used on the tropical zonal mean ECMWF temperature record between 2003 and 2008. Statistically significant time-varying signals in the power spectra of the temperature CWT were found for periods between 25 and 35 days throughout the SCIAMACHY observation period, and qualitatively agree with the ozone CWT. The CWT of Mg II index shows mostly strong signals very close to 27 days except at the end of 2003, where periodic signals from 25 to 32 days are observed in agreement with ozone (but not temperature) at 45 km altitude. The temperature CC shows weak but significant correlations around zero time lag. This suggests an indirect mechanism or even non-solar related processes to play a more important role on these time scales, in particular for stratospheric temperature.

7 Daytime variations in mesospheric ozone [2]

7.1 Abstract

The scope of this chapter is to investigate the latest version 1.07 SABER tropical ozone from the 1.27 μm as well as from the 9.6 μm retrieval and temperature data with respect to daytime variations in the upper mesosphere. For a better understanding of the processes involved we compare these daytime variations to the output of the three-dimensional general circulation and chemistry model HAMMONIA. The results show good agreement for ozone. The amplitude of daytime variations is in both cases approximately 60 % of the daytime mean. During equinox the daytime maximum ozone abundance is for both, the observations and the model, higher than during solstice, especially above 80 km. We also use the HAMMONIA output of daytime variation patterns of several other different trace gas species, e.g., water vapor and atomic oxygen, to discuss the daytime pattern in ozone. In contrast to ozone, temperature data show little daytime variations between 65 and 90 km and their amplitudes are on the order of less than 1.5 %. In addition, SABER and HAMMONIA temperatures show significant differences above 80 km.

7.2 Introduction

The sun influences the thermal structure, dynamics, and chemistry of the Earth's middle atmosphere. If UV radiation levels alter, middle atmospheric ozone is effected as well as other trace gases formed by photolysis from a direct radiation effect and due to a dynamical response to solar variability (indirect effect). In

[2] Sections 7.1 to 7.7 have been published as Dikty, S., Schmidt, H., Weber, M., von Savigny, C. and Mlynczak, M.: Daytime ozone and temperature variations in the mesosphere: A comparison between SABER observations and HAMMONIA model, Atmos. Chem. Phys. Discuss., 10, 2005-2029, 2010; with minor modifications.

particular, the response of ozone above 60 km to variations in UV radiation is not well established. In comparison with the 27-day solar rotation signal (e.g., Chen et al., 1997; Hood and Zhou, 1998; Ruzmaikin et al., 2007; Gruzdev et al., 2009; Dikty et al., 2009) and the 11-year solar cycle response (e.g., Haigh, 2003; Hood, 2004; Crooks and Gray, 2005; Soukharev and Hood, 2006; Marsh et al., 2007) in the middle atmosphere, the daytime variation of UV radiation inflicts a by far greater response in mesospheric ozone.

In the following it will be refered to *daytime* variations as to (ozone and temperature) variations between sunrise and sunset, i.e. in the tropics between 6h and 18h solar local time. The daytime patterns will be the main focus of this chapter. The term *diurnal* will be reserved for variations on the 24h time scale. The amplitude of daytime ozone variations in the upper mesosphere from sunrise to sunset is about 60 % of the daytime mean with extreme ozone values between 0.1 to 4 ppm at 77.5 km and 1 to more than 10 ppm for altitudes 85 km and above.

An early study by Vaughan (1984) summarizes the basics of mesospheric ozone chemistry. He used ozone data from rocket-borne instrumentation and temperature data from SAMS on Nimbus-7 and compared these with the output of a radiative photochemical model. Other early references to mesospheric ozone chemistry are the papers by Allen et al. (1984a,b), wherein they pointed out the significance of oxygen- and hydrogen-containing species and the temperature profile on the diurnal variability of ozone. Data used in these papers are from ground-based and rocket borne instrumentation at mid-latitudes. Several other studies investigated diurnal ozone variations in the mesosphere, including nighttime, with satellites (Ricaud et al., 1996; Marsh et al., 2002; Huang et al., 2008a; Smith et al., 2008) and ground-based observations (Connor et al., 1994; Haefele et al., 2008). Ricaud et al. (1996) also compared their observations with model results. Ground-based observations done in the Bordeaux area were compared to a one-dimensional photochemical model by Schneider et al. (2005). They clearly saw a diurnal pattern and a SAO signal above 50 km altitude. All of the above mentioned studies show that with nightfall the photodestruction of ozone stops and ozone quickly reaches a high nighttime equilibrium in the mesosphere. The models used by Ricaud et al. (1996) and Sinnhuber et al. (2003) did not show any variations during night, and

observations showed little to no variations.

Marsh et al. (2002) studied diurnal ozone variations from the High Resolution Doppler Imager (HRDI) on board UARS in the altitude range between 70 and 95 km. They attributed the increase in ozone in the afternoon in the upper mesosphere to the migrating diurnal tide. Air that is rich in atomic oxygen is believed to be pumped down from the lower thermosphere and to form ozone on recombination with molecular oxygen. SABER temperature data have been used, e.g., by Zhang et al. (2006) and Mukhtarov et al. (2009) to study tidal signatures between 20 and 120 km altitude within $\pm 50^\circ$ latitude. The solar diurnal tide has also been investigated by Achatz et al. (2008) who utilized a combination of HAMMONIA and a linear model.

Smith et al. (2008) were recently reporting on high ozone values at the nighttime mesopause observed in SABER version 1.07 ozone derived from 9.6 μm radiance. They used a simplified model of the diurnal migrating tide to show that the high night-time ozone values (up to 40 ppm) are a result of an upward motion of air low in atomic hydrogen and atomic oxygen combined with low temperatures, as a result of adiabatic cooling.

The paper by Huang et al. (2008a) can be seen as a precursor to the present study. They reported on SABER version 1.06 diurnal ozone variations (derived from 9.6 μm radiance) over 24 hours with the help of a two-dimensional Fourier least squares analysis. They were able to determine the diurnal variation as a function of latitude (up to 48°), altitude and day of year. The analysis was however limited to at least one year of data.

Beig et al. (2008) gave an overview of the temperature response to solar activity in the mesosphere and lower thermosphere. They assumed that the temperature response to solar activity is mainly due to the vertical distribution of chemically active gases near the mesopause and due to changes in the UV radiation.

In this chapter version 1.07 SABER ozone and temperature vertical profiles from 2003 to 2006 are used to derive daytime variations in the tropical upper mesosphere and to compare them with the output of the HAMMONIA model and to previous studies. In addition, version 1.07 SABER ozone data are compared to the previous version 1.06 data that was used in Huang et al. (2008a), especially since the ozone

retrieval at 1.27 μm was updated with respect to non-LTE processes, and the 9.6 μm ozone retrieval was improved by reducing the physical quenching rates of the ozone vibrational levels by a factor of 3. In addition to Huang et al. (2008a), SABER temperature data is also included in the analysis and the results are discussed with respect to the chemistry responsible for the daytime pattern from HAMMONIA ozone, temperature, and other trace gases. In Sect. 7.3 the data sources are summarized first before the methods used to extract the daytime pattern in ozone and temperature are briefly explained in Sect. 7.4. The presentation of the results (Sect. 7.5) and their discussion in Sect. 7.6 is followed by a summary in Sect. 7.7.

7.3 SABER and HAMMONIA data

7.3.1 SABER satellite data

The TIMED satellite has been launched on July 12^{th}, 2001 (Russel III et al., 1999; Remsberg et al., 2008). It circulates the Earth in a low orbit of 628 km mean altitude with an inclination of 74°. The TIMED satellite is in a non-sun synchronous or drifting orbit with a mean orbital time of 97 minutes. Each day the equator crossing time shifts by approximately 12 minutes. The scanning direction of the SABER instrument is perpendicular to the flight direction of TIMED. Once approximately every 60 days, the TIMED satellite performs a yaw maneuver reversing the scanning direction of SABER by 180°. This measuring geometry limits the latitudinal coverage to 83°S to 52°N and 52°S to 83°N, respectively. Continuous time series for high latitudes are therefore not available. Fig. 7.1 shows the spatial coverage for one day of SABER measurements on March 25^{th}, 2003, pointing south and on May 25^{th}, 2003, pointing north. The overall yield is roughly 40,000 profiles per month as SABER solely performs limb measurements in the infrared.

SABER on board TIMED is an infrared spectrometer measuring limb emission with a spectral range from 1.27 μm to 16.9 μm. The time required to make one *up* or *down* scan of the limb is slightly less than one minute. The instrument scans up to about 400 km in altitude, although the only channel that measures above 180 km tangent height is the NO channel at 5.3 μm. The vertical resolution is approximately 2 km and the instrument has a vertical sampling of 0.4 km.

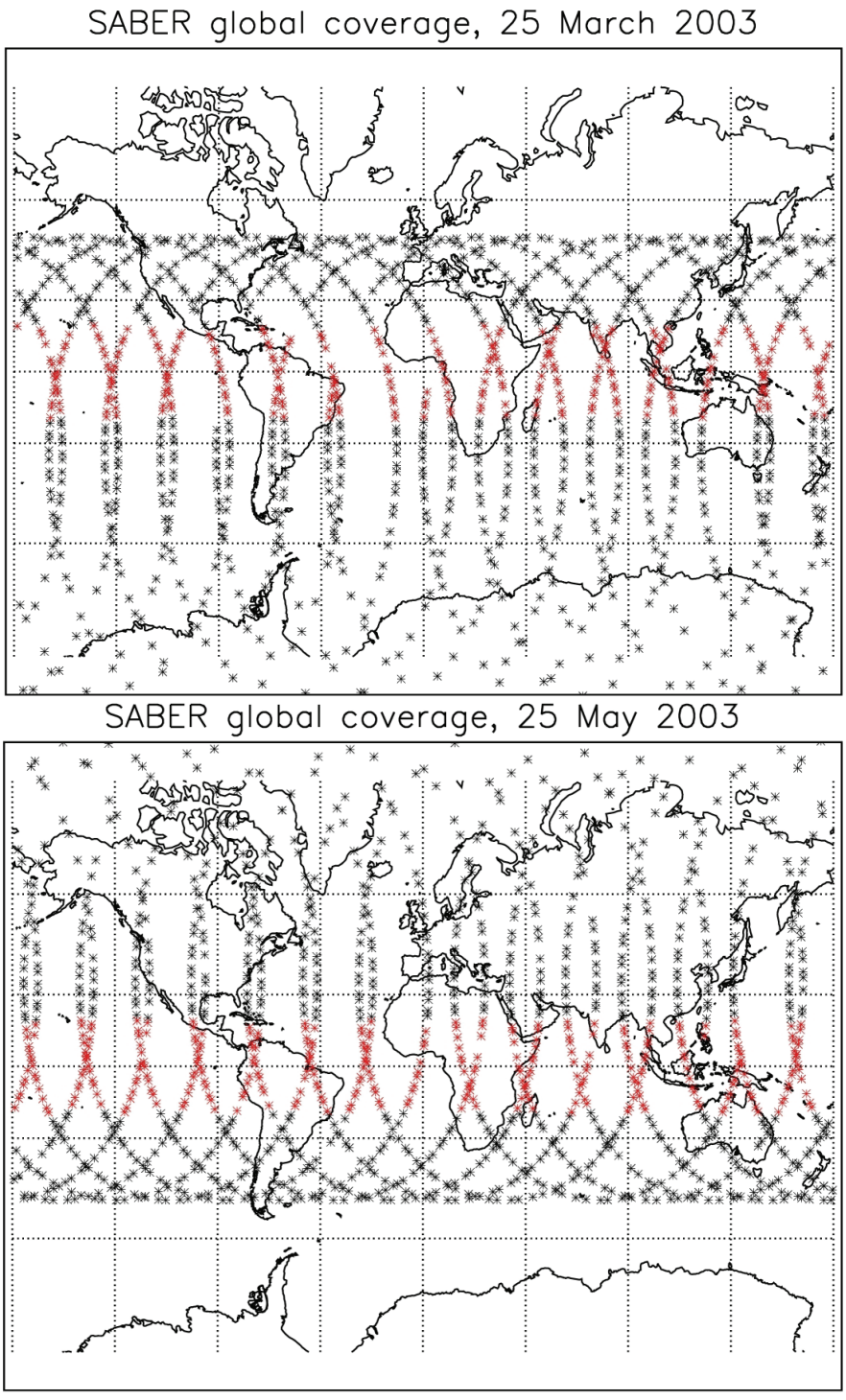

Figure 7.1: Example of daily global coverage of SABER measurements. On March 25 (upper panel), 2003, the instrument was facing south and on May 25 (lower panel), 2003, SABER was facing north. Each asterisk resembles one profile. Profiles between 20°S and 20°N are highlighted in red.

Depending on wavelength (320 nm $< \lambda <$ 1180 nm) the photochemical destruction of ozone can lead to molecular oxygen in its ground state (Eq. 7.1), at wavelengths shortward of 320 nm, and to oxygen in its first exited state (Eq. 7.2). The de-excitation leads to airglow emissions at 1.27 μm (Eq. 7.3) which can be detected by SABER and other spectrometers in orbit, e.g., SCIAMACHY aboard ENVISAT (Bovensmann et al., 1999) and the Optical Spectrograph and InfraRed Imaging System (OSIRIS) on Odin (Llewellyn et al., 2004):

$$O_3 + h\nu(\lambda > 320nm) \rightarrow O_2(^3\Sigma) + O(^3P)\,, \tag{7.1}$$

$$O_3 + h\nu(\lambda < 320nm) \rightarrow O_2(^1\Delta) + O(^1D)\,, \tag{7.2}$$

$$O_2(^1\Delta) \rightarrow O_2(^3\Sigma) + h\nu(1.27\mu m)\,. \tag{7.3}$$

Many parameters related to the odd-oxygen photochemistry and the energy budget of the mesosphere can be derived from these measurements and are used to infer ozone from the 1.27 μm airglow as described in Mlynczak et al. (2007).

In addition to the retrieval of ozone at 1.27 μm that is limited to daytime, the thermal emissions of ozone at 9.6 μm from vibration-rotational energy release can be detected by SABER as described in Rong et al. (2008). The retrieval in the 9.6 μm region permits measurements of ozone not only during daylight but at night as well and the vertical coverage is not limited to the mesosphere and lower thermosphere. Huang et al. (2008a) studied diurnal variations of ozone retrieved at 9.6 μm. Differences to Huang et al. (2008a) will be highlighted throughout this chapter. One of which is the emphasis on the daytime (6h-18h solar local time) ozone pattern, in addition to comparisons to the HAMMONIA model. In this chapter ozone data retrieved at 1.27 μm and at 9.6 μm is used, and temperature data available from SABER is also included. The temperature is retrieved using the spectral information from the two CO_2 channels at 14.9 μm and 15.2 μm (Remsberg et al., 2004).

7.3.2 HAMMONIA model

In this chapter the output from the three-dimensional general circulation and chemistry model HAMMONIA (Schmidt et al., 2006) is used to compare to SABER

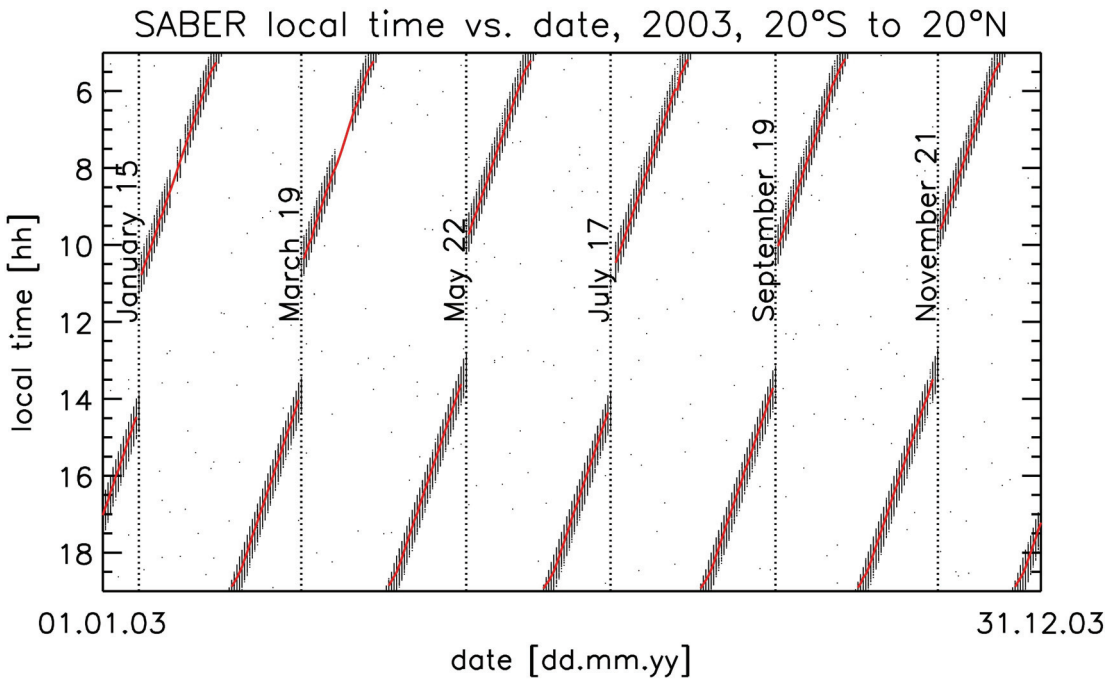

Figure 7.2: Distribution of solar local times of SABER measurements between 20°S and 20°N for the year 2003. Each dot represents one profile. The vertical dotted lines with dates indicated mark yaw maneuvers. The red line shows daily mean of the solar local time of measurements.

observations. HAMMONIA treats atmospheric dynamics, radiation and chemistry interactively. It was developed as an extension of the atmospheric general circulation model MAECHAM5 (Giorgetta et al., 2006; Manzini et al., 2006) and additionally accounts for radiative and dynamical processes in the upper atmosphere. HAMMONIA includes 153 gas phase reactions and 48 chemical compounds. It is a spectral model with (in the current configuration) triangular truncation at wave number 31 (T31) and with 67 levels between the surface and $1.7{\cdot}10^{-7}$ hPa (≈250 km). The model includes a full dynamic and radiative coupling with the MOZART3 chemical module (Kinnison et al., 2007). In addition, it accounts for solar heating in the UV and extreme UV wavelength regime, a non-LTE radiative scheme, energy deposition and eddy diffusion generated by gravity wave breaking, vertical molecular diffusion and conduction, and a simple parameterization of electromagnetic forces in the thermosphere. The processing of the model output is described in Sect. 7.4.

7.4 Data processing

7.4.1 SABER ozone and temperature data processing

The SABER ozone profiles retrieved from the 1.27 μm and 9.6 μm radiometer measurements as well as temperature profiles were interpolated to a regular height grid of 0.5 km using spline interpolation. All profiles were also gridded in the same fashion to a logarithmic pressure scale with an approximate height step of 1 km. Up to 200 profiles per day from within 20°S to 20°N were available for the calculation of an area weighted zonal mean profile. Days with less than 10 profiles were treated as days with no data. At each pressure level outliers in the time series were identified as being outside the 3σ value of the whole time series. Small data gaps of a few days were closed by the use of a spline interpolation. Fortunately, there were no large data gaps from 2003 to 2006.

All daytime time series have a strong signal with a periodicity of approximately 60 days which corresponds to the drift of measurements with local time and the yaw maneuver TIMED is performing. In the tropics this drift in local time is plotted in Fig. 7.2 for 2003. Yaw maneuvers are indicated as vertical dotted lines. Each dot in the plot represents a single profile and the red solid line indicates the mean local time of measurement. The fairly small spread of about half an hour resembles the uncertainty with which the mean local time is determined. The variability of the solar local time of approximately half an hour on a given day is mainly due to the fact that the solar local time is slightly different at each latitude in the tropics (movement of the satellite). So by reassigning each day's area weighted zonal mean profile to its mean local time of measurement (with an error of approximately 30 minutes around the mean) the analysis of daytime variations becomes possible. The daytime variation is derived from data covering 60 days of measurements between yaw maneuvers. Due to the properties of the TIMED orbit measurements between 11h and 13h solar local time are not possible.

The resulting daytime variation of ozone is shown in Fig. 7.3 at heights of 69.5, 74.5, 79.5, 84, and 88.5 km (dots) in units of volume mixing ratio. The daytime variations of ozone are also shown in Figs. 7.4 and 7.5 (color coding). Here the variation is given as deviation from the daytime (6-18h) mean in % for pressure

levels between 0.1 to 0.001 hPa. SABER temperature anomalies can be seen in Fig. 7.6 (color coding).

7.4.2 HAMMONIA model output processing

The HAMMONIA model output used in this study is a 20 year-average from a time-slice simulation for present day greenhouse gas concentrations and solar minimum conditions as described by Schmidt et al. (2006). The output is available covering all longitudes in 3.75°-steps and all latitudes in 3.75°-steps. There are 67 model levels in HAMMONIA ranging from the surface to $1.7{\cdot}10^{-7}$ hPa (≈250 km). The vertical resolution in the mesosphere is about 3 km. Along longitude circles all solar local times are covered, which makes it possible to derive diurnal and daytime variations. As the 3D model output is available each 3 hours, results presented here for specific local times are calculated as an average of 8 locations spaced by 45 degrees of longitude. All latitude steps between 20°S and 20°N were chosen to derive an area weighted meridional mean profile. Sunrise and sunset were identified by the sharp decrease and increase in ozone at 0.01 hPa, respectively, at the equator and defined as 6h and 18h solar local time, accordingly. HAMMONIA ozone and temperature daytime variations are shown in Figs. 7.4, 7.5 and 7.6 along with SABER ozone and temperature observations. Fig. 7.7 shows model results for atomic hydrogen, water vapor, hydroxyl, nitric oxide, atomic oxygen, and molecular oxygen in terms of a relative deviation from the daytime mean in %.

7.5 Results

As can be seen in Figs. 7.4 and 7.5, SABER and HAMMONIA ozone have distinct and very similar patterns of daytime variation between 0.1 and 0.001 hPa. SABER ozone results are color coded and the HAMMONIA model results are drawn with line contours. While Fig. 7.4 shows the results for ozone retrieved at 9.6 μm, Fig. 7.5 shows the results for ozone retrieved at 1.27 μm. For both retrievals and model output, ozone variation from sunrise to sunset can be up to 60 % from the daytime mean value. Both observation and model have in common that below about 0.01 hPa ozone values peak in the morning and decrease towards the afternoon.

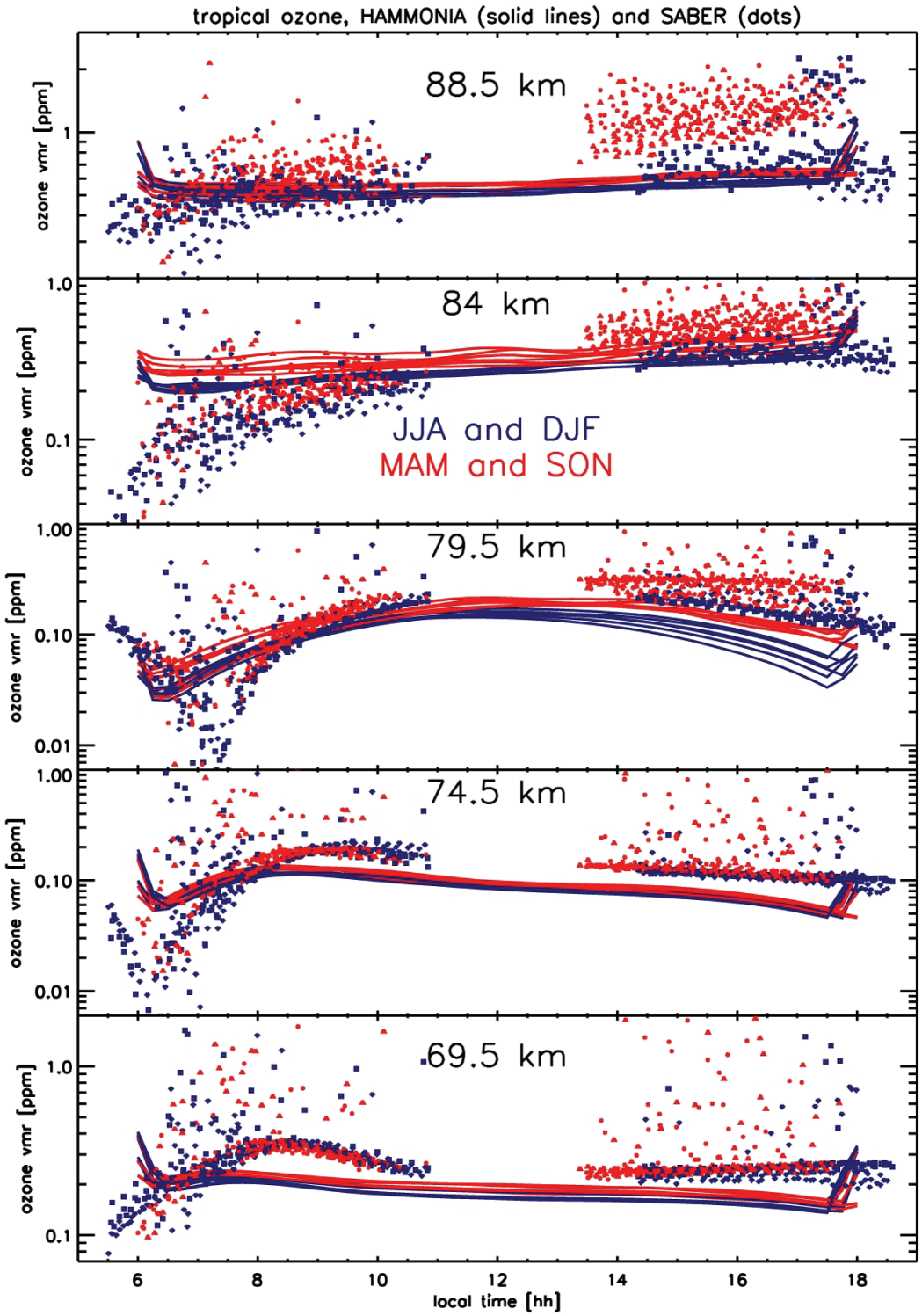

Figure 7.3: SABER (dots) and HAMMONIA (solid lines) daytime ozone (1.27 μm retrieval) variations at 69.5 km, 74.5 km, 79.5 km, 84 km, and 88.5 km sorted by month. Months close to equinox are highlighted in red and months close to solstice are marked in blue.

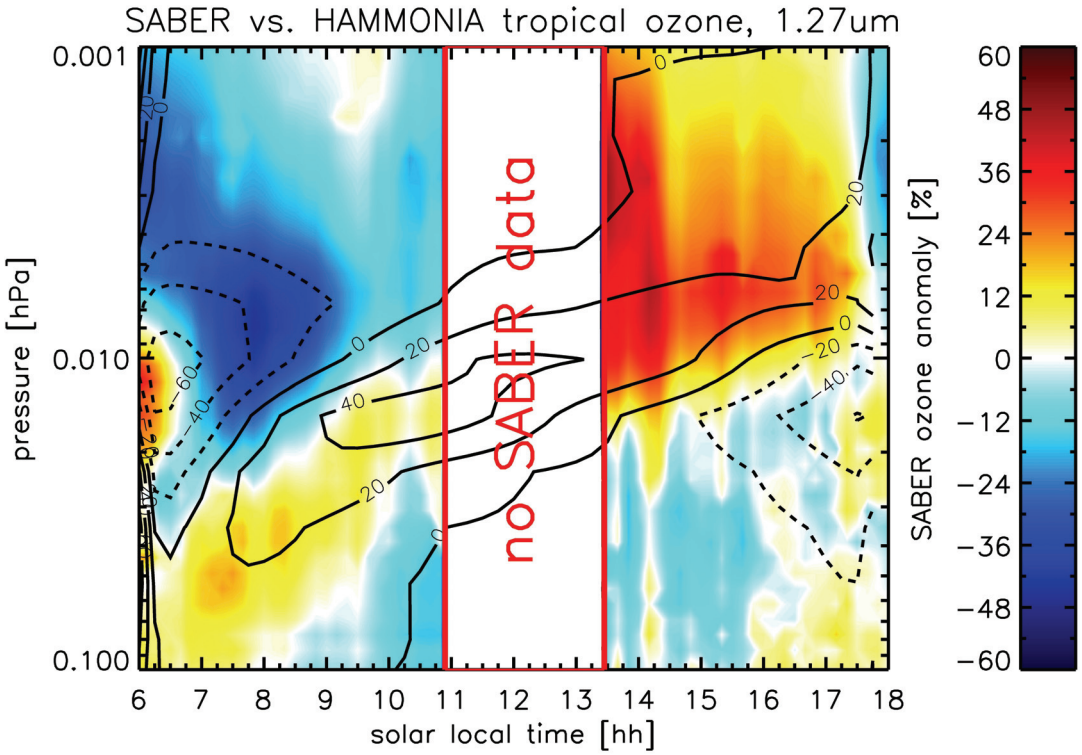

Figure 7.4: SABER (retrieved at 9.6 μm, color coding) and HAMMONIA (contour lines) daytime ozone variations between 0.1 and 0.001 hPa.

This peak shifts towards the afternoon with increasing altitude.

SABER and HAMMONIA ozone show good agreement in the daytime pattern as shown in Figs. 7.4, 7.5 and 7.8. The maximum daytime peak anomaly observed at 0.05 hPa (≈70 km) in the morning shifts its altitude to about 0.007 hPa (≈80 km) in the afternoon. This daytime shift is in very good agreement with the model, however the peak anomaly reaches a maximum of 40-50 % of the daytime mean, which is higher than HAMMONIA (30-40 %). Negative anomalies are observed in the early morning hours at 0.007 hPa and in the late afternoon near 0.015 hPa in quite good agreement with the model (Fig. 7.4). In contrast the 1.27 μm retrieval (Fig. 7.5) does not show this negative anomaly, which could be a SABER retrieval artifact due to twilight conditions. The positive anomaly in the morning hours is also much weaker for the 1.27 μm retrieval (≈10 %) than for the 9.6 μm (≈40 %). Generally the agreement with the model is better for the thermal infrared retrieval.

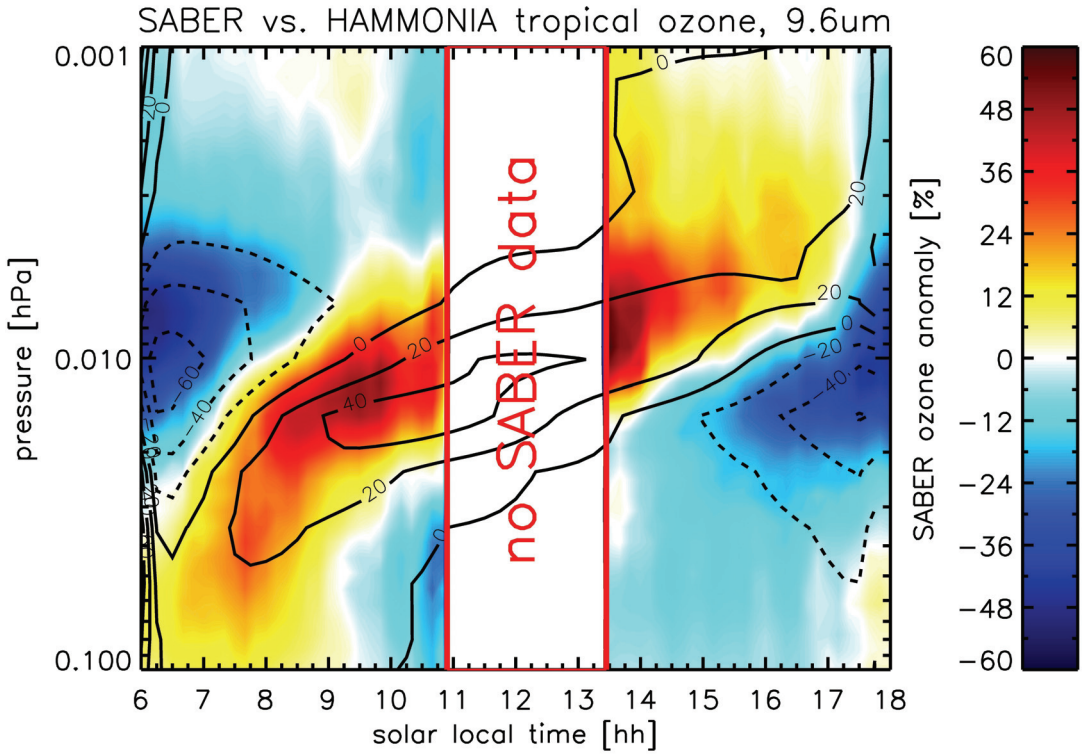

Figure 7.5: Same as Figure 7.4, but for SABER 1.27 μm retrieval.

In the case of temperature, the daytime behavior of SABER and HAMMONIA is out of phase for pressure levels above 0.01 hPa (Fig. 7.6). SABER observes low temperatures in the morning and high values in the afternoon, whereas HAMMONIA predicts high values in the morning and low temperatures in the afternoon. Below 0.01 hPa the agreement is better, yet HAMMONIA does not predict the spurious peak just before the SABER data gap at noon. This might be an artifact in the observations due to averaging effects close to the data gap around noon.

The daytime ozone variations depend on the season as is shown in Fig. 7.3. Especially in the afternoon and above 80 km, ozone reaches up to about 1 ppm in March, April, and May and again in September, October, and November, close to the equinox with increased solar input into the mesosphere. A similar seasonal dependence (albeit with weaker amplitude at high altitudes) is also produced by the HAMMONIA model. Another point is that the ozone minima in the morning do not occur at the same time at 79.5 and 74.5 km. SABER observes the minimum

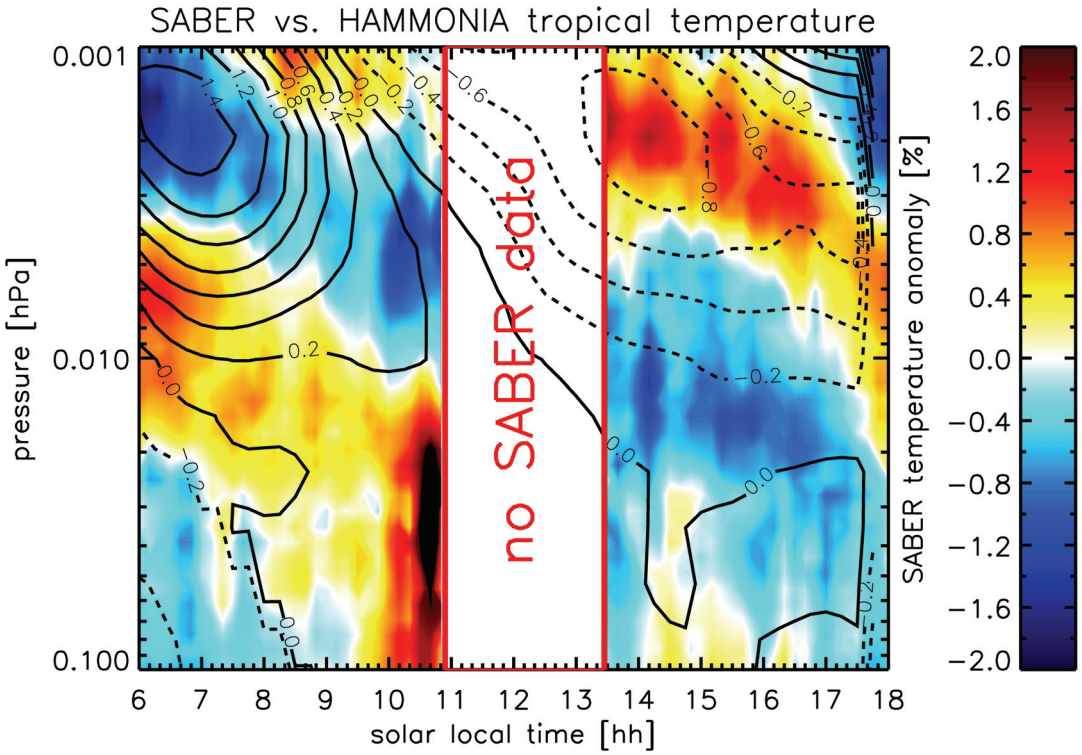

Figure 7.6: SABER (color coding) and HAMMONIA (contour lines) daytime temperature variations between 0.1 and 0.001 hPa.

approximately 30-60 minutes later than HAMMONIA.

7.6 Discussion

As for the version 1.06 SABER ozone data retrieved at 9.6 μm, Huang et al. (2008a) reported on diurnal patterns, including day and night time ozone values. Their method to obtain the diurnal pattern is to perform a least squares estimate of a two-dimensional Fourier series with at least one year of data. With the coefficients from the least squares fit the diurnal variations can be calculated. So, the method is different but the daytime patterns of Huang et al. (2008a) and ours are qualitatively in agreement. The main distinction of the presented method is the focus on daytime rather than diurnal variations, whereas Huang et al. (2008a) concentrated on the ozone shifts at daybreak and nightfall.

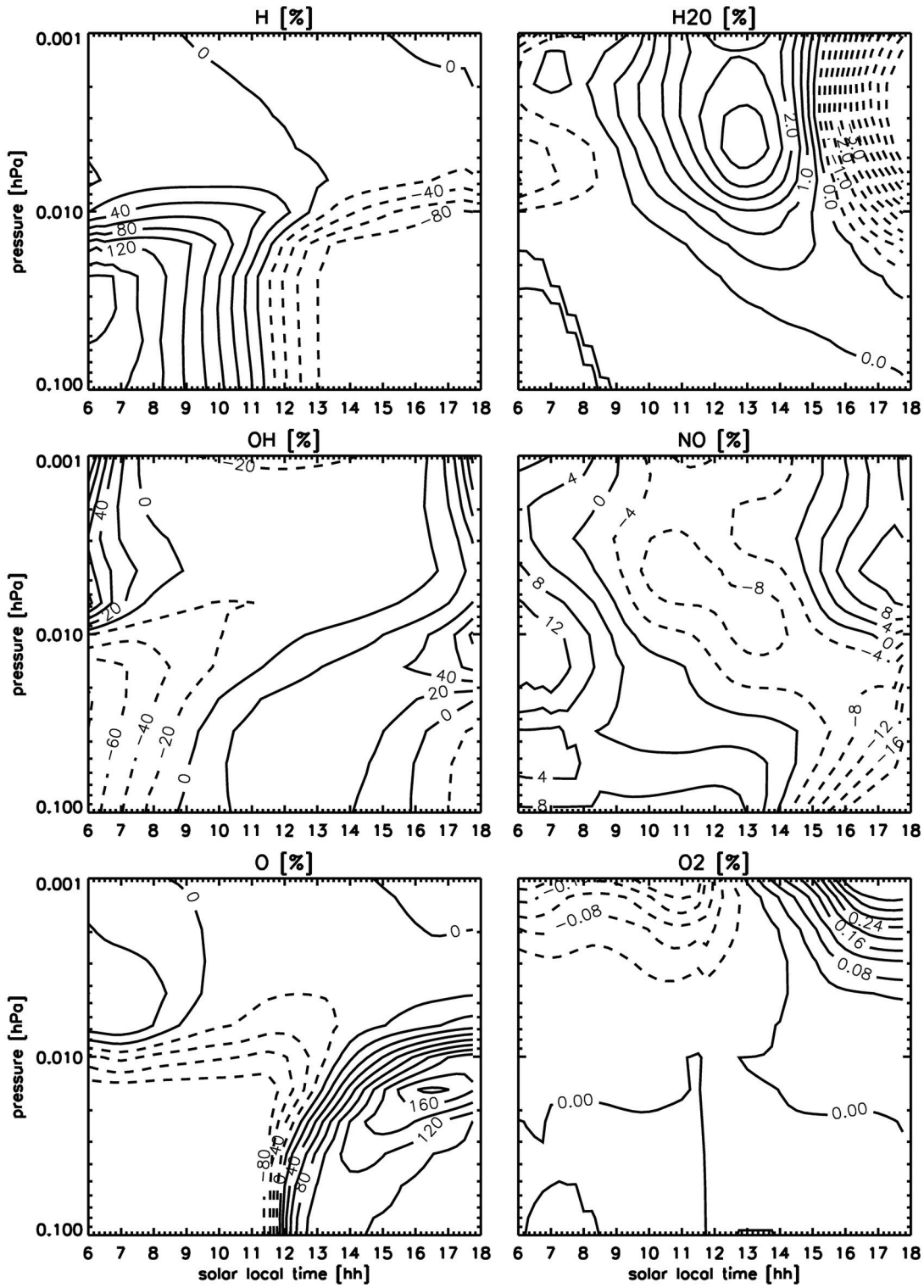

Figure 7.7: HAMMONIA daytime variations of atomic hydrogen, water vapor (top row, left to right), hydroxyl, nitric oxide (middle row, left to right), atomic oxygen, and oxygen (bottom row, left to right) between 0.1 and 0.001 hPa, given as deviation from the daytime mean in %.

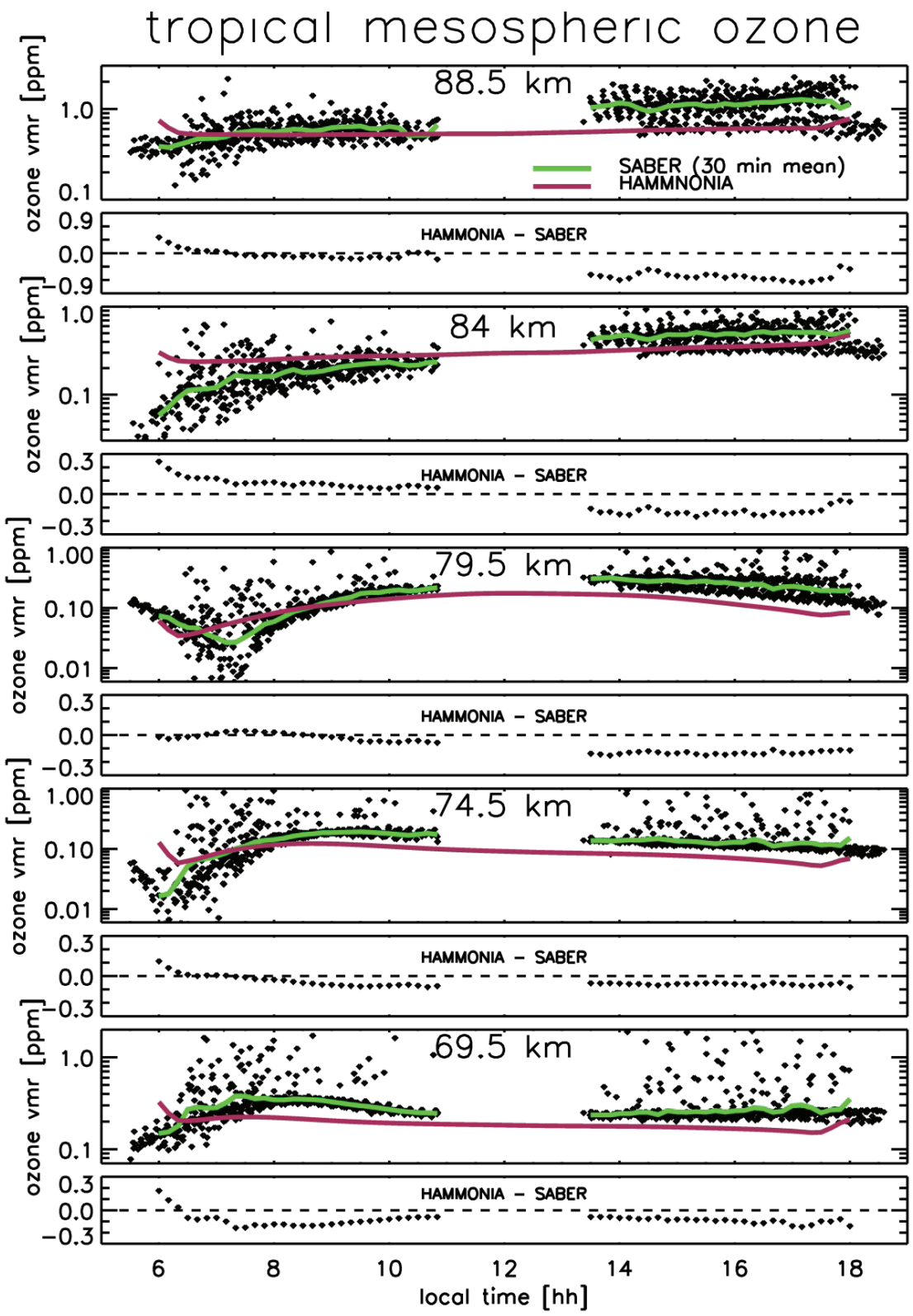

Figure 7.8: Daytime ozone (1.27 μm retrieval) variations as seen by SABER (dots) and HAMMONIA (red solid line) at 69.5 km, 74.5 km, 79.5 km, 84 km, and 88.5 km. A 30 minute running mean was calculated for SABER ozone (green solid line) and the difference to HAMMONIA was plotted below each plot.

The seasonal variation in ozone that can be seen in Fig. 7.3 is likely due to the variation of the angle of the incident light. At equinox the sun has the shortest path through the atmosphere in the tropics and thus the strongest potential to photo-dissociate molecular oxygen. At solstice these light paths are slightly longer in the tropics. Huang et al. (2008b) saw large amplitudes in the temperature semi-annual oscillation (SAO) at 75 and again at 85 km with a distinct minimum in between, and small SAO amplitudes below 80 km, above rising to peak at 95 km. So, a temperature dependency of the ozone SAO in the lower thermosphere cannot be ruled out.

The good agreement between the SABER and HAMMONIA daytime ozone pattern has been shown. In the following, this pattern is discussed with the help of other simulated species (e.g., H, O and OH). Ricaud et al. (1996) explain rising ozone values below 0.01 hPa in the morning with the increased photo-dissociation of O_2 and consequently with a higher production of O_3 due to the high abundance of O radicals. Figure 7.7 shows the daytime pattern of O radicals between 0.1 and 0.001 hPa (i.e., 65 to 95 km) as seen by HAMMONIA. The amplitude rises as high as 160 % from the daytime mean in the afternoon slightly below 0.01 hPa, where HAMMONIA ozone reaches its minimum. The decrease of ozone towards the afternoon below approximately 0.01 hPa is assumed by Ricaud et al. (1996) to have its origin in the HO_x catalytic cycles and the net destruction of ozone. HAMMONIA results of the daytime pattern show increasing values of OH and decreasing levels of atomic hydrogen below 0.01 hPa towards the afternoon (Fig. 7.7). Above 0.01 hPa other mechanisms must be of importance because the O and H radical abundances show almost no daytime pattern. Although daytime patterns can be seen in H_2O and O_2, the amplitude is rather small compared to O, OH and H. Also compared to O, H and OH, NO is the only shown species with strong daytime variations that does not have different amplitudes below and above 0.01 hPa, which indicates that for the mechanisms involved no distinction can be made between both altitude regions. According to Marsh et al. (2002), the shift of the ozone maximum towards late afternoon with increasing altitude, is accounted for by the temperature (altitude) dependent production rate of HO_x and the associated ozone loss. Notice that there is a sharp edge towards low values in the observational data below 0.01 hPa ($\approx$80 km)

and some data are scattered to higher volume mixing ratios (Fig. 7.8). This lower boundary may be attributed to an upper limit in H_2O abundances around 75-80 km. An anti-correlation at these heights between O_3 and HO_x has been concluded by Marsh et al. (2003) after having investigated data from the HALOE.

Marsh et al. (2002) suggested that the solar diurnal tide *pumps* down atomic oxygen for the ozone production in the afternoon ($>$ 85 km). It is interesting to note that the daytime variation of ozone is well reproduced by HAMMONIA in contrast to the temperature that is not. This may indicate that chemistry itself may have a larger impact on the abundance of ozone rather than transport effects involving the lower thermosphere. The model, however, underestimates ozone in the afternoon above approximately 0.01 hPa, so the remaining difference could be attributed to solar tides. The minimum early in the morning is caused by the direct photolysis of ozone before enough atomic oxygen is produced to counteract the ozone destruction. It is also assumed by Marsh et al. (2002) that the rise of ozone in the morning hours is due to tides transporting ozone rich air from below. At 0.01 hPa tropical ozone reaches its minimum. At the end of the day ozone rises to its high nighttime equilibrium shortly after sunset, the photochemistry being shut off.

Concerning tides, it is interesting to note that Achatz et al. (2008) have analyzed solar diurnal tides in HAMMONIA and found in general a good agreement with observed tides both in amplitude and in phase. The amplitude of the migrating diurnal tide in the equatorial region was however analyzed to be smaller than inferred from SABER data by Zhang et al. (2006). This supports the conclusion from above concerning the too low afternoon ozone concentrations above 0.01 hPa.

The amplitudes for temperatures from SABER observations and HAMMONIA model are relatively small. They only deviate about 1-1.5 % (i.e. 1.2-2 K) from the mean at maximum. It remains to be explained why model and observations show a different sign in the daytime pattern. Despite the general similarity of tidal patterns in HAMMONIA and observations as stated by Achatz et al. (2008), the comparison of temperature data suggests a difference in the vertical wavelength of tides in HAMMONIA and SABER. However, the exact analysis of the tides in HAMMONIA is not subject of this study.

7.7 Summary

Within this chapter SABER measurements and HAMMONIA model simulations of upper mesospheric daytime ozone and temperature variations in the tropics between 20°S and 20°N have been compared.

HAMMONIA and SABER daytime ozone variations show a qualitatively good agreement, particularly for the 9.6 μm retrieval. As the agreement is worse in the case of temperature, this suggests that the daytime ozone variations are mainly driven by (photo-)chemical processes and less influenced by transport. The underestimation of HAMMONIA ozone above 0.01 hPa in the afternoon may be due to tidal amplitudes being too weak and associated weak downward transport of air rich in atomic oxygen.

Daytime ozone values above 0.01 hPa are higher close to equinox than close to solstice. Volume mixing ratios can even go as high as 1.0-1.5 ppm in the afternoon for heights above 85 km. Upcoming SABER version 1.08 data will also include water vapor, which will be helpful to constrain the HO_x budget and its influence on daytime ozone.

8 Overall summary and outlook

This thesis documents contributions to a better understanding of solar-terrestrial relations, i.e. in particular the influence of solar rotation on stratospheric ozone and the chemistry of daytime variations of mesospheric ozone with respect to oxygen- and hydrogen-containing species. In order to achieve these goals, various data sets from satellite measurements and models were utilized.

New SCIAMACHY ozone data from a combined Hartley/Huggins and Chappuis band retrieval (the retrieval itself not being part of this thesis) covering altitude ranges between 20 and 60 km in combination with frequency analysis tools like the FFT, CC, and CWT were applied to unravel the modulating nature of the solar rotation signal in stratospheric ozone. The FFT of SCIAMACHY tropical ozone showed not only signals at a period of 27-days but also other periods nearby. CCs of ozone versus temperature identify strong correlations ($r > 0.9$) at 20 km with a time lag of 15-30 days, and strong anti-correlations ($r < -0.8$) at about 40 km with no time lag. The deseasonalization of the time series leads to weaker cross-correlations ($r > 0.5$ at 20 km and $r < 0.6$ at 40 km with no time lag). A multivariate least squares approach separates SAO, AO, and QBO signals from the time series and shows amplitudes of more than 5 % for the SAO below 20 km, around 35 km, and above 55 km, up to 10 % for the AO below 20 km and more than 5 % above 50 km, and up to 5 % for the QBO between 25 and 40 km. CCs of ozone versus Mg II index show significant correlations near solar maximum ($r > 0.35$) and insignificant correlations during solar minimum. The CC of ECMWF temperature versus Mg II index is weaker than for ozone, but still statistically significant, and also shows no significant results during solar minimum. The CWT of the combined time series of the Mg II index, deduced from SBUV (1979-1992), SUSIM (1992-1995), GOME (1995-2002), and SCIAMACHY (2002-today) measurements revealed the broad range of periods (25-32 days) from the solar rotation signal especially during solar

maximum. This conglomerate of periods is also visible in CWTs of SCIAMACHY ozone and ECMWF temperatures.

For the investigation of daytime (and diurnal) variations of atmospheric trace gas compositions the observing instrument needs to be in a non-sun synchronous satellite orbit. This way the solar local time of observations shifts from one day to another and allows the retrieval of information at different local times. SABER ozone (1.27 and 9.6 μm retrieval) and temperature data in its latest version 1.07 are available throughout the mesosphere (also in the stratosphere from the 9.6 μm retrieval, but the daytime variations below 50 km are not as strong). To be able to discuss the results, the daytime patterns of ozone and temperature were compared to the output of a sophisticated 3D general circulation and chemistry model, HAMMONIA, operated by the Max-Planck-Institute for Meteorology in Hamburg. The comparison shows very good agreement for ozone. For temperature the comparison is rather poor. In general, the upper mesosphere can be divided into two regimes, above and below 80 km. Below 80 km the photochemistry of oxygen and hydrogen species is most important. Depending on the local time (or angle of incident light), ozone producing or reducing reactions dominate. Above 80 km the solar diurnal tide needs also consideration. Therefore vertical motion delivers reactants for the odd oxygen chemistry, respectively air with different temperatures change the rate constants of the reactions involved.

Future work may comprise of an analysis extension to other stratospheric ozone data sets (e.g., SABER, OMI, GOME-2, ...) besides SCIAMACHY to confirm the findings from the time series analysis of the 27-day solar rotation signal. Especially the CWT offers a versatile tool and allows an in-depth view into data time series for high frequency signals. The CWT may also be applied to SCIAMACHY time series of other atmospheric constituents relevant in the ozone chemistry, e.g. NO_2 or BrO (Rozanov et al., 2005a). In addition, the investigation of SCIAMACHY ozone data can be extended to higher latitudes. It would be particularly interesting to see the 27-day solar rotation signal in upper mesospheric ozone near the polar cusps, where ozone is being depleted via NO_x (due to photodissociation of N_2 and O_2 by solar particles), outside solar proton events. Further investigation is possible with respect to a potential QBO phase dependency of the 27-day solar signal in stratospheric

SCIAMACHY ozone time series. A similar dependency was found for the 11-year solar cycle (Labitzke, 2004; Gabis and Troshichev, 2004).

Concerning the daytime variations in SABER ozone, the same analysis could also be done for stratospheric ozone, where overall amplitudes are by far less. With the availability of H_2O in the upcoming version 1.08 data, open questions on the chemistry may be answered, e.g., is H_2O constrained towards higher values below 80 km and why do model and observations differ for temperature above 80 km? In addition, HALOE and MLS data (on board UARS, non-sun synchronous orbit) offer the possibility of daytime pattern retrievals. The investigation can also be extended to higher latitudes but will not be possible at very high latitudes due to the reversal of the viewing geometry at yaw maneuvers.

Reconstructing the past and predicting the future is the foremost duty of models, yet models need to prove their reliability by properly simulating the current state ot the atmosphere. The solar energy introduced into the atmospheric system is particularly important. Short-term variations in solar forcing lead to significant changes in ozone and other trace gases in the middle atmosphere and need to be appropriately modelled in order to simulate solar variability on different time scales.

List of Figures

List of Tables

List of Acronyms

AIS Atmospheric Infrared Sounder

AMSU-A Advanced Microwave Sounding Unit-A

AO annual oscillation

ASAR Advanced Synthetic Aperture Radar

BD Brewer-Dobson

CAWSES Climate And Weather of the Sun-Earth System

CC cross-correlation

CCM Chemistry-Climate-Model

CFC chlorofluorocarbon

CME coronal mass ejection

CWT continuous wavelet transform

DFG Deutsche Forschungsgemeinschaft

DFT discrete-Fourier transform

DKRZ Deutsches Klimarechenzentrum

DORIS Doppler Orbitography and Radiopositioning Integrated by Satellite

DU Dobson unit

ECMWF European Centre for Medium range Weather Forecast

EMD Empirical Mode Decomposition

ENVISAT ENVIronmental SATellite

ESA European Space Agency

ESTEC European Space research and TEchnology Centre

FFT fast-Fourier transform

GOME Global Ozone Monitoring Experiment

GOMESCIA combined GOME and SCIAMACHY

GOMOS Global Ozone Monitoring by Occultation of Stars

GPS Global Positioning System

GUVI Global UltraViolet Imager

HALOE Halogen Occultation Experiment

HAMMONIA Hamburg Model of the Neutral and Ionized Atmosphere

HIRS High-resolution Infrared Radiation Sounder

HRDI High Resolution Doppler Imager

IFOV instantaneous field of view

IPCC Intergovernmental Panel on Climate Change

LIMS Limb Infrared Monitor of the Stratosphere

LRR Laser RetroReflector

LTE Local Thermodynanic Equilibrium

MERIS Medium Resolution Imaging Spectrometer

MIPAS Michelson Interferometer for Passive Atmospheric Sounding

MLS Microwave Limb Sounder

MOZART3 Model for Ozone and Related Chemical Tracers, version 3

MWR MicroWave Radiometer

NASA National Aeronautics and Space Administration

NIR Near-InfraRed spectrometer

NLC noctilucent cloud

Odin Name of a satellite operated by the Swedish National Space Board

OMI Ozone Monitoring Instrument

OSIRIS Optical Spectrograph and InfraRed Imaging System

PMC polar mesospheric cloud

PSC polar stratospheric cloud

QBO quasi-biennial oscillation

RA-2 Radar Altimeter 2

SABER Sounding of the Atmosphere using Broadband Emission Radiometry

SAGE Stratospheric Aerosol and Gas Experiment

SAMS Stratospheric and Mesospheric Sounder

SAO semi-annual oscillation

SBUV Solar Backscatter UltraViolet

SCIAMACHY SCanning Imaging Absorption spectroMeter for Atmospheric CHartographY

SCIATRAN Name of a radiative transfer model

SCOSTEP Scientific Committee on Solar-Terrestrial Physics

SEE Solar Extreme ultraviolet Experiment

SIM Solar Irradiance Monitor

SPDECDIO Chemical and dynamical influences on decadal ozone change

SPE solar proton event

SOLSTICE SOLar STellar Irradiance Comparison Experiment

SOLOZON Solar irradiance variability on hourly to decadal scale from SCIAMACHY and its impact on middle atmospheric ozone and ozone-climate interaction

SORCE SOlar Radiation and Climate Experiment

SUSIM Solar Ultraviolet Spectral Irradiance Monitor

TIDI TIMED Doppler Interferometer

TIMED Thermosphere, Ionosphere, Mesosphere, Energetics and Dynamics

UARS Upper Atmosphere Research Satellite

UNEP United Nations Environment Program

UV ultraviolet

WMO World Meteorological Organization

XPS XUV Photometer System

Bibliography

Achatz, U., Grieger, N., and Schmidt, H.: Mechanisms controlling the diurnal solar tide: Analysis using a GCM and a linear model, J. Geophys. Res., 113, doi:10.1029/2007JA012967, 2008.

Allen, M., Lunine, J., and Yung, Y.: The Vertical Distribution of Ozone in the Mesosphere and Lower Thermosphere, J. Geophys. Res., 89, 4841–4872, 1984a.

Allen, M., Lunine, J., and Yung, Y.: Correction to 'the Vertical Distribution of Ozone in the Mesosphere and Lower Thermospheret' by M. Allen, J. I. Lunine, and Y. L. Yung, J. Geophys. Res., 89, 11 827–11 827, 1984b.

Austin, J., Hood, L. L., and Soukharev, B. E.: Solar cycle variations of stratospheric ozone and temperature in simulations of a coupled chemistry-climate model, Atmos. Chem. Phys., 7, 1693–1706, 2007.

Banks, P. M., Huntress, W. T., Hudson, R. D., Reber, C. A., Barth, C. A., Farmer, C. B., Geller, M. A., Gille, J. C., London, J., Megill, L. R., Russell III, J. M., Roble, R. G., Stolarski, R. S., and Waters, J. W.: Upper Atmosphere Research Satellite Program, JPL Publications, 78-54, 1978.

Bates, D. R. and Nicolet, M.: The photochemistry of atmospheric water vapor, J. Geophys. Res., 55, 301, 1950.

Beig, G., Scheer, J., Mlynczak, M. G., and Keckhut, P.: Overview of the temperature response in the mesosphere and lower thermosphere to solar activity, Rev. Geophys., 46, doi:10.1029/2007RG000236, 2008.

Bennett, J., Donahue, M., Schneider, N., and Voit, M.: The Essential Cosmic Perspective, Addison-Wesley Educational Publishers, 2008.

Bertaux, J. L., Megie, G., Widemann, T., Chassefiere, E., Pellinen, R., Kyrölä, E., Korpela, S., and Simon, P.: Monitoring of ozone trend by stellar occultations: The GOMOS instrument, Adv. Space Res., 11, 237–242, 1991.

Bovensmann, H., Burrows, J. P., Buchwitz, M., Frerick, J., Noël, S., Rozanov, V. V., Chance, K. V., and Goede, A. P. H.: SCIAMACHY: Mission Objectives and Measurement Modes, J. Atmos. Sci., 56, 127–150, 1999.

Bracewell, R. N.: The Fourier Transform and its Applications, McGraw-Hill Education, 2000.

Brasseur, G.: The response of the middle atmosphere to long-term and short-term solar variability: A two-dimensional model, J. Geophys. Res., 98, 23 079–23 090, 1993.

Brasseur, G., Rudder, A. D., Keating, G. M., and Pitts, M. C.: Response of Middle Atmosphere to Short-Term Solar Ultraviolet Variations: 2. Theory, J. Geophys. Res., 92, 903–914, 1987.

Brewer, A. W.: Evidence for a world circulation provided by the measurements of helium and water vapour distribution in the stratosphere, Q. J. R. Meteorol. Soc., 75, 651–363, 1949.

Burrows, J. P. and Chance, K. V.: SCanning Imaging Absorption spetrometer for Atmospheric CHartographY, Proc. of SPIE, 35, 146–155, 1991.

Burrows, J. P., Schneider, W., Geary, J. C., Chance, K. V., Goede, A. P. H., Aarts, H. J. M., de Vries, J., Smorenburg, C., and Visser, H.: Atmospheric remote sensing with SCIAMACHY, Digest of Topical Meeting on Optical Remote Sensing of the Atmosphere, Optical Society of America, Washington D.C., 4, 71–74, 1990.

Burrows, J. P., Hötzle, E., Goede, A. P. H., Visser, H., and Fricke, W.: SCIAMACHY - Scanning imaging absorption spetrometer for atmospheric chartography, Acta Astronautica, 1490, 445–451, 1995.

Camp, C. D. and Tung, K.-K.: The Influence of the Solar Cycle and QBO on the Late-Winter Stratospheric Polar Vortex, J. Atmos. Sci., 64, 1267–1283, doi:10.1175/JAS3883.1, 2007.

Chandra, S.: Solar-induced oscillations in the stratosphere: A myth or reality?, J. Geophys. Res., 90, 2331–2339, 1985.

Chandra, S., McPeters, R. D., Planet, W., and Nagatani, R. M.: The 27-day solar UV response of stratospheric ozone: Solar cycle 21 versus solar cycle 22, J. Atmos. Terr. Phys., 56, 105–1065, 1994.

Chapman, S.: A theory of the upper atmospheric ozone, Mem. Roy. Meteor. Soc., 3, 130, 1930.

Chen, L., London, J., and Brasseur, G.: Middle atmospheric ozone and temperature responses to solar irradiance variations over 27-day periods, J. Geophys. Res., 102, 29 957–29 979, 1997.

Connor, B. J., Siskind, D. E., Tsou, J. J., Parish, A., and Remsberg, E. E.: Ground-based microwave observations of ozone in the upper stratosphere and mesosphere, J. Geophys. Res., 99, 16 757–16 770, 1994.

Crooks, S. A. and Gray, L. J.: Characterization of the 11-Year Solar Cycle Using a Multiple Regression Analysis of the ERA-40 Dataset, J. Climate, 18, 996–1015, 2005.

Crutzen, P. J.: The influence of nitrogen oxide on the atmospheric ozone content, Q. J. R. Meteorol. Soc., 96, 320–325, 1970.

Crutzen, P. J., Isaksen, I. S. A., and Reid, G. C.: Solar proton events: Stratospheric-sources of nitric oxide, Science, 189, 457–458, 1975.

DeLand, M. T. and Cebula, R. P.: Composite Mg II Solar Activity Index for Solar Cycles 21 and 22, J. Geophys. Res., 98, 12 809–12 823, 1993.

Dikty, S., Weber, M., von Savigny, C., Rozanov, A., Sonkaew, T., and Burrows, J. P.: Modulations of the 27-day solar rotation signal in stratospheric ozone from SCIAMACHY (2003-2008), J. Geophys. Res., paper in press, doi:10.1029/2009JD012379, 2009.

Doornbos, E. and Klinkrad, H.: Modelling of space weather effects on satellite drag, Adv. Space Res., 37, 1229–1239, doi:10.1016/j.asr.2005.04.097, 2006.

Ebel, A., Schwister, B., and Labitzke, K.: Planetary Waves and Solar Activity in the Stratosphere Between 50 and 10 mbar, J. Geophys. Res., 86, 9729–9738, 1981.

Eckman, R. S.: Response of ozone to short-term variations in the solar ultraviolet radiance. 1. A theoretical model, J. Geophys. Res., 91, 6695–6704, 1986a.

Eckman, R. S.: Response of ozone to short-term variations in the solar ultraviolet radiance. 2. Observations and interpretation, J. Geophys. Res., 91, 6705–6721, 1986b.

Etling, D.: Theoretische Meteorologie - Eine Einführung, Springer-Verlag, 2002.

Fahrmeir, L., Künstler, R., Pigeot, I., and Tutz, G.: Statistik, Springer-Verlag, 2004.

Farman, J. C., Gardiner, B. G., and Shanklin, J. D.: Large losses of total ozone in Antarctica reveal seasonal ClO_x/NO_x interaction, Nature, 315, 207–210, 1985.

Fioletov, V. E.: Estimating the 27-day and 11-year solar cycle variations in tropical upper stratospheric ozone, J. Geophys. Res., 114, doi:10.1029/2008JD010499, 2009.

Fischer, H. and Oelhaf, H.: Remote sensing of vertical profiles of atmospheric trace constituents with MIPAS limb-emission spectrometers, Appl. Opt., 35, 2787–2796, 1996.

Fischer, P. and Tung, K. K.: A reexamination of the QBO period modulation by the solar cycle, J. Geophys. Res., 113, doi:10.1029/2007JD008983, 2008.

Fleming, E. L., Chandra, S., Jackman, C. H., Considine, D. B., and Douglass, A. R.: The middle atmospheric response to short and long term solar UV variations: analysis of observations and 2D model results, J. Atmos. Terr. Phys., 57, 333–365, 1995.

Gabis, I. and Troshichev, O.: Influence of solar UV irradiance on quasi-biennial oscillations in the Earth's atmosphere, Adv. Space Res., 34, 355–360, 2004.

Giorgetta, M. A., Manzini, E., Roeckner, E., Esch, M., and Bengtsson, L.: Climatology and Forcing of the QBO in MAECHAM5, J. Climate, 19, 3882–3901, 2006.

Gottwald, M., Bovensmann, H., Lichtenberg, G., Noel, S., von Bargen, A., Slijkhuis, S., Piters, A., Hoogeveen, R., von Savigny, C., Buchwitz, M., Kokhanovsky, A., Richter, A., Rozanov, A., Holzer-Popp, T., Bramstedt, K., Lambert, J.-C., Skupin, J., Wittrock, F., Schrijver, H., and Burrows, J. P.: SCIAMACHY - Monitoring the Changing Earth's Atmosphere, Published by DLR, 2006.

Gruzdev, A. N., Schmidt, H., and Brasseur, G. P.: The effect of the solar rotational irradiance variation on the middle and upper atmosphere calculated by a three-dimensional chemistry-climate model, Atmos. Chem. Phys., 8, 1113–1158, 2009.

Häckel, H.: Meteorologie, Eugen Ulmer, 1999.

Haefele, A., Hocke, K., Kämpfer, N., Keckhut, P., Marchand, M., Bekki, S., Morel, B., Egorova, T., and Rozanov, E.: Diurnal changes in the middle atmospheric H_2O and O_3: Observations in the Alpine region and climate models, J. Geophys. Res., 113, doi:10.1029/2008JD009892, 2008.

Haigh, J. D.: The effects of solar variability on the Earth's climate, Phil. Trans. R. Soc. Lond. A, 361, 95–111, 2003.

Hamill, P., Toon, O. B., and Turco, R. P.: Characteristics of polar stratospheric clouds during the formation of the Antarctic ozone hole, Geophys. Res. Lett., 13, 1288–1291, 1986.

Harder, J., Lawrence, G., Rottman, G., and Woods, T.: The Solar Spectral Irradiance Monitor: SIM, Metrologia, 37, 415–418, 2000.

Hood, L. L.: The temporal behavior of upper stratospheric ozone at low latitudes: evidence from Nimbus 4 BUV data for shortterm responses to solar ultraviolet variability, J. Geophys. Res., 89, 9557–9568, 1984.

Hood, L. L.: Coupled Stratospheric Ozone and Temperature Response to Short-Term Changes in Solar Ultraviolet Flux: An Analysis of Nimbus 7 SBUV and SAMS Data, J. Geophys. Res., 91, 5264–5276, 1986.

Hood, L. L.: Solar ultraviolet radiation induced variations in the stratosphere and mesosphere, J. Geophys. Res., 92, 878–888, 1987.

Hood, L. L.: Effects of solar UV variability on the stratosphere, Solar Variability and Its Effects on Climate, Geophys. Monogr., 141, 283–303, 2004.

Hood, L. L. and Chantrell, V.: Stratospheric ozone and temperature responses to short-term solar ultraviolet radiations: Reproducibility of low-latitude response measurements, Ann. Geophys., 6, 525–530, 1988.

Hood, L. L. and Zhou, S.: Stratospheric effects of 27-day solar ultraviolet variations: An analysis of UARS MLS ozone and temperature data, J. Geophys. Res., 103, 3629–3638, 1998.

Hood, L. L., Huang, Z., and Bougher, S. W.: Mesospheric effects of solar ultraviolet variations: Further analysis of SME IR ozone and Nimbus 7 SAMS temperature data, J. Geophys. Res., 96, 12 989–13 002, 1991.

Huang, F. T., Mayr, H., Russel III, J. M., Mlynczak, M. G., and Reber, C. A.: Ozone diurnal variations and mean profiles in the mesosphere, lower thermosphere, and stratosphere, based on measurements from SABER on TIMED, J. Geophys. Res., 113, doi:10.1029/2007JA012739, 2008a.

Huang, F. T., Mayr, H. G., Reber, C. A., Russel III, J. M., Mlynczak, M. G., and Mengel, J. G.: Ozone quasi-biennial oscillations (QBO), semiannual oscillations (SAO), and correlations with temperature in the mesosphere, lower thermosphere, and stratosphere, based on measurements from SABER on TIMED and MLS on UARS, J. Geophys. Res., 113, doi:10.1029/2007JA012634, 2008b.

Jastrow, R. and Pearse, C.: Atmospheric drag on satellites, J. Geophys. Res., 62, 413–423, 1957.

Johnston, H. S.: Global ozone balance in the neutral stratosphere, Rev. Geophys. Space Phys., 13, 637–649, 1975.

Keating, G. M., Nicholson III, J., Brasseur, G., Rudder, A. D., Schmaltz, U., and Pitts, M.: Detection of stratospheric HNO_3 and NO_2 response to short-term solar ultraviolet variability, Nature, 322, 43–46, 1985.

Keating, G. M., Pitts, M. C., Brasseur, G., and Rudder, A. D.: Response of middle atmosphere to short-term solar ultraviolet variations: 1. Observations, J. Geophys. Res., 92, 889–902, 1987.

Kinnison, D. E., Brasseur, G. P., Walters, S., Garcia, R. R., Marsh, D. R., Sassi, F., Harvey, V. L., Randall, C. E., Emmons, L., Lamarque, J. F., Hess, P., Orlando, J. J., Tie, X. X., Randel, W., Pan, L. L., Gettelman, A., Granier, C., Diehl, T., Niemeier, U., and Simmons, A. J.: Sensitivity of chemical tracers to meteorological parameters in the MOZART-3 chemical transport model, J. Geophys. Res., 112, doi:10.1029/2006JD007879, 2007.

Köppen, W. P., Wegener, A., and Milancović, M.: Die Klimate der geologischen Vorzeit, Gebrüder Borntraeger (Berlin), 1924.

Labitzke, K.: On the signal of the 11-year sunspot cycle in the stratosphere and its modulation by the quasi-biennial oscillation, J. Atmos. Sol.-Terr. Phys., 66, 1151–1157, 2004.

Langematz, U., Grenfell, J. L., Matthes, K., Mieth, P., Kunze, M., Steil, B., and Brühl, C.: Chemical effects in 11-year solar cycle simulations with the Freie Universität Berlin Middle Atmospheric Model with online chemistry (FUB-CMAM-CHEM), Geophys. Res. Lett., 32, doi:10.1029/2005GL022686, 2005.

Le Treut, H., Somerville, R., Cubasch, U., Ding, Y., Mauritzen, C., Mokssit, A., Peterson, T., and Prather, M.: Historical Overview of Climate Change. In: Climate Change 2007: The Physical Science Basis. Contribution of Working Group I to the Fourth Assessment Report of the Intergovernmental Panel on Climate Change [Solomon, S., D. Qin, M. Manning, Z. Chen, M. Marquis, K. B. Averyt, M. Tignor and H. L. Miller (eds.)], Cambridge University Press, Cambridge, United Kingdom and New York, NY, USA, 2007.

Lean, U.: Variations in the Sun's Radiative Output, Rev. Geophys., 29, 505–535, 1991.

Lenoble, J.: Atmospheric radiative transfer, DEEPAK Publishing, 1993.

Liljequist, G. H. and Cehak, K.: Allgemeine Meteorologie, Vieweg, 1984.

Litvinenko, Y. E.: On the Magnetic Field Orientation and Plasma Flows in Solar Filament Barbs, Solar Physics, 196, doi:10.1023/A:1005259508498, 2000.

Llewellyn, E. J., Lloyd, N. D., Degenstein, D. A., Gattinger, R. L., Petelina, S. V., Bourassa, A. E., Wiensz, J. T., Ivanov, E. V., McDade, I. C., Solheim, B. H., McConnell, J. C., Haley, C. S., von Savigny, C., Sioris, C. E., McLinden, C. A., Griffioen, E., Kaminski, J., Evans, W. F. J., Puckrin, E., Strong, K., Wehrle, V., Hum, R. H., Kendall, D. J. W., Matsushita, J., Murtagh, D. P., Brohede, S., Stegman, J., Witt, G., Barnes, G., Payne, W. F., Piché, L., Smith, K., Warshaw, G., Deslauniers, D.-L., Marchand, P., Richardson, E. H., King, R. A., Wevers, I., McCreath, W., Kyrölä, E., Oikarinen, L., Leppelmeier, G. W., Auvinen, H., Mégie, G., Hauchecorne, A., Lefèvre, F., de La Nöe, J., Ricaud, P., Frisk, U., Sjoberg, F., von Schéele, F., and Nordh, L.: The OSIRIS instrument on the Odin spacecraft, Can. J. Phys., 82, doi:10.1139/P04-005, 2004.

Manzini, E., Giorgetta, M. A., Esch, M., Kornblueh, L., and Roeckner, E.: Sensitivity of the Northern Winter Stratosphere to Sea Surface Temperature Variations: Ensemble Simulations with the MAECHAM5 Model, J. Climate, 19, 3863–3881, 2006.

Marsh, D., Smith, A., and Noble, E.: Mesospheric ozone response to changes in water vapor, J. Geophys. Res., 108, doi:10.1029/2002JD002705, 2003.

Marsh, D. R., Skinner, W. R., Marshall, A. R., Hays, P. B., Ortland, D. A., and Yee, J.-H.: High Resolution Doppler Imager observations of ozone in the mesosphere and lower thermosphere, J. Geophys. Res., 107, doi:10.1029/2001JD001505, 2002.

Marsh, D. R., Garcia, R. R., Kinnison, D. E., Boville, B. A., Sassi, F., Solomon, S. C., and Matthes, K.: Modelling the whole atmosphere response to solar cycle changes in radiative and geomagnetic forcing, J. Geophys. Res., 112, doi:10.1029/2006JD008306, 2007.

McCormack, J. P., Siskind, D. E., and Hood, L. L.: Solar-QBO interaction and its impact on stratospheric ozone in a zonally averaged photochemical transport model

of the middle atmosphere, J. Geophys. Res., 112, doi:10.1029/2006JD008369, 2007.

Miranda, H. A. and Fenn, R.: Stratospheric aerosol sizes, Geophys. Res. Lett., 1, 201–203, 1974.

Mitalas, R. and Sills, K. R.: On the photon diffusion time scale for the sun, The Astrophysical Journal, 401, 759–760, 1992.

Mlynczak, M. G.: Energetics of the mesosphere and lower thermosphere and the SABER experiment, Adv. Space Res., 20, 1177–1183, 1997.

Mlynczak, M. G., Marshall, B. T., Martin-Torres, F. J., Russel III, J. M., Thompson, R. E., Remsberg, E. E., and Gordley, L. L.: Sounding of the Atmosphere using Broadband Emission Radiometry observations of daytime mesospheric $O_2(^1\Delta)$ 1.27 μm emission and derivation of ozone, atomic oxygen, and solar and chemical energy deposition rates, J. Geophys. Res., 112, doi:10.1029/2006JD008355, 2007.

Molina, M. J. and Rowland, F. S.: Stratospheric sink for chlorofluoromethanes: chlorine atom catalysed destruction of ozone, Nature, 249, 810–812, 1974.

Mukhtarov, P., Pancheva, D., and Andonov, B.: Global structure and seasonal and interannual variability of the migrating diurnal tide seen in the SABER/TIMED temperatures between 20 and 120 km, J. Geophys. Res., 114, doi:10.1029/2008JA013759, 2009.

Pagaran, J., Weber, M., and Burrows, J. P.: Solar variability from 240 to 1750 nm in terms of faculae brightening and sunspot darkening from SCIAMACHY, Astrophys. J., 700, 1884–1895, 2009.

Percival, D. B. and Walden, A. T.: Wavelet Methods for Time Series Analysis, Cambridge University Press, 2006.

Prölss, G. W.: Physik des erdnahen Weltraums, Springer Verlag, 2001.

Randel, W. J. and Wu, F.: A stratospheric ozone profile data set for 1979-2005: Variability, trends, and comparisons with column ozone data, J. Geophys. Res., 112, doi:10.1029/2006JD007339, 2007.

Remsberg, E. E.: On the response of Halogen Occultation Experiment (HALOE) stratospheric ozone and temperature to the 11-year solar cycle forcing, J. Geophys. Res., 113, doi:10.1029/2008JD010189, 2008.

Remsberg, E. E., Gordley, L. L., Marshall, B. T., Thompson, R. E., Burton, J., Bhatt, P., Harvey, V. L., Lingenfelser, G., and Natarajan, M.: The Nimbus 7 LIMS version 6 radiance conditioning and temperature retrieval methods and results, J. Quant. Spectrosc. Radiat. Transfer, 86, 395–424, doi:10.1029/2006JD007339, 2004.

Remsberg, E. E., Marshall, B. T., Garcia-Comas, M., Krueger, D., Lingenfelser, G. S., Martin-Torres, J., Mlynczak, M. G., Russel III, J. M., Smith, A. K., Zhao, Y., Brown, C., Gordley, L. L., Lopez-Gonzales, M. J., Lopez-Puertas, M., She, C.-Y., Taylor, M. J., and Thompson, R. E.: Assesment of the quality of the version 1.07 temperature-versus-pressure profiles of the middle atmosphere from TIMED/SABER, J. Atmos. Res., 113, doi:10.1029/2008JD010013, 2008.

Ricaud, P., de La Noë, J., Connor, B. J., Froidevaux, L., Waters, J. W., Harwood, R. S., MacKenzie, I. A., and Peckham, G. E.: Diurnal variability of mesospheric ozone as measured by the UARS microwave limb sounder instrument: Theoretical and ground-based validations, J. Geophys. Res., 101, 10 077–10 089, 1996.

Rodgers, C. D.: Inverse Methods for Atmospheric Sounding: Theory and Practice, World Scientific Publishing, 2000.

Roedel, W.: PHYSIK unserer Umwelt - Die Atmosphäre, Springer-Verlag, 2000.

Rohen, G., von Savigny, C., Sinnhuber, M., Llewellyn, E. J., Kaiser, J. W., Jackman, C. H., Kallenrode, M.-B., Schröter, J., Eichmann, K.-U., Bovensmann, H., and Burrows, J. P.: Ozone depletion during the solar proton events of October/November 2003 as seen by SCIAMACHY, J. Geophys. Res., 110, doi:10.1029/2004JA010984, 2005.

Rong, P. P., Russell III, J. M., Mlynczak, M. G., Remsberg, E. E., Marshall, B. T., Gordley, L. L., and Lopez-Puertas, M.: Validation of TIMED/SABER v1.07 ozone at 9.6 μm in the altitude range 15-70 km, J. Geophys. Res., 114, doi:10.1029/2008JD010073, 2008.

Rosenfield, J. E., Douglass, A. R., and Considine, C. B.: The impact of increasing carbon dioxide on ozone recovery, J. Geophys. Res., 107, doi:10.1029/2001JD000824, 2002.

Rottman, G.: Solar UV Irradiance Measurements: the UARS and EOS SOLSTICE, Phys. Chem. Earth, 25, 401–404, 2000.

Rottman, G. J., Thomas, N., and McClintock, W.: SORCE solar UV irradiance results, Adv. Space Res., 37, doi:10.1016/j.asr.2005.02.072, 2006.

Rozanov, A., Bovensmann, H., Bracher, A., Hrechanyy, S., Rozanov, V., Sinnhuber, M., Stroh, F., and Burrows, J. P.: NO_2 and BrO vertical profile retrieval from SCIAMACHY limb measurements: Sensitivity studies, Adv. Space Res., 36, 846–854, 2005a.

Rozanov, A., Rozanov, V. V., Buchwitz, M., Kokhanovsky, A., and Burrows, J. P.: SCIATRAN 2.0 - A new radiative transfer model for geophysical applications in the 175-2400 nm spectral region, Adv. Space Res., 36, doi:10.1016/j.asr.2005.03.012, 2005b.

Rozanov, E. and, T. E., Schmutz, W., and Peter, T.: Simulation of the stratospheric ozone and temperature response to the solar irradiance variability during sun rotation cycle, J. Atmos. Sol.-Terr. Phys., 68, doi:10.1016/j.jastp.2006.09.004, 2006.

Russel III, J. M., Mlynczak, M. G., Gordley, L. L., Tansock Jr., J. J., and Esplin, R. W.: Overview of the SABER experiment and preliminary calibration results, Proc. SPIE, 3756, doi:10.1117/12.366382, 1999.

Ruzmaikin, A., Santee, M. L., Schwartz, M. J., Froidevaux, L., and Pickett, H. M.: The 27-day variations in stratospheric ozone and temperature: New MLS data, Geophys. Res. Lett., 34, doi:10.1029/2006GL02819, 2007.

Sander, S. P., Friedl, R. R., Golden, D. M., Kurylo, M. J., Moortgat, G. K., Keller-Rudek, H., Wine, P. H., Ravishankara, A. R., Kolb, C. E., Molina, M. J., Finlayson-Pitts, B. J., Huie, R. E., and Orkin, V. L.: Chemical Kinetics and Photochemical Data for Use in Atmospheric Studies: Evaluation Number 15, JPL Publication 06-2, 2005.

Schmidt, H., Brasseur, G. P., Charron, M., Manzini, E., Giorgetta, M. A., Diehl, T., Fomichev, V. I., Kinnison, D., Marsh, D., and Walters, S.: The HAMMONIA Chemistry climate model: Sensitivity of the mesopause region to the 11-year solar cycle and CO_2 doubling, J. Climate, 19, 3903–3931, 2006.

Schneider, N., Selsis, F., Urban, J., Lezeaux, O., de La Noë, J., and Ricaud, P.: Seasonal and Diurnal Variations: Observations and Modeling, J. Atmos. Chem., 50, 25–47, 2005.

Schuster, G. L., Dubovik, O., and Holben, B. N.: Angstrom exponent and bimodal aerosol size distributions, J. Geophys. Res., 111, doi:10.1029/2005JD006328, 2006.

Seinfeld, J. H. and Pandis, S. N.: Atmospheric chemistry and physics, John Wiley, 1998.

Sekiyama, T. T., Shibata, K., Deushi, M., Kodera, K., and Lean, J. L.: Stratospheric ozone variation induced by the 11-year solar cycle: Recent 22-year simulation using 3-D chemical transport model with reanalysis data, Geophys. Res. Lett., 33, doi:10.1029/2006GL026711, 2006.

She, C. and von Zahn, U.: Concept of a two-level mesopause: Support through new lidar observations, J. Geophys. Res., 103, 5855–5863, 1998.

Sinnhuber, M., Burrows, J. P., Chipperfield, M. P., Jackman, C. H., Kallenrode, M.-B., Künzi, K. F., and Quack, M.: A model study of the impact of magnetic field structure on atmospheric composition during solar proton events, Geophys. Res. Lett., 33, doi:10.1029/2003GL017265, 2003.

Skupin, J., Weber, M., Noël, S., Bovensmann, H., and Burrows, J. P.: GOME and SCIAMACHY solar measurements: Solar spectral irradiance and Mg II solar activity proxy indicator, Mem. S. A. It., 76, 1038–1041, 2005.

Smith, A. K., Marsh, D. R., Russel III, J. M., Mlynczak, M. G., Martin-Torres, F. J., and Kyrölä, E.: Satellite observations of high nightime ozone at the equatorial mesopause, J. Geophys. Res., 113, doi:10.1029/2008JD010066, 2008.

Sonkaew, T., Rozanov, V. V., von Savigny, C., Rozanov, A., Bovensmann, H., and Burrows, J. P.: Cloud sensitivity studies for stratospheric and lower mesospheric ozone profile retrievals from measurements of limb scattered solar radiation, Atmos. Meas. Tech. Discuss., 2, 379–438, 2009.

Soukharev, B. E. and Hood, L. L.: Solar cycle variation of stratospheric ozone: multiple regression analysis of long-term satellite data sets and comparisons with models, J. Geophys. Res., 111, doi:10.1029/2006JD007107, 2006.

Stepanov, S. I.: Have the electric currents produced by plasma and magnetic field gradients been discovered in the solar photosphere?, Astronomy Letters, 34, doi:10.1134/S106377370805006X, 2008.

Stolarski, R. and Cicerone, R.: Stratospheric clorine: a possible sink for ozone, Can. J. Chem., 52, 1610, 1974.

Summers, M. E., Strobel, D. F., Bevilaqua, R. M., Zhu, X., DeLand, M. T., Allen, M., and Keating, G. M.: A model study of the response of mesospheric ozone to short-term solar ultraviolet flux variations, J. Geophys. Res., 95, 22 523–22 538, 1990.

Taylor, J. R.: Introduction to Error Analysis: The Study of Uncertainties in Physical Measurements, University Science Books, 1996.

Torrence, C. and Compo, G. P.: A Practical Guide to Wavelet Analysis, Bull. Amer. Meteor. Soc., 79, 61–78, 1998.

Vaughan, G.: Mesospheric ozone - theory and observation, Quart. J. R. Met. Soc., 110, 239–260, 1984.

Viereck, R. A., Floyd, L. E., Crane, P. C., Woods, T. N., Knapp, B. G., Rottman, G., Weber, M., Puga, L. C., and DeLand, M. T.: A composite Mg II index spanning from 1978 to 2003, Space Weather, 2, doi:10.1029/2004SW000084, 2004.

von Savigny, C., Kaiser, J. W., Bovensmann, H., Burrows, J. P., McDermid, I. S., and Leblanc, T.: Spatial and temporal Characterization of SCIAMACHY Limb Pointing Errors during the first three Years of the Mission, Atmos. Chem. Phys., 5, 2593–2602, 2005a.

von Savigny, C., Rozanov, A., Bovensmann, H., Eichmann, K.-U., Noël, S., Rozanov, V. V., Weber, M., Burrows, J. P., and Kaiser, J. W.: The Ozone Hole Breakup in September 2002 as Seen by SCIAMACHY on ENVISAT, J. Atmos. Sci., 62, 721–734, 2005b.

von Zahn, U., Höffner, J., Eska, V., , and Alpers, M.: The mesopause altitude: Only two distinctive levels worldwide?, Geophys. Res. Lett., 23, 3231–3234, 1996.

Weber, M.: Solar Activity during solar cycle 23 monitored by GOME, European Symposium on Atmospheric Measurements from Space, Proc. ESAMS'99, ESA-WPP-161, pp. 611–616, 1999.

Williams, V., Austin, J., and Haigh, J. D.: Model Simulations of the Impact of the 27-day Solar Rotation Period on Stratospheric Ozone and Temperature, Adv. Space Res., 27, 1933–1942, 2001.

WMO: Scientific Assessment of Ozone Depletion: 2003, Global Ozone Research and Monitoring Project - Report No. 47, World Meteorological Organization, Geneva, 2003.

WMO: Scientific Assessment of Ozone Depletion: 2006, Global Ozone Research and Monitoring Project - Report No. 50, World Meteorological Organization, Geneva, 2007.

WMO: Climate Variability and Extremes, `http://www.wmo.int/pages/themes/climate/climate_variability_extremes.php`, 2009.

Wofsy, W. J., McElroy, M., and Yung, Y.: The chemistry of atmospheric bromine, Geophys. Res. Lett., 2, 215–218, 1975.

Woods, T. N., Rottman, G., Harder, J., Lawrence, G., McClintock, B., Kopp, G., and Pankratz, C.: Overview of the EOS SORCE Mission, SPIE Proceedings, 4135, 192–203, 2000.

Woods, T. N., Rottman, G., and Vest, R.: XUV Photometer System (XPS): Overview and Calibrations, Solar Physics, 230, 345–374, 2005.

Zhang, X., Forbes, J. M., Hagan, M. E., Russel III, J. M., Palo, S. E., Mertens, C. J., and Mlynczak, M. G.: Monthly tidal temperatures 20-120 km from SABER/TIMED, J. Geophys. Res., 111, doi:10.1029/2005JA011504, 2006.

Zhou, S., Rottman, G. J., and Miller, A. J.: Stratospheric ozone response to short- and intermediate-term variations in solar UV flux, J. Geophys. Res., 102, 9003–9011, 1997.

Zhou, S., Miller, A. J., and Hood, L. L.: A partial correlation analysis of the stratospheric ozone response to 27-day solar UV variations with temperature effects removed, J. Geophys. Res., 105, 4491–4500, 2000.

Zhu, X., Yee, J.-H., and Talaat, E. R.: Effect of short-term solar ultraviolet flux variability in a coupled model of photochemistry and dynamics, J. Atmos. Sci., 60, 491–509, 2003.

Acknowledgements

My sincere gratitude goes to ...

... Prof. John Burrows for the opportunity to work at IUP Bremen in his group on a fascinating topic within the field of satellite remote sensing. I really learned what it means "“Wir sehen jeden Dreck!"” (We see all the dirt!).

... Prof. Justus Notholt für die kurzfristige Zusage als zweiter Gutachter zur Verfügung zu stehen.

... Mark Weber for his supervision and his valuable advice in scientific and non-scientific matters. With his support, he guided me through three years of hard work with its ups and downs.

... Christian von Savigny for adding valuable scientific content to my work. Also the SCIAMACHY group for providing the new ozone data set.

... PIP (Postgraduate International Program) for financial benefits for hardware and conference travel expenses.

... Deutsche Forschungsgemeinschaft (DFG) for funding this study (SOLOZON project) as part of the German priority program CAWSES.

... ECMWF for temperature data made available via the ECMWF special project SPDECDIO.

... Martin Mlynczak and the SABER science team for providing satellite data.

... Hauke Schmidt and the Deutsches Klimarechenzentrum (DKRZ) for performing

the numerical simulations with HAMMONIA.

... Miriam Sinnhuber and Holger Winkler for their help to understand and work with TOMCAT.

... Petra Horn, Birgit Teuchert, and Heidemarie Krug for their patience when I kept them going with bureaucratic matters.

... Joana Leitao, Max Reuter, Oliver Schneising, Sebastian Mieruch, and Christian Theiß for reviewing this thesis. On short notice, you supported me, which first and foremost calmed me down and additionally helped me to see my thesis from a critical perspective.

... All members of IUP Bremen I worked with for the great experiences I've made with you, be it at the institute or after work. You never declined to help when asked. Brilliant!

... Philipp Grünling and Christian Theiß for being really good friends when I needed them the most. One cannot perform properly at work, when private matters block his mind.

... Meiner Mutter, Tante Helga und meinen Geschwistern und ihren Familien für das schöne Gefühl noch immer in einer großen Familie geborgen zu sein. Tante Helga für ihre freundliche Ruhe und dafür für uns alle da zu sein, wenn uns die Sorgen mal wieder plagen. Zu guter letzt gilt mein herzlichster Dank meinen Eltern für ihre bedingungslose Liebe zu ihren Kindern. Ein besonderes Dankeschön an meine Mutter für die Unterstützung und Aufopferung über all die Jahre. Ich bin froh, dass ich euch Alle habe.